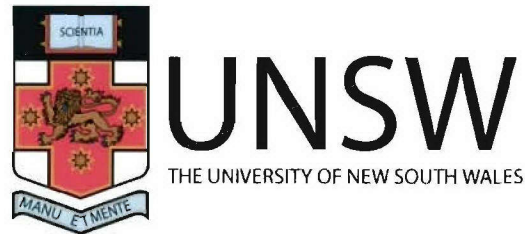


REPORT DOCUMENTATION PAGE					<i>Form Approved</i> OMB No. 0704-0188	
The public reporting burden for this collection of information is estimated to average 1 hour per response, including the time for reviewing instructions, searching existing data sources, gathering and maintaining the data needed, and completing and reviewing the collection of information. Send comments regarding this burden estimate or any other aspect of this collection of information, including suggestions for reducing the burden, to Department of Defense, Washington Headquarters Services, Directorate for Information Operations and Reports (0704-0188), 1215 Jefferson Davis Highway, Suite 1204, Arlington, VA 22202-4302. Respondents should be aware that notwithstanding any other provision of law, no person shall be subject to any penalty for failing to comply with a collection of information if it does not display a currently valid OMB control number.						
1. REPORT DATE (DD-MM-YYYY) 31-03-2005		2. REPORT TYPE Final			3. DATES COVERED (From - To) 1 Feb 02 – 31 Mar 03	
4. TITLE AND SUBTITLE Hydrocarbon-Fueled Scramjet Research at Hypersonic Mach Numbers				5a. CONTRACT NUMBER F6256202P0243		
				5b. GRANT NUMBER		
				5c. PROGRAM ELEMENT NUMBER		
6. AUTHOR(S) Dr. Frank Houwing				5d. PROJECT NUMBER		
				5e. TASK NUMBER		
				5f. WORK UNIT NUMBER		
7. PERFORMING ORGANIZATION NAME(S) AND ADDRESS(ES) Australian National University Dept of Physics ACT 0200 Australia					8. PERFORMING ORGANIZATION REPORT NUMBER N/A	
9. SPONSORING/MONITORING AGENCY NAME(S) AND ADDRESS(ES) AOARD UNIT 45002 APO AP 96337-5002					10. SPONSOR/MONITOR'S ACRONYM(S) AOARD	
					11. SPONSOR/MONITOR'S REPORT NUMBER(S) AOARD-024001	
12. DISTRIBUTION/AVAILABILITY STATEMENT Approved for Public Release. Distribution unlimited.						
13. SUPPLEMENTARY NOTES						
14. ABSTRACT Planar laser-induced fluorescence (PLIF) of OH and wall-pressure measurements have been used to investigate the combustion in a cavity flame-holder scramjet combustor.						
15. SUBJECT TERMS Aeroengines, Hypersonics, Hypersonic Test Facilities						
16. SECURITY CLASSIFICATION OF:			17. LIMITATION OF ABSTRACT	18. NUMBER OF PAGES	19a. NAME OF RESPONSIBLE PERSON	
a. REPORT	b. ABSTRACT	c. THIS PAGE			Anthony M. Mitchell, Maj, USAF	
U	U	U	UU	124	19b. TELEPHONE NUMBER (Include area code) +81-3-5410-4409	



HYDROCARBON-FUELED SCRAMJET RESEARCH AT HYPERSONIC MACH NUMBERS

Sean O'Byrne, Ingo Stotz, Andrew Neely, Russell Boyce,

Frank Houwing[†], Neil Mudford, Christina Riley

University of New South Wales, Australian Defence Force Academy,
Canberra, ACT, 2600, Australia

[†] Australian National University, Acton, ACT, 0200, Australia

DISTRIBUTION STATEMENT A
Approved for Public Release
Distribution Unlimited

Sponsored by:

Air Force Office of Space Research, Grant Number AOARD-02-4001

For Wright Patterson Air Force Base

Report Submitted: March 31, 2005

AQ F05-12-3725

Abstract

Planar laser-induced fluorescence (PLIF) of OH and wall-pressure measurements have been used to investigate the combustion in a cavity flame-holder scramjet combustor. The experiments were conducted in the T3 free-piston-driven shock tunnel using a Nd:YAG laser to pump a dye laser system exciting the $Q_1(8.5)$ transition of the hydroxyl radical. The OH radical was chosen as it is one of the most abundant species in flames and therefore is a good indicator for ignition and combustion in general. Two different fuels, hydrogen and ethylene, were tested at three different equivalence ratios each ($\Phi = 0.15$, $\Phi = 0.24$ and $\Phi = 0.47$ for hydrogen, $\Phi = 0.13$, $\Phi = 0.37$ and $\Phi = 0.64$ for ethylene). The shock tunnel produced a 6.15 MJ/kg flow condition corresponding to a simulated flight Mach number of approximately 11.5 at an altitude of approximately 29 km. OH PLIF images obtained at three different planes in the scramjet combustor are presented. Pressure measurements along the scramjet duct centerline were recorded for each equivalence ratio.

Supersonic combustion was achieved for all conditions investigated. The PLIF images clearly show the presence of OH above and downstream of the cavity indicating the ignition zone. The penetration height of the OH plume was found to be linearly dependent on the equivalence ratio. The pressure measurements particularly showed the locations of oblique shock waves in the scramjet duct and indicated a significant pressure rise due to combustion. Similarities and differences for the different equivalence ratios and fuels were observed and are discussed in detail.

The images clearly show the ignition length scales for the two fuels, and these agree with empirical calculations. A significant change in the spatial distribution of OH concentration was noted at the highest ethylene equivalence ratio. The OH PLIF images show a localized, intense fluorescence signal near the injection point, with much lower signal further downstream. This was not noted for hydrogen injection. The exact cause of this change is not known, although possible explanations for the behavior are discussed.

Computations of the flow field at a lower static to the experiments are presented. For this reason, direct comparison with experiment is not made, but the resulting maps of computed flow quantities provided valuable insight into the mixing and combustion processes occurring in the combustor.

Contents

List of Figures	vi
List of Tables	vii
Nomenclature	viii
1 Introduction	1
1.1 Cavity-based Fuel Injection	2
1.1.1 Cavity Flow Regimes	2
1.1.2 Previous Cavity Experiments	3
1.1.3 Investigation of Suitable Fuels	4
1.1.4 Effect of Equivalence Ratio	6
1.1.5 Flight Mach Number	6
1.1.6 PLIF Measurements in Scramjet Combustors	7
1.1.7 Computational Fluid Dynamic Studies	8
1.2 Overview	8
2 Experimental Apparatus and Procedures	10
2.1 The T3 Free-Piston-Driven Shock Tunnel	10
2.1.1 Shock Tunnel Operation	11
2.1.2 Tunnel Fill Conditions	12
2.1.3 Nozzle Reservoir Conditions	13
2.1.4 Freestream Conditions	15
2.2 The Cavity Flame-Holder Scramjet	17
2.2.1 The Experimental Scramjet Combustor Model	18
2.2.1.1 Instrumentation	19
2.3 The Fuel Injection System	21
2.3.1 Functional Principle	21
2.3.2 Calibration of the Fuel Injection System	22
2.3.3 Equivalence Ratio Calculation	26
2.4 PLIF Apparatus and Procedure	28
2.4.1 Tunnel Run Procedure	31
2.5 Data Reduction	33
2.5.1 PLIF	33
2.5.2 Pressure Measurements	36
3 Initial Scramjet Experiments	38

3.1	Data Analysis	39
3.1.1	Pressure Comparisons	39
3.1.2	Equivalence Ratio Effects	46
3.2	Discussion of Static Pressure Results	47
3.2.1	Combustor Flow Field	47
3.2.2	Combustion Pressure Rise and Ignition Length	49
3.2.3	Equivalence Ratio Effects	50
3.2.4	Summary	50
4	Preliminary PLIF Experiments and CFD Methodology	52
4.1	Theoretical Aspects of Laser-Induced Fluorescence	52
4.1.1	Laser-Induced Fluorescence (LIF)	52
4.1.2	Planar Laser-Induced Fluorescence (PLIF)	53
4.1.3	The Two-Level Model	54
4.2	Preliminary PLIF Calibration Experiments	57
4.2.1	Saturation Irradiance Measurements	57
4.2.2	Response of the ICCD Camera	58
4.2.3	Spatial Laser Profile Corrections	61
4.2.4	Transition Choice	63
4.2.5	Accuracy and Repeatability of Tuning on Transitions	64
4.2.6	Focusing on the Image Plane	65
4.3	Computational Fluid Dynamics (CFD)	66
4.3.1	The CFD++ [®] code	66
4.3.2	Governing Equations	67
4.3.3	Fluid Properties (Real Gas Thermodynamic Model)	68
4.3.4	Turbulence Modeling	69
4.3.5	Chemistry Model	69
4.3.6	The Scramjet Simulation Model	70
4.3.7	Initial and Boundary Conditions	72
5	OH PLIF and CFD Results	74
5.1	Experimental Results	75
5.1.1	General Observations	75
5.1.2	Repeatability	81
5.1.3	Influence of Equivalence Ratio and Laser Sheet Location	84
5.1.3.1	Hydrogen Fuel	85
5.1.3.2	Ethylene Fuel and Comparison of Fuels	88
5.2	CFD Results	96
5.2.1	Basic Flow Structures	97
5.2.2	Fuel/Air Mixing	98
5.2.3	Combustion	101
5.2.4	Qualitative Comparison of Computation and Experiment	102
6	Conclusions and Recommendations for Future Work	104
6.1	Experiments	105
6.2	CFD	106

6.3 Proposal for Further Research	107
Acknowledgements	110
A PLIF and Luminosity Images	111
References	120

List of Figures

2.1	Schematic of the T3 free-piston-driven shock tunnel	11
2.2	Typical nozzle-reservoir trace	14
2.3	Histograms showing the variability of (a) the shock velocity and (b) the nozzle reservoir pressure	15
2.4	Scramjet inlet cross-section (left) and cavity dimensions (right)	18
2.5	Positions of the piezoelectric pressure transducers	19
2.6	Details of the pressure transducer mounts	20
2.7	Fuel injection system	21
2.8	Typical fuel pressure trace - entire injection period	22
2.9	Typical fuel pressure trace - magnification	23
2.10	Fuel mass fluxes versus Ludwig tube fill pressure	26
2.11	Equivalence ratio versus Ludwig tube fill pressure	28
2.12	Experimental arrangement for the OH PLIF experiments	29
2.13	Trigger logic – timing electronics	32
2.14	Raw false color images	34
2.15	Flow chart of PLIF data reduction process	35
2.16	Region within the flow, selected to compare averaged OH signals	36
3.1	Normalized static pressure histories	40
3.2	$H_2, \Phi = 0.24$ normalized floor pressure.	40
3.3	$H_2, \Phi = 0.47$ normalized floor pressure.	41
3.4	$H_2, \Phi = 0.42$ normalized floor pressure.	41
3.5	$C_2H_4, \Phi = 0.57$ normalized floor pressure.	42
3.6	Luminosity image of the scramjet inlet	43
3.7	Normalized floor pressure, hydrogen into nitrogen at various equivalence ratios.	44
3.8	Normalized floor pressure, hydrogen into air at various equivalence ratios.	44
3.9	Normalized floor pressure, ethylene into nitrogen at various equivalence ratios.	45
3.10	Normalized floor pressure, ethylene into air at various equivalence ratios.	45
3.11	Dependence of cavity floor pressure on equivalence ratio	46
3.12	Integrated pressure rise for different equivalence ratios	47
3.13	Combustion chamber flow field structures	48
4.1	Schematic of LIF excitation between two rovibronic states of OH and subsequent relaxation	55
4.2	(a) Experimental apparatus for the laser sheet thickness measurement. (b) Measured profile	59
4.3	Saturation irradiance measurement	60

4.4	(a) Example OH PLIF image in a flame. (b) Camera response for different gain settings	61
4.5	(a) Laser sheet image, (b) Laser sheet profile	62
4.6	Temperature dependence of the Q_1 (8.5) transition	63
4.7	Numerical prediction of OH excitation spectrum	64
4.8	Accuracy of tuning the laser on the peak transition	65
4.9	Grid image	66
4.10	Computational mesh of the scramjet model	71
5.1	Laser sheet locations	75
5.2	Typical OH PLIF combustion image	76
5.3	Pressure distribution during nominal test time for hydrogen injection into air and nitrogen	77
5.4	Typical image of the spatial OH distribution	78
5.5	Spatial PLIF signal distribution	79
5.6	Comparison between PLIF image and luminosity image	80
5.7	Repeatability of PLIF experiments a)	82
5.8	Repeatability of PLIF experiments b)	83
5.9	Repeatability of pressure measurements	83
5.10	Pressure comparison campaigns for different ethylene equivalence ratios	84
5.11	Effects of equivalence ratio variation (hydrogen)	86
5.12	Pressure distributions for hydrogen injection into air and nitrogen plots for different hydrogen equivalence ratios	87
5.13	Penetration height of OH-plume (hydrogen above injection port)	88
5.14	PLIF images captured on different laser sheet locations (hydrogen, $\Phi = 0.47$)	89
5.15	Penetration height depending on the visualization plane	90
5.16	PLIF and luminosity images for three different ethylene equivalence ratios	91
5.17	Pressure distributions for ethylene	92
5.18	Pressure distributions for ethylene injection into air and nitrogen ($\Phi = 0.37$)	93
5.19	Comparison of penetration heights for different fuels and equivalence ratios	93
5.20	Pressure-ratio comparison of lowest equivalence ratios for hydrogen and ethylene	94
5.21	PLIF images for three different ethylene equivalence ratios and two laser sheet locations	95
5.22	Pressure distribution on the center plane, non-injection	97
5.23	Mach number distribution on the center plane, non-injection	97
5.24	Mach number distribution and streamline traces in and above the cavity, non-injection	98
5.25	Pressure distribution in the scramjet duct, frozen reactions	99
5.26	Mach number distribution and streamline traces in and above the cavity, frozen reactions	99
5.27	Mass fraction of hydrogen, frozen reactions	100
5.28	Mole fractions of H_2O , finite-rate reactions	102
5.29	Mole fractions of OH, finite-rate reactions	103
5.30	Overlay of luminosity image and computational pressure distribution	103
A.1	Hydrogen, high equivalence ratio ($\Phi = 0.47$)	112
A.2	Hydrogen, high equivalence ratio ($\Phi = 0.47$)	113

A.3 Hydrogen, medium equivalence ratio ($\Phi = 0.24$) 114

A.4 Hydrogen, low equivalence ratio ($\Phi = 0.15$) 115

A.5 Ethylene, high equivalence ratio ($\Phi = 0.64$) 116

A.6 Ethylene, medium equivalence ratio ($\Phi = 0.37$) 117

A.7 Ethylene, low equivalence ratio ($\Phi = 0.13$) 118

A.8 Luminosity images 119

List of Tables

2.1	Shock tunnel parameters	13
2.2	Nozzle reservoir conditions	16
2.3	Calculated freestream conditions	17
2.4	Pressure transducer specifications	20
2.5	Fuel injection conditions	25
2.6	Equivalence ratios	28

Nomenclature

Latin symbols

Symbol	Definition
a	speed of sound, ms^{-1}
a^*	speed of sound at nozzle throat, ms^{-1}
$a_m, b_m, c_m,$ d_m, e_m, g_m	curve fit coefficients
A	nozzle area, m^2 cross-section area of laser sheet, m^2 cross-section of scramjet duct, m^2 Einstein A coefficient for spontaneous absorption/emission, s^{-1}
A^*	nozzle throat area, m^2
B	Einstein B coefficient for stimulated absorption/emission, cmJ^{-1}
c_p	specific heat at constant pressure, $Jkg^{-1}K^{-1}$
c_v	specific heat at constant volume, $Jkg^{-1}K^{-1}$
C	Chapman-Rubesin parameter, $\rho\mu/(\rho_e\mu_e)$ compression tube fill pressure, kPa
d	distance
D	cavity depth, m diaphragm burst pressure, Pa
e	specific internal energy, J
E	laser energy, J activation energy, $Nm/kmol$
f	fuel/air ratio
f_B	Boltzmann fraction
g	spectral overlap integral, cm
G	Gibb's free energy, J/mol
h	specific enthalpy, Jkg^{-1} Planck constant, Js
ΔH_f	enthalpy of formation
I	laser irradiance, Wm^{-2}
J	rotational level

k	Boltzmann constant, $K^{-1}cm^{-1}$ frequency factor, $s^{-1}(m^3/mol)^{step-reactants-1}$
K_e	equilibrium constant
l	(characteristic) length, m
L	cavity length, m
m	mass, kg
\dot{m}	mass flux, $kg s^{-1}$
M	Mach number, v/a
n	temperature exponent, K
N_T	number density, m^{-3}
p	pressure, Pa
p^*	pressure at nozzle throat, Pa
p_m	plenum pressure, Pa
q	heat flux (vector), Wm^{-2}
Q	collisional quenching rate, s^{-1}
R	specific gas constant, $Jkg^{-1}K^{-1}$ high-pressure reservoir pressure, Pa
Re_x	(local) Reynolds number based on length x , $(\rho ux)/\mu$
S_f	time-integrated fluorescence signal imaged by the camera, <i>arbitrary units</i>
t	time, s
T	temperature, K
T^*	temperature at nozzle throat, Pa
v	vibrational level velocity, ms^{-1} diffusion velocity, ms^{-1}
V	volume, m^3
\dot{w}	production rate, s^{-1}
W	stimulated emission/absorption rate coefficient, s^{-1}
x, y, z	spatial coordinates, m
Y	mass fraction

Greek symbols

Symbol	Definition
β	oblique shock deflection angle, <i>deg</i>
δ	boundary layer thickness, m Kronecker symbol
γ	ratio of specific heats, c_p/c_v
η	camera efficiency
η_c	collection efficiency of PLIF system
θ	flow turning/deflection angle, <i>deg</i>
Θ	characteristic vibrational temperature for a species, K

λ	shock tube compression ratio
μ	viscosity, $kgm^{-1}s^{-1}$
ρ	density, kgm^{-3}
ρ^*	density at nozzle throat, kgm^{-3}
τ_c	time for chemical reactions to approach equilibrium, s
τ_f	flow residence time, s
τ_{ij}	shear stress tensor, Nm^{-1}
Φ	equivalence ratio
	fluorescence yield, $A_{21}/(A_{21} + Q_{21})$
	angle the reflected shock wave forms with the wall, deg
Ω	solid angle, Sr

Subscripts

Symbol	Definition
∞	freestream/farfield
'	excited state vibrational and rotational levels
"	ground state vibrational and rotational levels
0	at stagnation conditions
1, 2, ...	enumeration for flow properties at different locations
b	backward
f	flow
	forward
	final
i	initial
i, j, k	spatial directions
m	atomicities of carbon in hydrocarbon fuels
n	atomicities of hydrogen in hydrocarbon fuels
max	maximum
sat	saturation
st	stoichiometric
x, y, z	horizontal and vertical directions

Acronyms, abbreviations and chemical symbols

Symbol	Definition
3D	three-dimensional

ADFA	Australian Defence Force Academy
ALDiR	Aerophysics and Laser-Based Diagnostics Laboratory
ANU	Australian National University
APAC	Australian Partnership for Advanced Computing
Ar	argon
CH	methylidyne radical
C ₂ H ₄	ethylene
CO ₂	carbon dioxide
CCD	charge-coupled device
CFD	computational fluid dynamics
CRO	cathode-ray oscilloscope
ESTC	equilibrium shock-tube code
H ₂ O	water
ICCD	intensified charge-coupled device
LIF	laser-induced fluorescence
N	atomic nitrogen
N ₂	molecular nitrogen
NASA	National Aeronautics and Space Administration
NH	imidyl radical
NO	nitric oxide
O	atomic oxygen
O ₂	molecular oxygen
OH	hydroxyl radical
ppm	parts per million
PD	photodiode
PLIF	planar laser-induced fluorescence
PMT	photomultiplier tube
RAM	random access memory
RANS	Reynolds-averaged Navier-Stokes
RET	rotational energy transfer
TDLAS	tunable diode laser absorption spectroscopy
UNSW	University of New South Wales
UV	ultraviolet
UQ	University of Queensland
VET	vibrational energy transfer

Chapter 1

Introduction

This report examines the flow within the combustor of a supersonic combustion ramjet engine using a cavity-based fuel injection scheme. Work at lower Mach numbers (Tishkoff et al. 1997) has shown that the cavity injector has excellent properties for use as a fuel injection system: it assists in flame-holding and mixing of the flow and is less of an obstruction to the oncoming flow than other configurations such as strut injectors. However until now little work has been done to investigate the performance of this injections scheme at higher flight Mach numbers. This report presents an initial investigation into the viability of combustion at flight Mach numbers above Mach 10 using cavity fuel injection.

The experimental campaign was performed with the following aims in mind:

- To experimentally determine whether supersonic combustion will occur at a flight Mach number above Mach 10 using a cavity-based injector geometry. The T3 free-piston driven reflected shock tunnel facility at the Australian National University was used to produce the flow conditions required to simulate the flow in the combustor at such flight Mach numbers. The scramjet configuration was tested in a semi-direct-connect configuration.
- To gain a deeper insight into where ignition occurs in the flow field. To achieve this, planar laser-induced fluorescence PLIF of the hydroxyl(OH) radical is performed on the combustor. This gives a qualitative indication of where OH is produced within the combustor. Issues such as whether significant radical populations are produced within the cavity can also be addressed. The initial portion of this work concentrated on pressure measurements to indicate where combustion took place. These pressure measurements can be directly compared to the OH visualizations to determine how the locations of the static pressure rise and the flame front correlate with each other.
- To compare the performance of hydrogen and ethylene as fuels using this configuration. Ethylene and other hydrocarbon fuels have a significantly longer ignition delay time than

hydrogen does, which can adversely affect combustor performance. As hydrocarbon-based fuels have a number of practical advantages when compared with hydrogen, it is important to evaluate their performance relative to using hydrogen. To this end, experiments were performed in which each fuel was injected into the cavity at a range of equivalence ratios.

- To produce high-quality experimental visualizations and pressure measurements at known free stream conditions that can be directly compared to numerical simulations.

1.1 Cavity-based Fuel Injection

Critical to the performance of any air-breathing engine are the successful mixing of the fuel with the oncoming flow, and the ability to initiate and maintain combustion. This is particularly true for the supersonic combustion process in a scramjet. It is desirable to inject the fuel in a way that minimizes the disturbance to the airflow, yet maximizes the efficiency with which fuel-air mixing occurs. Due to the high velocity of the airflow through the combustion chamber duct, the time available for fuel injection, mixing and combustion is very short. Thus, it is crucial to minimize the delay time for ignition of the flame, to avoid excessive combustion lengths and hence excessive weight and drag penalties ((Heiser and Pratt 1994)). Strut injectors, while being attractive for their contribution to mixing and flame-holding in a scramjet combustor, suffer from increased drag and thermal loading ((Kanda et al. 2001, Tomioka et al. 2001)). Transverse injection of fuel from the sidewall causes a detached normal shock to be produced upstream of the fuel jet. As a result, considerable losses in total pressure and hence cycle efficiency can occur ((Seiner et al. 2001)). Angling the injectors downstream can reduce these losses, but also reduces the mixing effectiveness and flame holding ability. Previous research has indicated that the addition of one or more cavities in the walls of the combustor can improve the mixing and flame holding capabilities, by providing an area where subsonic recirculation of fuel and air can occur, thus aiding in the mixing process and allowing sufficient time for the combustion process to begin, and intermediate radicals to be produced. All previous cavity combustion work reported has been at low hypersonic flight Mach numbers for which ramjet or dual-mode ramjet/scramjet operation is observed. No experimental combustion data has previously been obtained for flight Mach numbers of the order of 10 or above. This has provided the motivation for the present study.

1.1.1 Cavity Flow Regimes

The addition of a cavity to a scramjet combustor is a trade off between the benefits to flame-holding and the promotion of efficient combustion and the resultant drag penalty. Ben-Yakar

and Hanson (2001) provide a comprehensive review of the various issues associated with the use of cavities. The mixing and flame-holding properties of a scramjet can be significantly improved through the addition of a cavity. As the convective Mach number increases, compressibility effects suppress the growth of the shear layer causing the mixing of the oncoming air and the fuel to decrease.¹ However it has been demonstrated that the mixing of the shear layers can be improved by the presence of cavity flow oscillations. These instabilities enhance the mixing capabilities. The opposite case is a stable cavity, which aids in flame holding. Cavities produce a recirculation of radicals, with sufficient residence time for ignition to occur without the need for long combustion chamber lengths. If the recirculation in the cavity is stable, a continuous ignition source is present and thus flame holding is improved significantly. The stability of a cavity is directly related to its design ((Ben-Yakar and Hanson 2001)). For all cavity geometries, the flow separates from the upstream lip, forming a shear layer, and reattaches downstream. A higher pressure results from the shear layer impingement at the rear wall, and subsequently increases the cavity drag, since the pressure at the front face is lower than that at the rear. By inclining the rear wall, the drag may be reduced. Particular ramp angles have been found to minimize the drag penalty of the cavity ((Gruber et al. 2001, Mathur et al. 2001, Zhang et al. 1998)). The interaction of the shear layer with the rear wall also causes fluctuations to occur, i.e. the cavity resonates. These instabilities can aid the mixing process and are used in so-called unstable cavities but they can reduce the ability of the cavity to act as a flameholder. In order to minimize fluctuations, the shear layer needs to be controlled. Experimental results have shown that an inclined rear wall assists in the stabilization of the shear layer by eliminating the generation of the traveling waves inside the cavity, and hence alleviates the fluctuation effect as well((Ben-Yakar and Hanson 2001)). This passive stabilization technique, while not being optimal for all flow conditions is simpler than proposed active systems that utilize variable fuel injection upstream of the cavity lip. Cavity geometry is characterized by its length to depth (L/D) ratio. A cavity is termed open if the ratio is less than approximately 10. For these ratios, the free shear layer will reattach to the rear face of the cavity. For L/D greater than 10, the cavity is considered closed, because the shear layer will reattach on the cavity floor. The boundary layer thickness at the cavity leading edge, the flow Mach number and the cavity width determine the critical L/D ratio. For fluid injection, the L/D ratios should be larger, to achieve steady flow. Studies have indicated that for longer lengths and inclined walls, cavity residence time is decreased. However for greater L/D ratios, the drag coefficient increases significantly ((Ben-Yakar and Hanson 2001)).

1.1.2 Previous Cavity Experiments

Various combinations of L/D ratios, ramp angles and overall engine design have been tested in recent years; the aim being to optimize the cavity configuration for minimum losses, and effective flame holding. Again, Ben-Yakar and Hanson (2001) provide a comprehensive summary of this work. The initial cavity experiments were conducted in a joint Russian/French project

designed by the Central Institution of Aviation Motors (CIAM) in Moscow. The project established that the use of a cavity for hydrocarbon combustion was beneficial. CIAM conducted further cavity experiments that showed for Mach 6.5 flow speeds, auto-ignition and flame holding can be achieved without the use of spark plugs. The engine flow path incorporated two cavities, a step flameholder and three separate injection points, one in each of the front cavity walls at 30° to the engine axis, and another just upstream of the step at 45°. Due to the small injector diameters, it was highly unlikely ignition would have occurred without the cavity. A flight test of the design did achieve positive thrust ((Ben-Yakar and Hanson 2001)). It is thought however that this test did not produce true scramjet operation, since the flow in the combustor had substantial subsonic regions. Effectively, it was a ramjet test at higher than normal flight Mach number. Ben-Yakar and Hanson (2001) conducted flow visualization experiments of duct flows across various cavity geometries using an expansion tube. They simulated Mach 10 total enthalpy conditions at combustor entry but could only produce a flow of low stagnation pressure in which combustion was not possible. Experimental results have indicated that there is an optimal ramp angle in which drag is minimized. The AFRL at Wright-Patterson AFB investigated ramp angles of 16°, 30° and 90° in a Mach 3 flow, and concluded that drag increases with shallower ramp angles ((Gruber et al. 2001, Mathur et al. 2001)). This can be attributed to an expansion wave being created at the leading edge of the cavity, and the shear layer deflecting further into the cavity. These factors cause the pressure to drop, and a larger area of recompression to develop at the rear cavity face, resulting in increased drag. Opposite results appeared when Zhang et al. (1998) produced numerical calculations. They investigated the effect of reducing the ramp angle from 90° to 67.5° and 45°, and obtained results that indicated drag is reduced with decreasing ramp angle. Both these sets of results showed that the pressure on the front wall is reduced with decreasing rear ramp angle. An earlier study by Samimy et al. (1986) minimized the losses due to drag by using a 20° ramp angle. The shear layer was undisturbed at this configuration, and thus the pressure within the cavity remained unchanged, minimizing drag. From these three separate results, it can be concluded that the optimal ramp angle lies between 16° and 45° ((Ben-Yakar and Hanson 2001)). Yu et al. (2001) investigated several cavity configurations, and determined that a two step cavity with an inclined wall was the most efficient configuration; resulting in the highest increase in combustor pressure and exit recovery temperature. This also demonstrated a significant improvement in combustion ((Seiner et al. 2001)). Other research efforts by the same group investigated flow stability and flameholding capabilities at Mach 2. They altered the ramp angle and tested L/D ratios of 0.5, 1, 2, 3 and 5. The small L/D ratios produced successful flame holding. However the L/D ratio of 5 had an inclined rear ramp, and interestingly, failed to hold a flame at all.

1.1.3 Investigation of Suitable Fuels

Traditionally, scramjet research has focused on the use of hydrogen for fuel given its ease of combustion and high energy density. Hydrocarbon fuels though are logistically more attrac-

tive than hydrogen given the problems associated with storing the lower density fuel, and the significant safety measures that must be in place. This may not be such an issue for civilian operators, whose vehicles launch from the one location, and thus all supporting infrastructure can be permanently located on site. However for military applications, such as hypersonic missiles, it is essential that all resources be easily transportable. Using a hydrocarbon fuel will decrease vehicle size due to its higher density, be simpler to manage logistically, and be sufficient for flight numbers up to approximately Mach 10 ((Townend 2001)). Some hydrocarbon fuels such as ethylene also have the operational advantage of liquefaction at room temperature ((Paull and Stalker 2000)). The combustion of fuel is not instantaneous, there is a finite time for combustion, characterized by the type of fuel. This becomes an issue for scramjet engines, due to the flow being supersonic, and thus time for combustion is minimal. For flight Mach numbers greater than 8 where combustion lengths are at their most critical, hydrogen is the preferred fuel, due to its short ignition time.⁵ Below Mach 8, hydrocarbon fuels become more desirable due to their higher densities. Hydrocarbon fuels tend to have longer ignition times and reduced reaction rates compared to hydrogen. Thus the use of cavity flameholders becomes even more desirable for these fuels to minimize combustor length, especially at high Mach number. Fuels must be broken down into intermediate species before combustion is possible. In the case of hydrogen, the H_2 molecules have to be broken down into the H and OH radicals. Hydrogen combustion occurs relatively fast, due to this small molecular structure. However typical hydrocarbons of interest (for example, kerosene) can have rather long chains, and thus take a significant time to react. A suggested solution is to circulate the fuel around the vehicle body through pipes, in order to absorb the heat generated by the vehicle traveling at hypersonic speeds ((Colket and Spaddaccini 2001)). The heat absorbed will cool the vehicle, at the same time as heating the fuel and thus assist in the cracking (thermal decomposition) of the long chains before injection into the combustor. Combustion of the smaller hydrocarbons is then able to proceed at faster rates than for the original kerosene. The fastest of these small hydrocarbons to burn is ethylene (C_2H_4) ((Colket and Spaddaccini 2001)). Consequently, ethylene is often used as a substitute for kerosene-like fuels in scramjet ground tests, in order to obtain fundamental data on hydrocarbon-fueled scramjet performance. It is a primary fuel in itself, and is the product of the combustion of methane, ethane and other longer-chain hydrocarbons. For most of the hydrocarbon-fueled tests conducted thus far, an igniter has been required to initiate and maintain the flame. Hydrogen pilots have been shown to be effective for ethylene or kerosene fuels ((Taha et al. 2002)). Wright-Patterson Air Force Research Laboratories injected gaseous ethylene fuel upstream of the cavity. Tests were conducted for equivalence ratios of 0.25 to 0.75, at a dynamic pressure of 49.7 kPa, and used only a spark plug for ignition. Combustion efficiencies of about 80% holding and large flame-spreading in the cavity region were observed for all test conditions ((Mathur et al. 2001)).

1.1.4 Effect of Equivalence Ratio

In the AFRL tests, using ethylene fuel and simulated flight speeds between Mach 4 and 6, the equivalence ratio was varied between 0.25 and 0.757. Wall static pressure distributions were produced for each equivalence ratio. The greatest pressure ratio (P_{wall}/P_{inlet}) was observed in the cavity region. This occurs because at these low flight Mach numbers, subsonic flow (ramjet operation) often occurs in the combustor, induced by a shock train that straddles the injection point ((Heiser and Pratt 1994)). Cavity flame holding capabilities under such conditions become of extreme importance, as the shock can extinguish the flame. As the fuel flow rate was increased in the above experiments, the shock system began to shift upstream more and more, and the overall pressure ratio distribution increased with increasing equivalence ratio. Ratner et al. (2001) measured the combustion efficiency values in supersonic flames, using hydrogen fuel at a flight Mach number of 2.5. They increased the equivalence ratio from 0.034 to 0.068, and found that by doing this, the combustion efficiency and the flame length were both increased. The increase in combustion efficiency was found to have a virtually linear relationship with increasing fuel mass flow rate. This was attributed to the fact that increasing the fuel flow rate will increase the volume of the flame and thus there is less chance that the oncoming flow will be convected around the flame, and remain unburnt. Also, this will create a longer flame length, providing a longer residence time for fuel oxidation.

1.1.5 Flight Mach Number

The majority of the experiments investigating the use of cavities to aid supersonic combustion have been performed at the lower end of the flight Mach number range (less than 8) for which scramjet operation is envisaged. This is due to the limitations imposed by most ground-based test facilities. To date, the research has aimed at finding the optimum specifications for specific flight conditions, such as cavity geometry, the type of fuel used, and appropriate fuel/air equivalence ratios. The knowledge base for these conditions is increasing, but again, only for low Mach numbers. The experiments reported here extend this knowledge base to flight at Mach 11.5.

Griffiths (2004) used a tunable diode laser absorption spectroscopy (*TDLAS*) system to measure water vapor concentration and temperature in a combusting scramjet flow. The *TDLAS* was applied to a similar cavity flame-holder scramjet model as used in Neely et al. (2003). The water vapor Griffiths detected is evidence of supersonic combustion. The measurements were able to resolve trends over the test time of the facility and showed different water vapor concentrations and temperatures at different heights in the duct.

1.1.6 PLIF Measurements in Scramjet Combustors

Since its first employment by Cattolica and Stephenson (1984), Planar Laser-Induced Fluorescence (PLIF) has become a major flow diagnostic technique. Initially used for measuring number densities and temperatures in flames its application has been extended to measuring velocity, pressure and mole-fractions in a large variety of flow fields.

Allen et al. (1993) showed applications of PLIF measurements of OH and NO in a model scramjet combustor using an excimer-pumped dye laser system. Strategies for measurements of species number densities, mole fractions and static gas temperature were developed and the possibilities for the quantitative interpretation of the PLIF measurements were discussed. The NO PLIF images they obtained demonstrate the potential of NO PLIF for quantitative measurements in high temperature, supersonic flows. They also discussed in detail the limitations to the quantitative interpretation of supersonic reacting flows.

Recently Gruber et al. (2004) conducted NO and OH PLIF measurements using cavity-based flame-holders in a supersonic flow at a combustor Mach number of 2 and ethylene injection. For their mixing studies they added a small portion of NO to the fuel and captured a series of instantaneous NO PLIF images for different injection schemes. The results they present point out the effectiveness of fuel mixing for an injection scheme, where fuel is directly introduced into the cavity from its back wall. Apart from investigating the mixing capabilities of cavity flame-holders, they also conducted combustion studies using OH PLIF. For this purpose the fuel/air mixture was ignited using a spark plug, as their test conditions were not sufficient for auto-ignition. They investigated various injection schemes, whereas only the direct fuel injection into the cavity from the cavity back wall produced sustained cavity combustion. OH PLIF images were presented for this injection scheme for various equivalence ratios and back pressures.

Ben-Yakar et al. (1998) characterized the flame-holding process of a hydrogen jet injected into a high total enthalpy supersonic-cross-flow (flight-Mach number 13) simultaneously applying planar laser-induced fluorescence (PLIF) of OH and Schlieren imaging. The acquired and subsequently overlaid OH PLIF and Schlieren images indicated auto-ignition of the hydrogen jet in air cross-flow. OH fluorescence was measured in the recirculation region upstream of the jet extending along the outer edge of the jet plume adjacent to the wall. In the side view, decreasing OH PLIF signal was observed, beginning about 6-jet diameters downstream of the jet implying quenching of the ignition, however the results still showed potential for flame-holding.

1.1.7 Computational Fluid Dynamic Studies

Unfortunately ground test facilities like shock tunnels either do not exist in all the flight regimes covered by scramjet vehicles, or the experimental expense is simply too great for practical use. Hence, computational fluid dynamics (CFD) play a more and more important role in the design of scramjets. In recent years many different scramjet configurations have been simulated using CFD, and the development of test models and new vehicles such as the *X-43A* benefit from it.

Boyce et al. (2002) performed computational fluid dynamics calculations in support of the successful HyShot dual-combustor (fuel-on/fuel-off) scramjet flight experiment. Results from the scramjet experiment were used as input conditions for 3D combustion chamber calculations employing the finite-rate hydrogen/air chemistry model presented by Evans and Schexnayder (1979). A Mach 7.5 flight at an altitude 28 km and an angle of attack of $\pm 5^\circ$ was simulated. Their results predict significant pressure rises due to combustion for the combustor located windward comparing well with shock tunnel results at similar combustor inlet conditions, whereas the combustor located leeward did not experience the same pressure rise, unlike the corresponding tunnel results. This is presumably attributed to differences in combustor inlet temperature between the leeward CFD and shock tunnel combustors.

Baurle (2004) provides a detailed overview of the modeled equations typically employed by commercial CFD codes for high-speed reacting flows, as can be found in scramjet combustors. Approximations employed for turbulence and combustion modeling are covered in detail. State of the art models to close the unclosed terms in the averaged equation sets are presented and academic efforts addressing current shortcomings in order to improve these models are discussed.

1.2 Overview

This section briefly outlines the contents of this report and the research work conducted. The experimental work is split into two sections, each of which covers an experimental campaign. The first series of experiments was an initial survey of conditions using static pressure measurements. This work determined free stream conditions at which combustion will occur and determined axial pressure distributions along the combustor floor. The second series of experiments involved using planar laser-induced fluorescence of OH to investigate the effect of fuel type and equivalence ratio on location and intensity of hydroxyl radical production.

Chapter 2 describes the apparatus involved in the experiments. The T3 free-piston shock tunnel facility is described, concentrating on its configuration and operation. The method of determining initial flow properties such as nozzle reservoir and free stream conditions is also

outlined. The scramjet combustor used for the experiments is described, defining important parameters and detailing the geometry and instrumentation of the model. Chapter 2 also briefly describes how the equivalent flight Mach number was determined. The calibration and the calculation of equivalence ratios are also detailed, along with an explanation of how the injection system for the ANU scramjet combustor model operates. The final section of Chapter 2 describes the apparatus used to perform the OH PLIF experiments presented in Chapter 5, as well as the methodology used to acquire and reduce the data.

Chapter 3 describes and presents results for the initial experimental campaign, consisting of floor static pressure measurements for a range of equivalence ratios using both ethylene and hydrogen fuels. This initial experimental campaign was performed to acquire wall pressure distributions to determine the axial location and extent of combustion in the presence of the cavity fuel injection system for the specified range of equivalence ratios and fuels. These experiments helped determine the most useful equivalence ratios and test times for performing the OH PLIF experiments in Chapter 5.

Chapter 4 is a collection of preliminary experiments that were necessary to ensure that the main OH PLIF experiments were performed consistently and precisely. It is particularly important to ensure that the signal is proportional to OH concentration. These experiments include measurements of saturation irradiance and laser-sheet thickness, calibrations of the ICCD camera and LIF excitation repeatability experiments. Chapter 4 also presents the numerical model used for the CFD simulations and provides an overview of initial and boundary condition applied.

Chapter 5 presents and discusses the main experimental and computational findings of the report, starting with a description of the experimental procedure for the OH PLIF and pressure measurements and the data reduction process conducted. Subsequently the experimental and computational results for different flow conditions are presented and compared among each other.

Chapter 6 summarizes the main conclusions drawn from experiments and CFD simulations and recommends ways in which the work may be meaningfully continued.

Chapter 2

Experimental Apparatus and Procedures

This chapter describes the experimental apparatus used to generate the flow conditions, the scramjet and its fuel injection system, and the PLIF system used for visualizations. Care has been taken to determine as precisely as possible the nozzle exit flow conditions, and issues that contribute to the uncertainty in inlet flow conditions are discussed.

This chapter also describes the procedures used to acquire pressure traces and PLIF images for the experimental campaign. The procedures used to correct the PLIF images for scatter and spatial non-uniformity and the data reduction procedure used to compute time-resolved static pressure distributions are discussed in Section 2.5.

2.1 The T3 Free-Piston-Driven Shock Tunnel

As flight Mach number and stagnation enthalpy increase, it becomes more difficult and expensive to simulate flow conditions using continuously running facilities. Pulsed facilities allow relatively inexpensive simulation of free stream conditions at high flight Mach number conditions. These facilities increase the enthalpy of the flow at the cost of a reduced flow time. The current experiments were performed in one such pulsed facility: the T3 free-piston shock tunnel.

The free-piston-driven shock tunnel was developed by at the Australian National University (ANU) in the 1960s (Stalker 1967) and has proved to be a very successful facility for investigating hypersonic flows. T3 is one of a series of free-piston-driven shock tunnels built at the ANU (Stalker 1972). In more recent times, similar facilities have been developed in the United States, Germany, Japan and elsewhere. The major components of the free-piston shock tunnel are outlined in Figure 2.1.

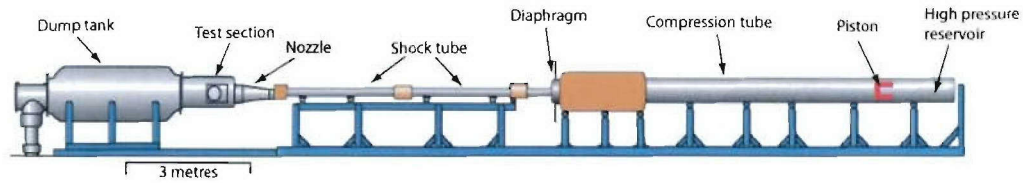


Figure 2.1: Schematic of the T3 free-piston-driven shock tunnel

The main components of the facility are shown in the figure. The *high pressure reservoir* and the *compression tube* are forged as an integral nine-meter-long stainless steel tube. The high-pressure reservoir is 3 meters long, the compression tube is 6 meters long. The reservoir's inner diameter is 340 mm, while the compression tube has an inner diameter of 300 mm. The compression tube is reinforced at its downstream end by a two-meter-long steel sleeve with 760 mm outer diameter, to ensure that it can withstand the extremely high pressures experienced during tunnel operation. A steel *diaphragm* separates the compression tube from the shock tube and hence the driver gas from the test gas. Material and thickness of the diaphragm are dictated by the initial driver conditions and the desired test conditions. The diaphragms used in these tests came from a single batch, were manufactured from mild steel, were 1.854-mm thick and had a burst pressure of 28.3 ± 0.7 MPa.

The six-meter *shock tube* has an inner diameter of 76 mm, and contains the test gas. In these tests, the tunnel is operated in reflected-shock mode, so the shock tube is separated from the *nozzle* by a 0.05-mm-thick mylar diaphragm located at the throat. To generate different flow Mach numbers in the test section, various conical and contoured nozzles are available. For these experiments a contoured nominal-Mach-4 Laval nozzle was used. The compression tube and the shock tube with the attached nozzle are placed on rollers to allow the facility to recoil during a tunnel run.

Models to be investigated are mounted in the $480 \times 480 \times 680$ mm (height \times width \times depth) *test section*, providing optical access through UV grade fused silica windows on either side and on top. Signals from the pressure transducers in the model leave the test section through a flange in the bottom wall. During tunnel operation the exhaust flow is collected in the *dump tank*, which is 3 meters long, has a diameter of 1.2 m and a volume of 3.500 m^3 .

2.1.1 Shock Tunnel Operation

Before operation, the compression tube, shock tube and dump tank are evacuated and subsequently filled with test and driver gases to their initial conditions, as described in Section 2.1.2. The choice of the test gas is governed by the desired gas for the experiments. The compression

tube contains a low-pressure driver gas mixture of helium and argon, chosen for its high sound speed and because it is chemically inert. The composition ratio of the driver gas has been chosen to achieve a properly tailored reservoir trace (Sudani et al. 2000). The reservoir behind the piston is filled with air at high pressure. A small evacuated volume, the *piston space*, separates the high pressure reservoir and the piston launcher, preventing the piston from launching.

When the reservoir pressure reaches its final value, the piston space is vented to a higher pressure. The pressure rise behind the piston causes it to launch. The piston accelerates and consequently adiabatically compresses the driver gas in the compression tube, increasing pressure and temperature of the driver gas. When the piston reaches the end of the compression tube, the driver gas pressure exceeds the burst pressure of the metal diaphragm. By then the piston has transferred almost all of its kinetic energy to the driver gas, the remaining portion is absorbed by polyurethane buffers, which stop the piston at the end of the compression tube.

The bursting diaphragm allows the driver gas to enter the shock tube, forming a strong normal shock wave that propagates along the shock tube. This shock wave adiabatically compresses and heats the initially cool and stationary test gas. Upon reaching the downstream end of the shock tube, the shock wave is reflected and also ruptures the mylar diaphragm at the nozzle entrance. The reflected shock travels back through the shock tube again, decelerating the test gas to come to rest, and further increasing its pressure and temperature. The resulting conditions upstream of the nozzle are approximately the stagnation conditions, supplying the nozzle with a high-temperature and high-pressure flow.

Due to the large pressure difference between the nozzle reservoir and the nozzle exit, the test gas starts flowing through the nozzle, which is shaped to generate the desired Mach number in the test section. After the starting process completes, quasi-steady flow exists in the test section until arrival of driver gas in the test section determines the end of the facility test time. More thorough descriptions of the shock tunnel operation are provided in Stalker (1972) and Gai (1992).

2.1.2 Tunnel Fill Conditions

Table 2.1 summarizes the gas compositions and fill pressures for the experiments described in this report. The composition of the driver gas was chosen to be 80% helium and 20% argon, the shock tube was filled with air at a pressure of 50 kPa. Values for the fill pressures were chosen to ensure a volumetric compression ratio, λ , of approximately 30 and a shock tube constant, K , of between 4 and 6. The latter value is chosen to ensure that the piston is fully decelerated when it reaches the end of the compression tube (Gai 1992).

R (MPa)	C (kPa)	D (MPa)	$\lambda = \left(\frac{D}{C}\right)^{\frac{1}{\gamma}}$	$K = \frac{R\lambda}{D}$
4.24	95.2	29.0	30.9	4.5

Table 2.1: Reservoir fill pressure R , compression tube fill pressure C , diaphragm burst pressure D , compression ratio λ and shock tube constant K for all experiments

2.1.3 Nozzle Reservoir Conditions

T3 is a pulsed facility and thus the test time is limited by the volume of the shock tube and the mass flow rate through the nozzle. Constant-pressure test times are typically between 0.5 and 2 ms, depending on the stagnation enthalpy. Higher enthalpy conditions tend to have lower constant-pressure test times. Two major effects reduce the usable test time of the shock tunnel: the time required to generate a uniform flow at the nozzle exit and the contamination of the test gas by the arrival of driver gas in the nozzle flow. Previous work in T3 by O'Byrne (1997) at a stagnation enthalpy of 4 MJ/kg, and using the time-variation of Mach angle in a duct, showed that driver gas contamination did not occur until more than 4 ms after shock reflection. Studies using a time-of-flight mass spectrometer in the T4 shock tunnel at the university of Queensland show that 10% levels of contamination do not occur until approximately 5 ms after shock reflection, and that this time reduces to 2.5 ms at 6MJ/kg(Paull 1996). Therefore the free stream flow should be free of driver gas at the test time of 1.5 ms used for these experiments.

Figure 2.2 is an example of a typical nozzle reservoir pressure trace. The pressure in the nozzle reservoir increases to 3 MPa when the initial shock wave first reaches it. Then the reflected shock wave passes, causing a further two-stage increase, initially to 12.5 MPa and less than 50 μ s later to its peak value. This two-stage pressure rise is most likely due to a bifurcated reflected shock formed by interaction of the reflected shock with the boundary layer. After an expansion phase during flow establishment in the nozzle, a period of almost constant nozzle reservoir pressure ensues, followed by a linear pressure decay. This pressure decay is caused either by the drainage of driver gas through the nozzle or by *under-tailored* shock tunnel operation.

For these experiments, a nominal test time of 500 μ s between 1.25 ms and 1.75 ms after shock reflection was chosen. The laser used for the PLIF imaging was pulsed 1.5 ms after the reflected shock wave. The test time t_{test} was chosen to ensure that the nozzle flow has had sufficient time to establish but that no driver gas has yet contaminated the flow. It is also important to ensure that the combustion flow reaches a quasi-steady state for the tests. Plots comparing the static pressure distribution as a function of distance along the duct for injection into air and injection into nitrogen show that the inlet pressure for each case is the same after approximately 1.2 ms. Plots of the ratio of static pressure to the nozzle reservoir pressure also

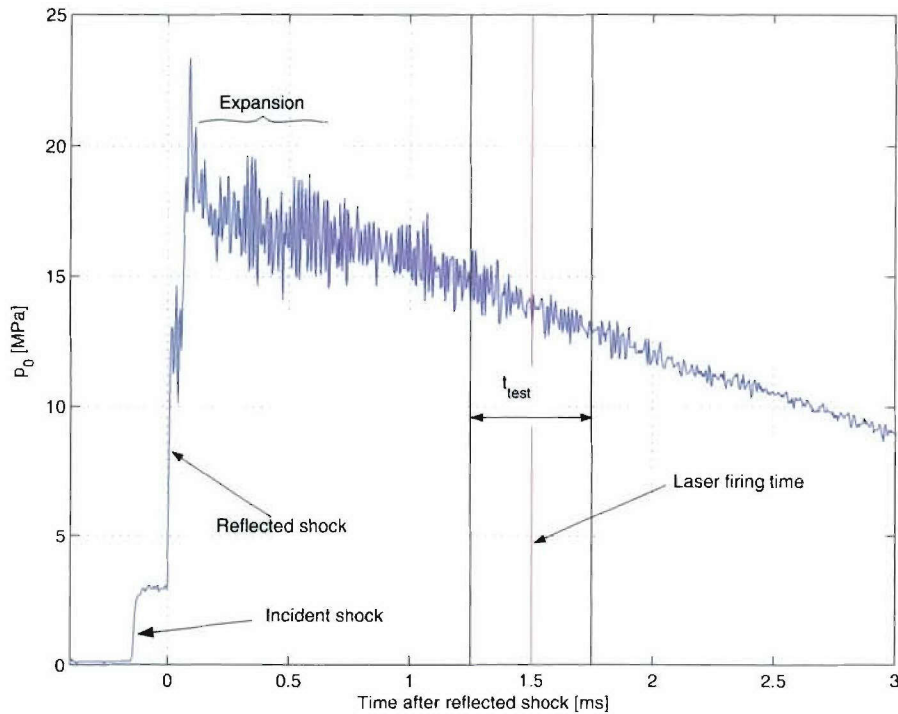


Figure 2.2: Typical nozzle-reservoir trace, showing the time of laser firing and the chosen test time.

indicate that this ratio reaches a steady state by 1.5 ms after shock reflection. It is apparent from Fig. 2.2 that the reservoir pressure has dropped from the plateau value of 16 MPa to approximately 14 MPa by 1.5 ms after shock reflection.

The nozzle reservoir conditions for the test time can be calculated if, besides the initial conditions, two further quantities are known: the nozzle reservoir pressure p_0 and the initial shock velocity v_{shock} . The nozzle reservoir pressure is measured using a Piezotronics PCB pressure transducer (type 113A22) (see Table 2.4) mounted at the end of the shock tube. The nozzle reservoir signal generated for each tunnel run is recorded using a digital storage oscilloscope. The shock velocity can be calculated using the measured time the incident shock wave takes to travel from another transducer located 1.435 m upstream of the nozzle reservoir transducer. Note that this measurement assumes constant shock propagation speed and therefore does not account for any attenuation in shock speed as the shock wave approaches the shock tube end-wall.

Measurements of shock velocities and reservoir pressures allow run-to-run variations in the nozzle reservoir conditions to be quantified. These fluctuations have a number of different causes: variations in the piston motion due to leakage of high-pressure reservoir gas; friction differences between the piston and the walls of the compression tube as the piston rings wear out; varying burst pressures between individual diaphragms; and run-to-run changes in high-

pressure reservoir, compression tube and shock tube fill pressures. The effects of these variations for the current experiments are shown in the histograms in Figure 2.3. These histograms

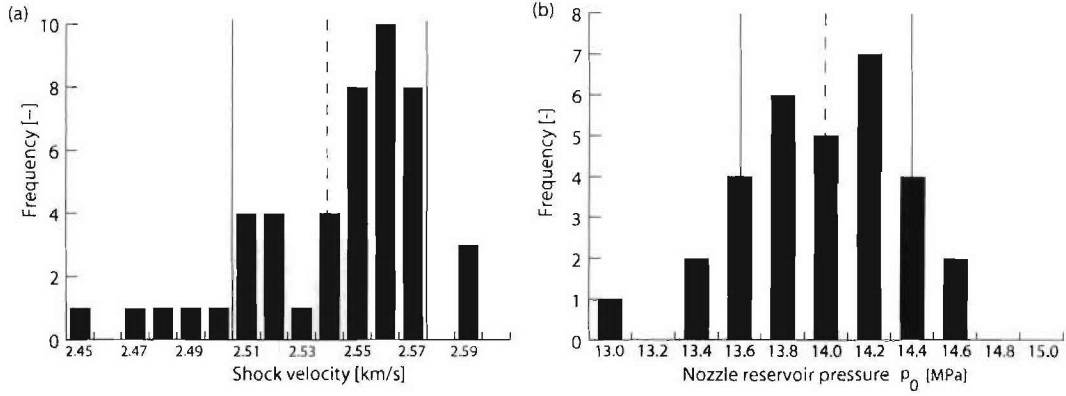


Figure 2.3: Histograms showing the variability of (a) the shock velocity and (b) the nozzle reservoir pressure. The solid vertical lines indicate one standard deviation either side of the mean value (dashed lines).

show the variations of the shock velocity and the nozzle reservoir pressure over a representative sample of 47 tunnel runs for the shock speed and 30 runs for the nozzle reservoir pressure. The vertical black lines indicate ± 1 standard deviation from the mean value (dashed blue lines) of the measurements. The standard deviation in the shock velocity is ± 0.034 km/s ($\pm 1.3\%$) while the nozzle reservoir pressure has a deviation of ± 0.3 MPa ($\pm 2.5\%$).

The nozzle reservoir (stagnation) temperature T_0 and hence the stagnation enthalpy h_0 are calculated using the ESTC (equilibrium shock tube calculation) code (M^CIntosh 1968). The ESTC code solves the inviscid, one-dimensional shock tube equation (Gaydon and Hurlé 1963) for a reflected shock with the primary shock velocity given by the measured shock velocity. The reflected shock conditions are then isentropically expanded until the static pressure matches the measured nozzle reservoir pressure. The calculation results, assuming chemical and vibrational equilibrium, are summarized in Table 2.2. The quoted uncertainties are the standard deviations, based upon the standard deviations in the measured nozzle reservoir pressures and shock speeds. Table 2.2 provides conditions at both 1.0 and 1.5 ms after shock reflection, corresponding to the constant-pressure reservoir conditions and the conditions at the nominal test time, when the OH PLIF images were obtained.

2.1.4 Freestream Conditions

Since the scramjet model is a semi-direct-connect one, has no intake ramp and therefore does not compress the incoming air, the shock tunnel is configured to deliver an airflow analogous

Time (ms)	p_0 (MPa)	T_0 (K)	h_0 (MJ/kg)
1.0	15.6 ± 0.4	4330 ± 30	6.28 ± 0.08
1.5	14.0 ± 0.4	4255 ± 30	6.14 ± 0.08

Table 2.2: Computed temperature T_0 , pressure p_0 and enthalpy h_0 in the nozzle reservoir.

to the flow that would be present at the entrance of a real combustor after intake compression. The flow conditions at the model inlet/nozzle exit are determined using the STUBE code (Vardavas 1984). This is a one-dimensional, inviscid nozzle code, specifically designed for use in determining free-piston shock tunnel freestream conditions. It assumes one-dimensional, inviscid nozzle flow, and incorporates finite-rate chemistry and vibrational non-equilibrium. STUBE uses the values calculated by the ESTC code as input quantities and determines the chemical composition and the state variables of the nozzle flow as a function of axial distance. Since the calculation is inviscid, the effects of boundary layer formation in the nozzle are not accounted for. In order to correct for the displacement effect, Pitot pressure was measured at the nozzle exit. The ratio of Pitot pressure to nozzle reservoir pressure was 0.1225. The inviscid nozzle location at which the calculated ratio of Pitot to reservoir pressure corresponded to this value was taken to be the area ratio corrected for boundary layer growth. For the Mach 4 contoured nozzle used in these tests, the geometrical exit-to-throat area ratio was 12.96, while the effective area ratio accounting for the displacement thickness was 12.79.

One difficulty associated with predicting the thermal state of the freestream in shock tunnel facilities is that the expansion is nearly always sudden enough to cause vibrational freezing in the flow. Vibrational freezing occurs when the number of collisions between molecules is not sufficient to allow the vibrational energy to reach equilibrium (Bray 1969, Hurle 1971). Vibrationally frozen nozzle flows will have a lower rotational temperature at the nozzle exit than an equivalent equilibrium flow. Previous laser-diagnostic studies in free-piston shock tunnels at the ANU (O'Byrne et al. 2002, Fraval et al. 2001) show that vibrational temperatures, and particularly those of nitrogen, are elevated well above the rotational temperature at the nozzle exit. STUBE uses the correlation of Millikan and White (1963) to determine the vibrational freezing temperatures for the major flow species, assuming collision with nitrogen to be the only vibrational relaxation process. For the contoured nozzle used in this investigation, STUBE predicts a freezing temperature of 2468 K for nitrogen, while oxygen and nitric oxide remain in equilibrium throughout the nozzle.

STUBE calculates pressure, temperature, density, velocity, frozen Mach number and species mole fraction as a function of axial distance along the nozzle. The freestream quantities at the scramjet intake — pressure p_∞ , temperature T_∞ , density ρ_∞ , velocity v_∞ and Mach number M_∞ — are listed in Table 2.3.

When the pressure measurements from this investigation were presented by Neely et al. (2003), the flow was assumed to be vibrationally frozen at the nozzle reservoir conditions. This calculation produces a much lower rotational temperature at the nozzle exit. If these values are used in a thermal equilibrium CFD code like CFD++[®], the excess vibrational energy will be lost to that computation. For this reason, Table 2.3 contains STUBE calculation results for both vibrationally frozen and equilibrium nozzle flow. Equilibrium CFD codes should use the equilibrium STUBE results, to account for all the energy in the flow. In the absence of a true nonequilibrium calculation, this procedure is the best alternative, because the pressure increase in the combustor should cause the flow to come to vibrational equilibrium somewhere within the combustor. It should also be noted from Table 2.3 that a significant amount of dissociated oxygen and nitric oxide exists in the freestream. This is a characteristic of free-piston shock tunnel flows. While it is difficult to quantify the effect of the extra atomic species on the flow, combustion is in general more likely to occur when atomic oxygen is present in the flow (Odam 2004).

The temperatures and pressures predicted by STUBE are sufficient for auto-ignition within the combustor, and therefore no external measures are required to initiate combustion.

Calculation	p_{∞} (kPa)	T_{∞} (K)	ρ_{∞} (kg/m ³)	v_{∞} (m/s)	M_{∞}
Vib. nonequilibrium	88 ± 2	1410 ± 30	0.217 ± 0.007	2885 ± 20	3.74 ± 0.03
Vib. equilibrium	98 ± 2	1563 ± 30	0.217 ± 0.007	2880 ± 20	3.96 ± 0.03
Mole Fractions	N_2	O_2	NO	O	
	0.755	0.174	0.063	0.0078	

Table 2.3: Calculated freestream conditions

The freestream conditions used for this study were chosen to approximately match a Mach 11.5 flight at an altitude of about 29 km. At this altitude, the temperature of the international standard atmosphere is approximately 225 K, and therefore the sound speed and static enthalpy are defined. From these quantities and the total enthalpy presented in Table 2.2, the Mach number can be determined directly.

2.2 The Cavity Flame-Holder Scramjet

The introduction of a cavity flame-holder into the duct of a supersonic combustor increases its mixing and flame-holding capabilities, as described in Section 1.1. We now describe in more detail the cavity flame-holder scramjet and the instrumentation used in the experiments.

2.2.1 The Experimental Scramjet Combustor Model

As mentioned previously, the scramjet is a generic, semi-direct-connect combustion chamber. No intake compression ramp or exhaust nozzle were included, since the focus of the research was on the combustion process and not on the overall aerodynamic performance. The model consists of a 500-mm-long rectangular duct with a constant cross-section of 52 mm \times 25 mm, incorporating a single full-width cavity flame-holder located 152.5 mm downstream of the inlet leading edge. The cavity dimensions were chosen to be a sub-scale version of the configuration employed by Gruber et al. (2001), enabling data comparison to be made by WPRL at a later date. The cavity has a rear angle of 22.5° and a length-to-depth ratio of 4.8. Both values are in the suggested range to produce an open cavity with stable recirculation (Ben-Yakar and Hanson 2001). The scramjet inlet was located 10-mm downstream of the nozzle exit after recoil. This cavity nominally matches the cavity used in experiments conducted at the Wright-Patterson Air Force Research Laboratories in the flight Mach number range of 4–6.7.

Hydrogen or ethylene fuel is introduced to the cavity from ports in the rear, angled cavity step. The fuel is injected through four cylindrical ports, each having a diameter of 2 mm and located at the half-depth of the cavity. Figure 2.4 illustrates the scramjet geometry. Optical access to the combustor is provided by two UV-grade fused silica windows, mounted on the top and side walls. The laser sheet is directed through the top window, as described in Section 2.4. Two wedge-shaped shields were placed around the side-windows of the scramjet, to prevent the oncoming nozzle flow from disturbing the camera's view into the combustion chamber. This significantly decreases the tunnel luminosity signal, which otherwise would deteriorate the signal-to-noise ratio of the PLIF measurements.

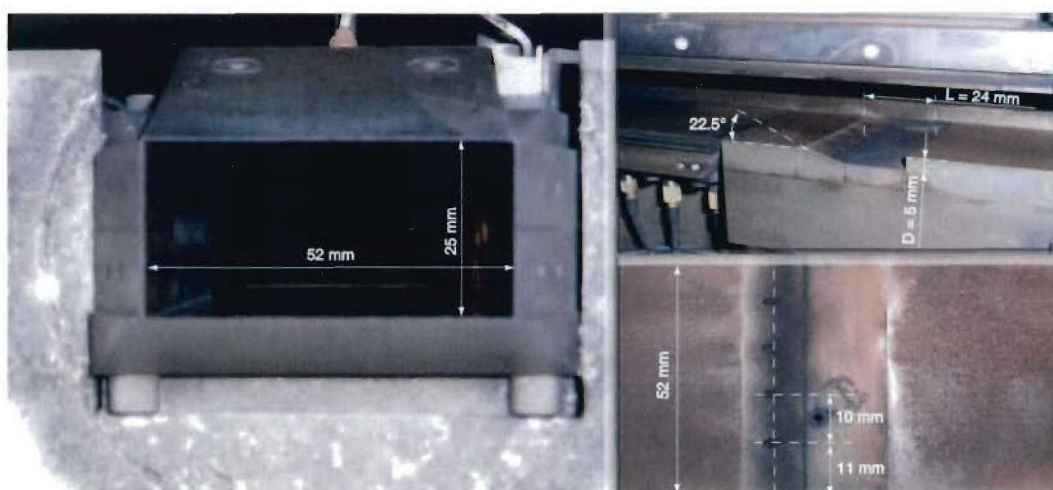


Figure 2.4: Scramjet inlet cross-section (left) and cavity dimensions (right)

2.2.1.1 Instrumentation

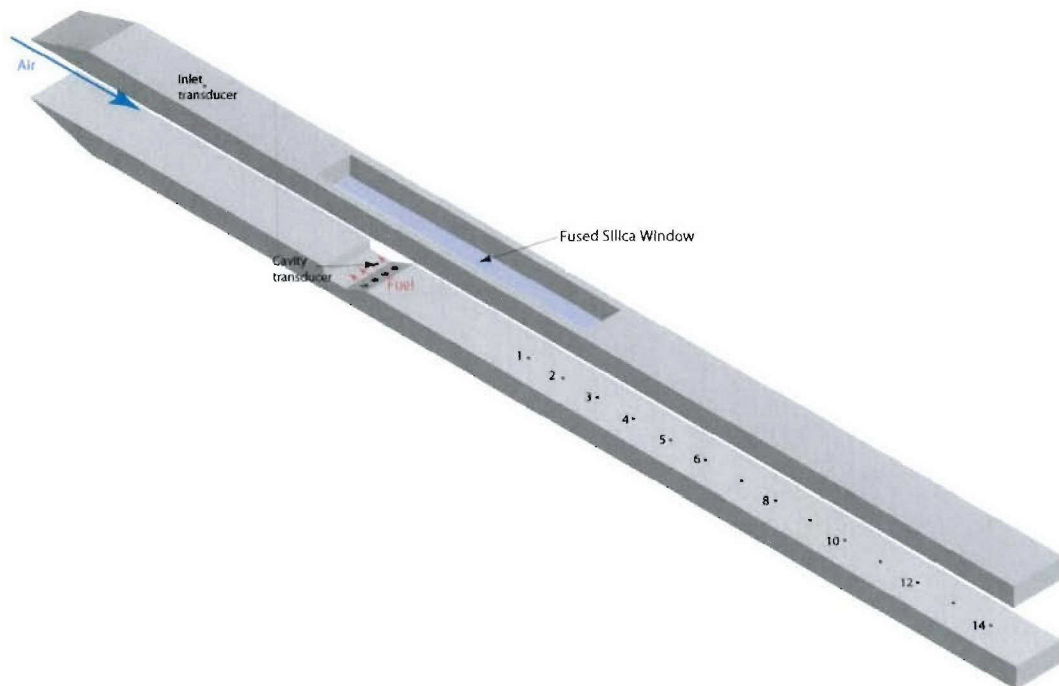


Figure 2.5: Positions of the piezoelectric pressure transducers

The scramjet model was instrumented with multiple piezoelectric pressure transducers, whose positions are shown in Figure 2.5. The first of these transducers, referred to as the inlet transducer, is located 52 mm downstream of the scramjet intake and mounted on the top of the duct, followed by the cavity transducer, mounted 10 mm off-center across the duct and 170 mm downstream of the inlet on the cavity floor. Downstream of the cavity trailing edge a further ten transducers, labeled transducers 1 to 14 according to their positions in the duct, measured floor static pressure. With the exception of the cavity transducer, all transducers were located in the center of the duct.

Transducer 1 is located 232 mm downstream of the inlet, the subsequent five transducer are each spaced 20 mm apart. Between transducers 6 and 8 the spacing is increased to 40 mm, leaving one available mount empty between transducers. The pressure traces were recorded using a series of digital storage oscilloscopes. Table 2.4 provides an overview of the technical specifications of the pressure transducers used in the current experiments.

All transducers except the one at the inlet are mounted in the manner as shown in Figure 2.6. The inlet transducer, and to a lesser extent the cavity transducer were noisy compared with the others. The inlet transducer was found to be noisy because space restrictions required it to be mounted at an angle and without using the vibration-reducing mounting method used for the floor transducers. Improvements to the mount used previously (Neely et al. 2003) and (Griffiths

2004) have been made in this study by introducing an additional rubber buffer between the inlet transducer's sensitive surface and the scramjet roof. The rear of the transducer and its connection to the recording devices were previously directly exposed to the air flowing around the scramjet at hypersonic speeds. Disturbances caused by this were alleviated by shielding it with a block of foam rubber.

Neely et al. (2003) and Griffiths (2004) also noted a negative signal output of several transducers mounted downstream of the cavity. This was most likely caused by the heat load from the hot gases introduced to the transducer's sensing surface, causing the transducer casing to widen and hence reducing the preload force on the piezoelectric crystals. An aluminum shim (see Figure 2.6 (b)) placed on top of each transducer prevented negative signals and thus improved the quality of the recorded pressure traces.

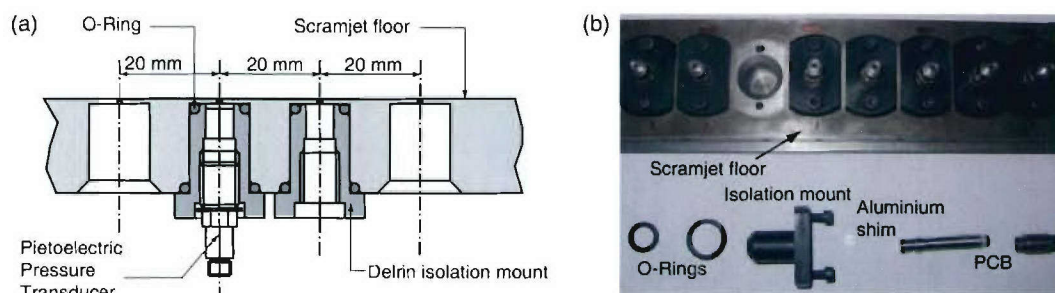


Figure 2.6: Details of the pressure transducer mounts: (a) schematic drawing (taken from (Gaston 2002)), (b) photograph of the disassembled transducer

Transducer	Distance from inlet (mm)	Piezotronics Model	Sensitivity (mV/kPa)
Stagnation	-	113A22	0.071
Injector	-	111A24	0.7174
Inlet	52	113A21	3.53
Cavity	170	113M165	7.25
1	232	113M165	7.61
2	252	113M165	7.63
3	272	113M165	7.47
4	292	113M165	7.89
5	312	113M165	7.59
6	332	113M165	7.63
8	372	113M165	7.53
10	412	113M165	7.45
12	452	113M165	7.57
14	492	113M165	7.63

Table 2.4: Specifications of the pressure transducers used for the experiments.

2.3 The Fuel Injection System

2.3.1 Functional Principle

The fuel injection system used for the experiments is based on a Ludwieg tube made from a spiral of copper tubing with a volume of $1.419 \times 10^{-3} \text{ m}^3$, shown schematically in Figure 2.7. Before each shot, the Ludwieg tube is filled to the desired pressure. For the existing system, the maximum fuel pressure is limited to 2500 kPa. This effectively limits the maximum global fuel/air equivalence ratio. When the shock tunnel is fired, the tunnel recoil triggers a fast-acting valve (Morgan and Stalker 1983) supplying fuel to the injection ports.

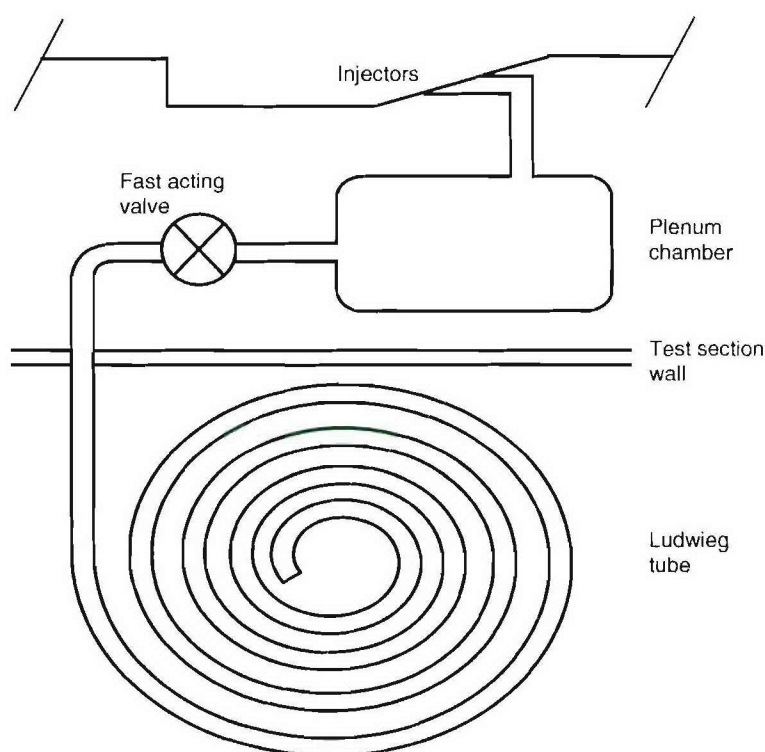


Figure 2.7: Fuel injection system (from (Griffiths 2004))

The fuel mass flux \dot{m}_{fuel} flowing through the injectors varies with time due to the decreasing Ludwieg tube pressure. During a facility run the pressure in the plenum chamber $p_m(t)$ is recorded. A typical pressure trace is shown in Figure 2.8. As Figure 2.8 shows, the fuel flow duration is approximately 100 ms; much longer than the tunnel flow duration. Figure 2.9 shows a magnified section of Figure 2.8 for the defined test time from 1.25 to 1.75 ms after shock reflection (Section 2.1) with the nozzle reservoir pressure trace. It indicates that the plenum pressure p_m and thus the fuel mass flux is essentially constant during this period. To obtain accurate values for the equivalence ratios it is necessary to determine the fuel mass flux

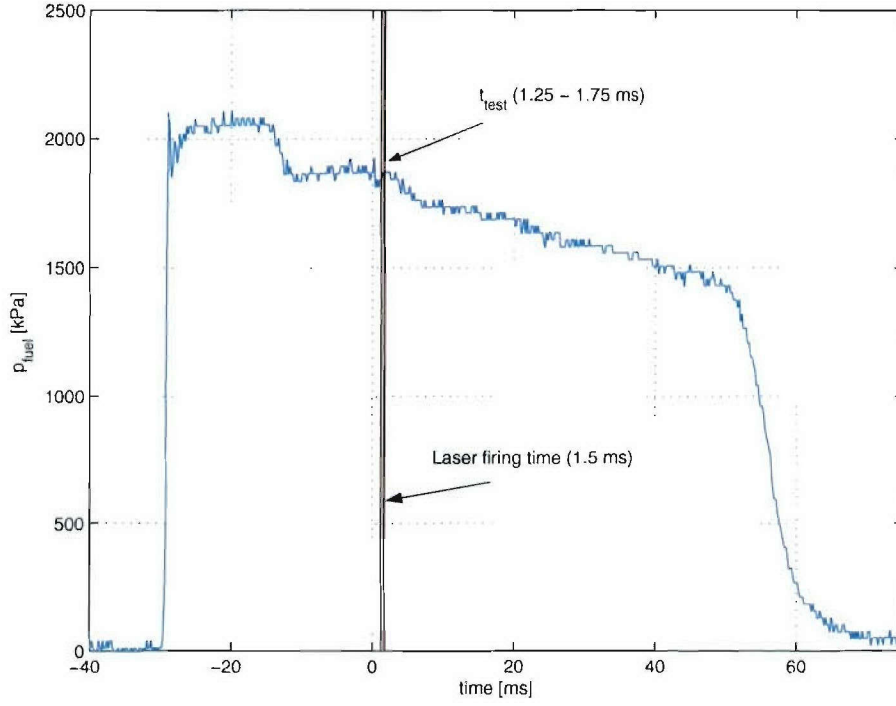


Figure 2.8: Typical fuel pressure trace, entire injection period

$\dot{m}_{fuel}(t)$ from the plenum pressure $p_m(t)$, and it is essential to know which initial Ludwig tube pressure p_i to choose to achieve the desired $\dot{m}_{fuel}(t)$ during the test time.

2.3.2 Calibration of the Fuel Injection System

The fuel mass flux at the throat, provided the throat is choked (with * indicating the conditions at the throat) and therefore the injection is sonic, is defined as:

$$\begin{aligned}\dot{m}_{fuel} &= \rho^* a^* A^* \\ &= \frac{p^* a^* A^*}{RT^*}\end{aligned}\tag{2.1}$$

With the definition of the speed of sound $a = \sqrt{\gamma RT}$ Equation 2.1 becomes

$$\begin{aligned}\dot{m}_{fuel} &= \sqrt{\frac{\gamma}{R}} \frac{p^* A^*}{\sqrt{T^*}} \\ &= c_1 \frac{p^*}{\sqrt{T^*}}\end{aligned}\tag{2.2}$$

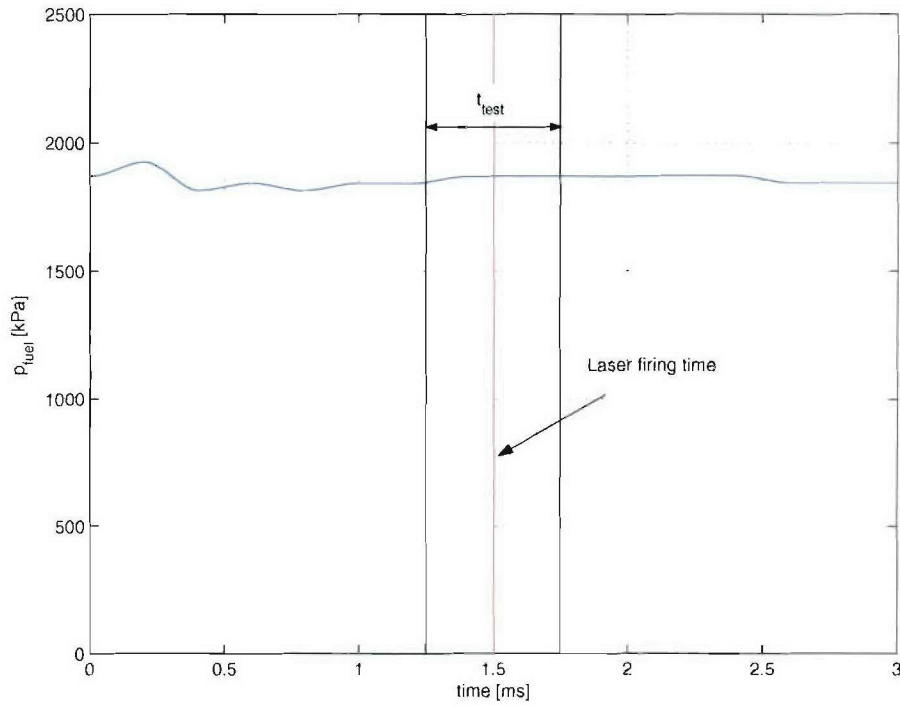


Figure 2.9: Typical fuel pressure trace, magnification

where $c_1 = \sqrt{\frac{2}{R}} A^*$ is a constant for a given injector geometry. Assuming isentropic flow in the Ludwieg tube and the rest of the injection system, the conditions can be referenced to the total pressure p_0 and the total temperature T_0 that initially existed in the Ludwieg tube. With

$$\frac{T_0}{T} = \left(\frac{p_0}{p} \right)^{\frac{\gamma-1}{\gamma}} \quad (2.3)$$

Equation 2.2 can be written as:

$$\dot{m}_{fuel} = c_1 \frac{p^*}{\sqrt{T_0}} \left(\frac{p_0}{p^*} \right)^{\frac{\gamma-1}{2\gamma}} \quad (2.4)$$

or with the introduction of the constant $c_2 = \frac{c_1}{\sqrt{T_0}} p_0^{\frac{\gamma-1}{2\gamma}}$ Equation 2.4 simplifies to:

$$\dot{m}_{fuel} = c_2 p^{*\frac{\gamma+1}{2\gamma}} \quad (2.5)$$

The total fuel mass Δm_{fuel} which has passed through the injectors can be calculated by integrating Equation 2.5 and with the definition of the mass flux $\dot{m} = \frac{dm}{dt}$ it becomes:

$$\Delta m_{fuel} = c_2 \int_0^t p^*{}^{\frac{\gamma+1}{2\gamma}} dt \quad (2.6)$$

The total fuel mass Δm_{fuel} delivered into the scramjet corresponds to the mass loss of the Ludwig tube. This mass loss can be written as

$$\begin{aligned} \Delta m_{fuel} &= m_i - m_f \\ &= (p_i - p_f) \frac{V}{RT_0} \end{aligned} \quad (2.7)$$

where m_i is the initial and m_f the final fuel mass; p_i is the initial and p_f the final Ludwig tube pressure; V is the Ludwig tube volume upstream of the fast-acting valve (see Figure 2.7); and R is the gas constant for the fuel. Hence Equations 2.5 and 2.6 result in:

$$\dot{m}_{fuel} = (p_i - p_f) \frac{V}{RT_0} \frac{p^*{}^{\frac{\gamma+1}{2\gamma}}}{\int_0^t p^*{}^{\frac{\gamma+1}{2\gamma}} dt} \quad (2.8)$$

As the “*” indicates, p^* is the pressure at the (choked) throat. Its ratio to the plenum pressure p_m , which is the pressure actually measured during a tunnel run, can again be determined from the isentropic relations as follows (Anderson 1990):

$$\frac{p_0}{p_m} = \left(1 + \frac{\gamma-1}{2} M^2\right)^{\frac{\gamma}{\gamma-1}} \quad (2.9)$$

$$\frac{p_0}{p^*} = \left(1 + \frac{\gamma-1}{2}\right)^{\frac{\gamma}{\gamma-1}} \quad (2.10)$$

$$\frac{p^*}{p_m} = \frac{\left(1 + \frac{\gamma-1}{2} M^2\right)^{\frac{\gamma}{\gamma-1}}}{\left(1 + \frac{\gamma-1}{2}\right)^{\frac{\gamma}{\gamma-1}}} \quad (2.11)$$

The flow in the plenum chamber is, by definition, subsonic. Also a large change in Mach number does not affect the ratio $\frac{p^*}{p_m}$ significantly. If the Mach number e.g. doubles from 0.2 to 0.4, the ratio only varies by 8.6% (for $\gamma = 1.4$). Thus the pressure ratio $\frac{p^*}{p_m}$ can be treated as a constant and hence Equation 2.8 becomes:

$$\dot{m}_{fuel} = (p_i - p_f) \frac{V}{RT_0} \frac{p_m^{\frac{\gamma+1}{2\gamma}}}{\int_0^t p_m^{\frac{\gamma+1}{2\gamma}} dt} \quad (2.12)$$

With this equation, the fuel mass flux $\dot{m}_{fuel}(t)$ can be accurately determined by recording the initial Ludwieg tube pressure p_i , the final Ludwieg tube pressure p_f and the history of the plenum pressure $p_m(t)$. Details of the pressure transducer used to acquire the plenum pressure traces can be found in Table 2.4. Table 2.5 gives an overview of the six different fuel conditions examined, for both hydrogen and ethylene fuels.

Hydrogen (H ₂)			
p_i (kPa)	2500	1420	954
\dot{m}_{fuel} (kg/s)	0.0114 ± 0.0004	0.0058 ± 0.0003	0.0037 ± 0.0003
uncertainty (%)	3.5	4.9	6.9
Ethylene (C ₂ H ₄)			
p_i (kPa)	2500	1454	508
\dot{m}_{fuel} (kg/s)	0.0367 ± 0.0013	0.0214 ± 0.0009	0.0073 ± 0.0003
uncertainty (%)	3.5	4.0	3.5

Table 2.5: Fuel injection conditions: initial Ludwieg tube pressures p_i , fuel mass fluxes \dot{m}_{fuel} and uncertainties (%)

The mass fluxes are averaged for the test period between 1.25 and 1.75 ms. Since there were not very many tunnel runs carried out for each fuel condition (e.g. only 5 for the lowest ethylene equivalence ratio) the uncertainties are only indicative. However the scatter between these runs is 4–7%, which is quite reasonable.

Figure 2.10 shows the resulting fuel mass fluxes plotted over the initial Ludwieg tube fill pressure for both fuels with a linear curve fit applied to the measured data points. Note that for more accurate curve fits more shots at a greater spectrum of fill pressures are required, as performed by Neely et al. (2003). The differences between the mass fluxes presented in this report and those of Neely et al. (2003) are due to an implementation error in the previous work. The hydrogen mass fluxes are about 1.75 times higher, and the ethylene mass fluxes about 1.4 times higher, than reported by Neely et al. (2003) for the same injection pressure.

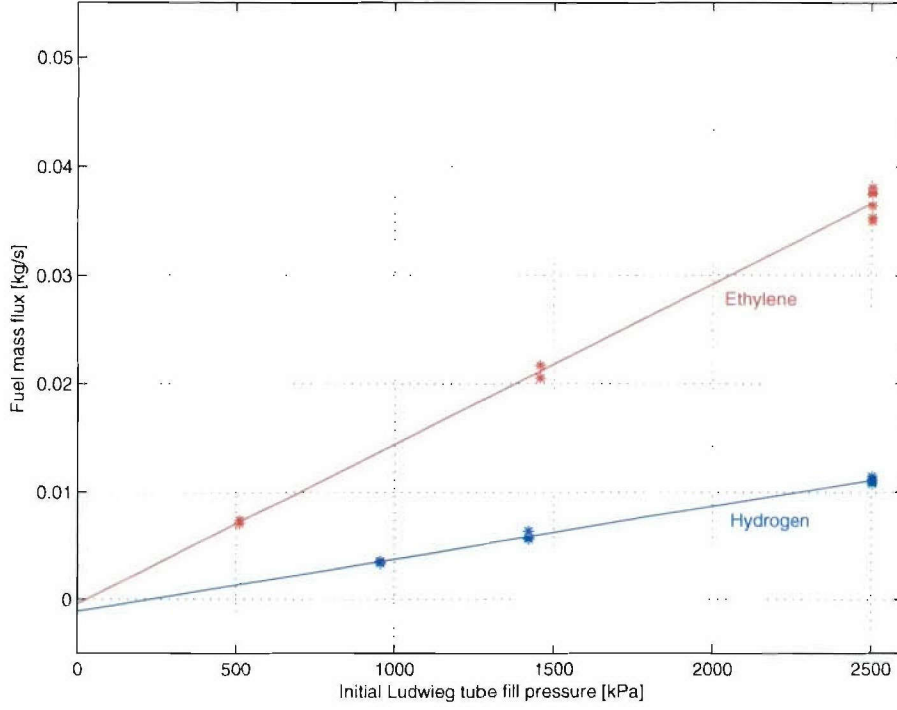
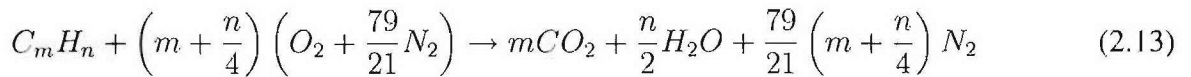


Figure 2.10: Fuel mass fluxes \dot{m}_{fuel} versus Ludwig tube fill pressure p_i , for hydrogen (blue) and ethylene (red)

2.3.3 Equivalence Ratio Calculation

Experimental data was acquired for different combustion conditions, for both hydrogen and ethylene fuels. The aim was to examine how different global fuel-air equivalence ratios influence the combustion process, through pressure and OH PLIF measurements. Considering a simple single-step hydrocarbon/air reaction set given by



where m and n are the number of hydrogen- and carbon-molecules (atomicities) in the fuel ($m = 0$ and $n = 2$ for pure hydrogen, $m = 2$ and $n = 4$ for ethylene respectively), the stoichiometric fuel/air ratio can be calculated. As can be seen in Equation 2.13, air was assumed to consist of 21% oxygen and 79% nitrogen. Accounting for the atomic weights of hydrogen ($M_H = 1\text{g/mol}$), carbon ($M_C = 12\text{g/mol}$), nitrogen ($M_N = 14\text{g/mol}$) and oxygen ($M_O = 16\text{g/mol}$), the stoichiometric fuel/air mass ratio $f_{st} = \frac{m_{fuel}}{m_{air}} = \frac{\dot{m}_{fuel}}{\dot{m}_{air}}$ directly derives from

Equation 2.13 to

$$f_{st} = \frac{mM_C + nM_H}{\left(m + \frac{n}{4}\right) \left(2M_O + 2\frac{79}{21}M_N\right)} = \frac{12m + n}{\left(m + \frac{n}{4}\right) \left(32 + 28\frac{79}{21}\right)} \quad (2.14)$$

For hydrogen (H_2) and ethylene (C_2H_4) this becomes $(f_{st})_{H_2} = 0.0291$, and $(f_{st})_{C_2H_4} = 0.0680$ respectively.

The equivalence ratio Φ is defined as the ratio of the actual fuel/air ratio f to the stoichiometric fuel/air ratio f_{st} . Therefore stoichiometric combustion results in $\Phi = 1$, whereas $\Phi < 1$ is fuel-lean and $\Phi > 1$ is fuel-rich. The experimentally obtained mass flux of air can be calculated from the freestream conditions (see Table 2.3) using the law of mass conservation given by

$$\dot{m}_{air} = \rho_{\infty} v_{\infty} A \quad (2.15)$$

where A is the inlet cross-section of the scramjet duct, with $A = 0.025 \text{ m} \times 0.052 \text{ m} = 0.0013 \text{ m}^2$. The air mass flux then results in $\dot{m}_{air} = 0.84 \pm 0.02 \text{ kg/s}$, whereas the corresponding fuel mass fluxes are accounted for using Equation 2.12 and listed in Table 2.5. From this the equivalence ratios can then be calculated using the equation

$$\Phi = \frac{f}{f_{st}} = \frac{\left(\frac{\dot{m}_{fuel}}{\dot{m}_{air}}\right)}{f_{st}} \quad (2.16)$$

The resulting equivalence ratio versus Ludwig tube fill pressure plots are shown in Figure 2.11. Note that both curves should actually pass through the origin. Since no calibration data was obtained for very low Ludwig tube fill pressures, the calibration curves are uncertain at low pressures. The equivalence ratios were calculated using the mean of both fuel and air mass fluxes. The stated uncertainties result from calculating equivalence ratios for the upper and lower limits of fuel and air and vice-versa. The results are summarized in Table 2.6.

The resulting equivalence ratio calibration curves are, for hydrogen $\Phi_{H_2} = -0.051 + (0.00021 \pm 0.00002) p_i$ and for ethylene $\Phi_{C_2H_4} = -0.00085 + (0.00026 \pm 0.00002) p_i$.

Note that originally the fill pressures were designed to permit a direct comparison of hydrogen and ethylene fuels at the same equivalence ratios. As already mentioned, a numerical error in the original calculation method led to a choice of conditions for which only the lower

equivalence ratios are similar enough to be considered a direct comparison. The maximum plenum pressure of 2500 kPa was dictated by the safe operating limit of the Ludwig tube delivery system.

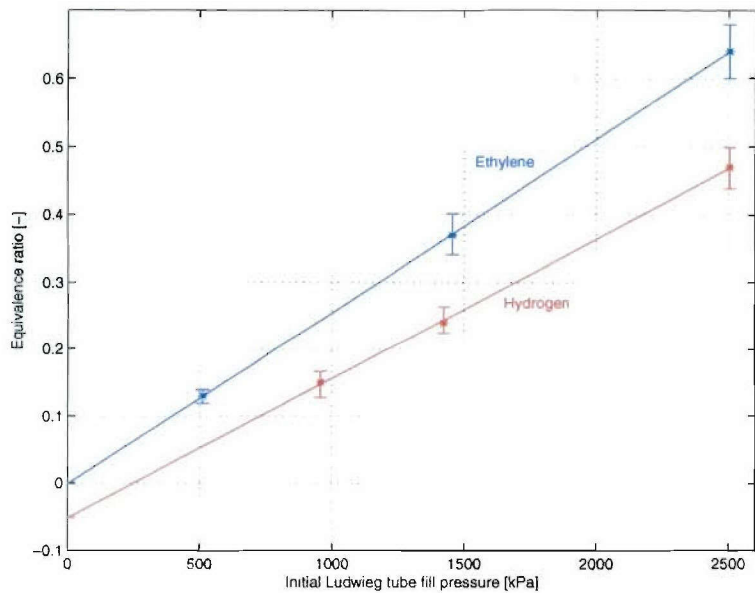


Figure 2.11: Equivalence ratio Φ versus Ludwig tube fill pressure p_i , for hydrogen (blue) and ethylene (red)

Hydrogen (H ₂)			
p_i (kPa)	2500	1420	954
Φ	0.47 ± 0.03	0.24 ± 0.02	0.15 ± 0.02
uncertainty (%)	6.0	7.7	10.7
Ethylene (C ₂ H ₄)			
p_i (kPa)	2500	1454	508
Φ	0.64 ± 0.04	0.37 ± 0.03	0.13 ± 0.01
uncertainty (%)	6.1	6.7	6.6

Table 2.6: Equivalence ratios Φ dependent on initial Ludwig tube pressures p_i and corresponding uncertainties (%)

2.4 PLIF Apparatus and Procedure

The OH PLIF system used for these experiments was very similar to that used for a previous OH PLIF investigation of supersonic combustion in a strut-based combustor geometry (M^cIntyre

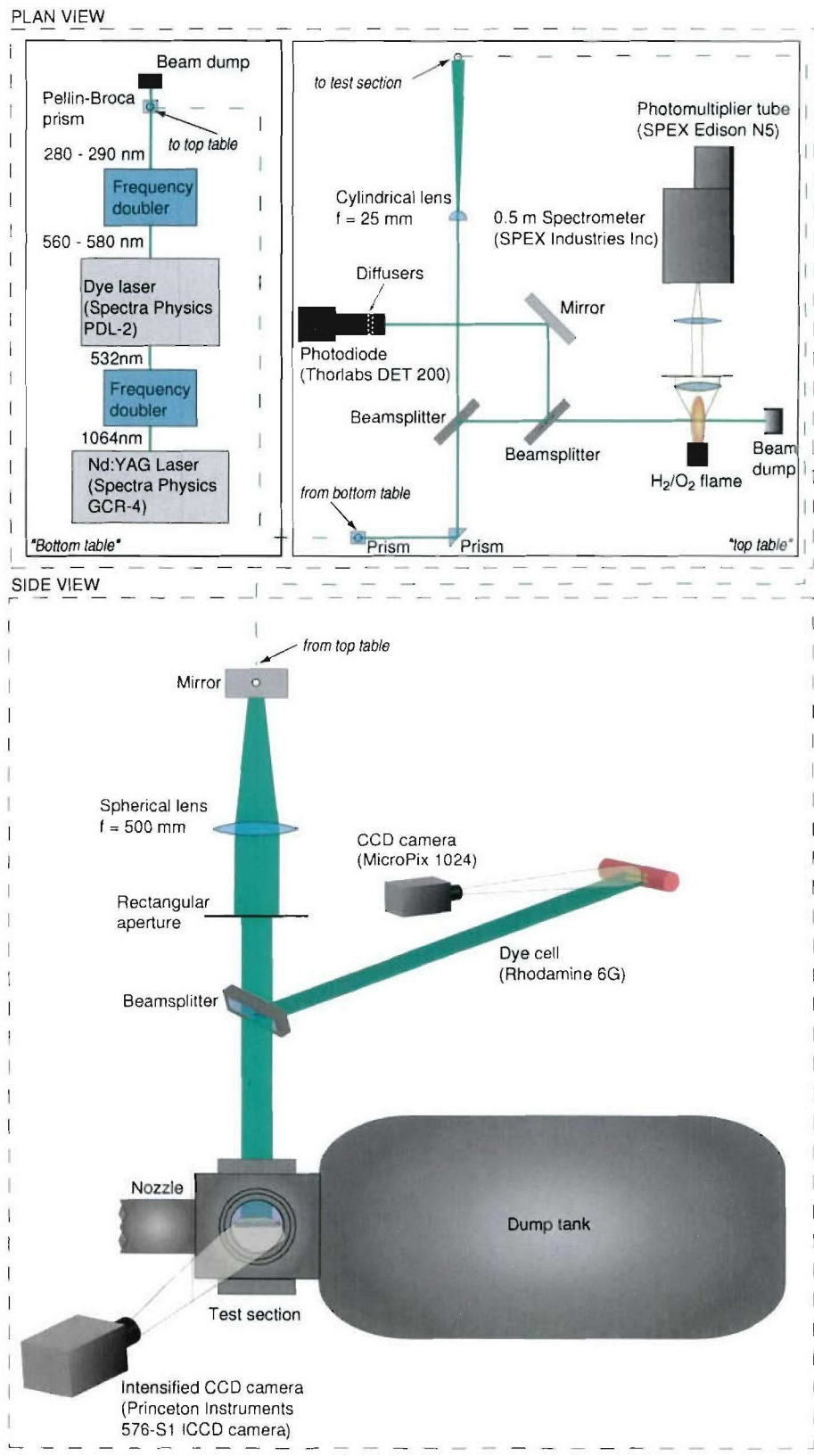


Figure 2.12: Experimental arrangement for the OH PLIF experiments.

et al. 1997). The only significant difference is that the current fluorescence measurements were made using a better ICCD camera (Princeton Instruments ICCD) with 16-bit dynamic range.

Figure 2.12 shows the apparatus used for acquiring the PLIF images discussed in Chapter 5. Transitions in the $A^2\Sigma^+ - X^2\Pi(1, 0)$ rovibronic band of OH were excited using a YAG-pumped frequency-doubled dye laser system. The required wavelengths were achieved by pumping a Spectra Physics PDL-2 dye laser with a Spectra Physics GCR-4 Nd:YAG laser. The Nd:YAG laser initially produces radiation at 1064 nm, frequency-doubled to 532 nm using a BBO doubling-crystal. The doubled output energy of the Nd:YAG laser is approximately 550 mJ. The dye laser uses a mixture of Rhodamine 590 and Rhodamine 610 dyes to produce 160 mJ of radiation between 560 and 580 nm.

The output of the dye laser is frequency-doubled to generate wavelengths from 280 to 290 nm. At the output of this doubling-crystal, the laser system produces UV radiation with energy between 10 and 20 mJ, depending on the dye age and concentration and the laser alignment. The desired wavelengths near 283 nm are generated by tuning the grating on the dye laser, while keeping the doubling crystal optimally aligned. The 283-nm beam is separated from the residual laser beams at 532 nm and 566 nm using a Pellin-Broca prism. These higher-wavelength beams are blocked with a beam dump. The Pellin-Broca prism also turns the ultra-violet beam 90° upward, to raise it to a level above the test section, to the upper table.

Before being spread out to form the PLIF laser sheet, the beam is split into three beams using two 10% beam splitters. The first beam splitter takes some energy from the main beam, and is split again. The first of the two low-energy beams excites OH fluorescence in a hydrogen/oxygen flame, to ensure tuning to the correct OH transition. The LIF signal in the flame is collected by a 0.5-m SPEX Industries Inc spectrometer and detected by a SPEX Edison N5 photomultiplier tube connected to the spectrometer. An excitation spectrum is produced by scanning across a number of absorption transitions prior to each tunnel run. The second minor beam is diverted to a Thorlabs DET 200 photodiode to correct for pulse-to-pulse variations in laser energy.

The laser sheet is formed by passing the laser beam through a convex cylindrical lens with a focal length $f = 25$ mm followed by a spherical lens with a focal length of $f = 500$ mm. The cylindrical lens expands the beam into one transverse direction, and after being reflected 90° downward by a mirror the laser sheet is collimated by the spherical lens and pointed towards the test section using a mirror. An aperture following the spherical lens creates sharply defined laser sheet edges and defines a sheet with a length of about 78 mm, which is more homogeneous in terms of its spatial energy distribution. The spherical lens also focuses the laser sheet. The sheet is located in such a way that the focus occurs before the sheet entered the duct, to reduce the likelihood of saturation of the fluorescence. Thus the sheet in the duct is very slightly diverging, although the effect is negligible over the 25-mm height of the duct. Measurements of the laser sheet thickness at the measurement location are presented in Section 4.2.1.

It is also important to know the spatial distribution of irradiance within the laser sheet, to correct the PLIF images for spatial non-uniformities. A fused silica window diverts 10% of the laser sheet intensity onto a quartz cell filled with Rhodamine 6G laser dye dissolved in methanol. The UV radiation causes the dye to fluoresce. The dye cell is located at the same distance from the beam splitter as the center of the scramjet duct. The fluorescing laser sheet profile is captured on a 1024 by 768 pixel MicroPix CCD camera. The energy distribution of the laser sheet is determined by the intensity of the dye fluorescence and the PLIF images presented in Chapter 5 are normalized to this distribution. This procedure will be discussed in Section 4.2.3.

The PLIF images are captured using a 576 by 384 pixel Princeton Instruments 576-S1 intensified CCD camera with a Nikon UV-Nikkor f 4.5 lens, imaging perpendicular to the laser sheet, which is in the focal plane of the ICCD camera. A 2-mm Schott UG11 filter, which passes wavelengths between 240 and 400 nm, and a 2 mm Schott WG305 filter, which passes wavelengths >305 nm are placed in front of the camera. These filters block most of the broad-band flow luminosity and the elastic laser scatter from the flow and the floor of the scramjet, while most of the fluorescence signal reaches the camera, thus improving the image quality significantly. The camera is interfaced to a Pentium-class PC, and the camera acquisition speed limits us to single image acquisitions for each tunnel run.

2.4.1 Tunnel Run Procedure

Before each experimental run all UV fused silica windows are cleaned to ensure that the laser energy and detected fluorescence signal is optimal and repeatable between tunnel runs. Experience has shown that even small deposits on windows of soot and other particulates caused by running the facility is absorbed strongly in the UV. The ICCD camera and the Nd:YAG laser are flushed with nitrogen and the laser is run to check the correct location of the laser sheet in the scramjet duct. If necessary, the ICCD camera is refocused onto this plane using a grid positioned at the laser sheet position as described in Section 4.2.6. After this, the windows are put back in place, the test section is sealed and the shock tunnel is then reloaded and pumped down for about 45 minutes. The final pressure in the test section and the dump tank is about 13 Pa. The laser is turned on again to warm up ensuring stable operation at warm operation conditions. The laser system is run for 20–30 minutes at 10 Hz before the experiment. A LIF excitation scan is performed in a hydrogen/oxygen-flame (as described in Section 4.2.4) to identify the correct transition to which the laser is subsequently tuned. Before the tunnel run, the recoil and nozzle reservoir pulses are simulated both to ensure that the laser and camera trigger at the same time and to acquire a laser scatter image. The Ludwig tube is then filled with fuel to its previously calculated initial pressure depending on the equivalence ratio desired for the experiment. The oscilloscopes used to record the pressure trace are armed. Immediately before the experiment, the laser energy is maximized by adjusting the doubling crystal to ensure sufficient

PLIF signal.

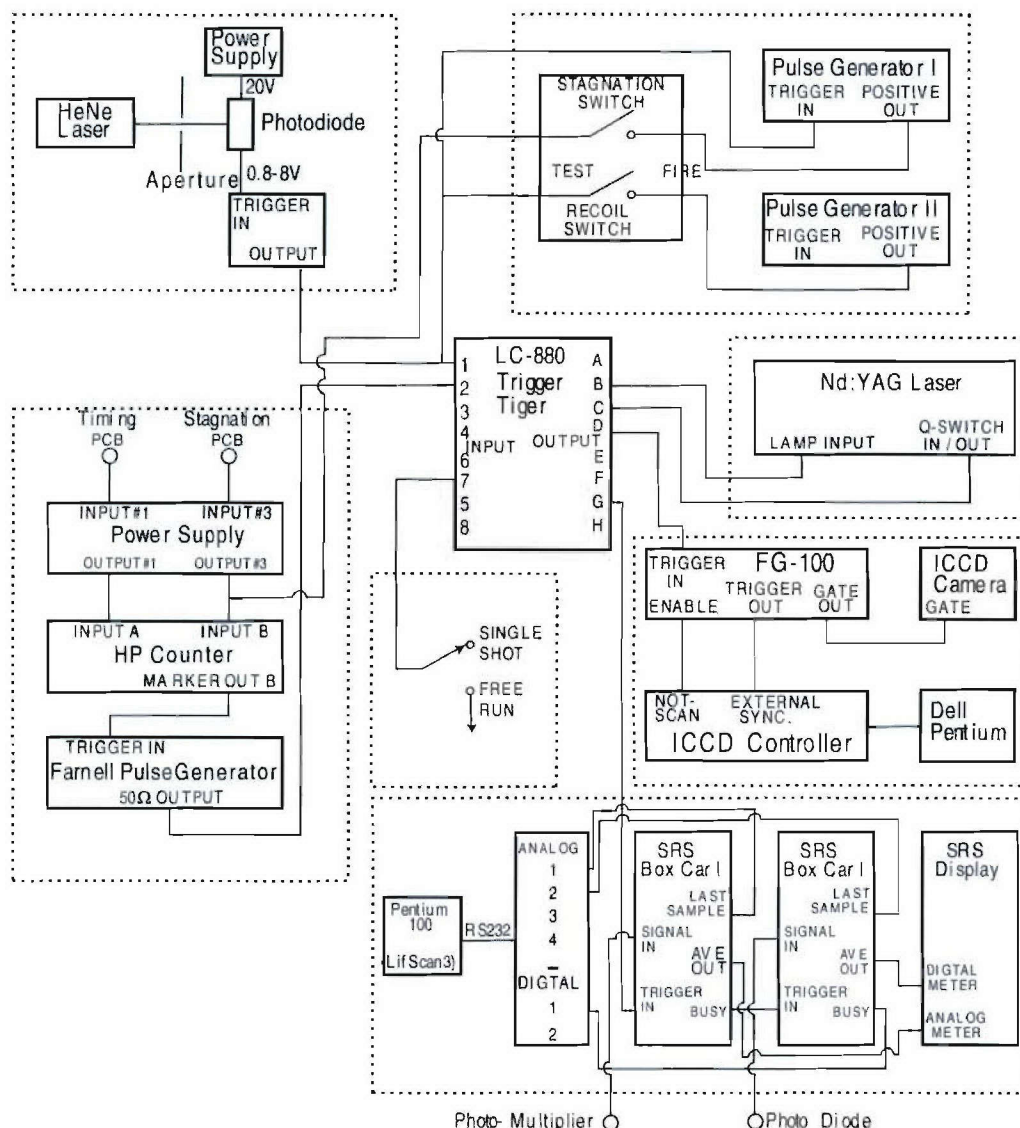


Figure 2.13: Trigger logic – timing electronics (from (Fox 2003)).

The tunnel is fired, causing it to recoil. The recoil of the tunnel is monitored by a sensor that initiates a logic control system (LabSmith LC880) that triggers the Nd:YAG laser, the camera and the oscilloscopes. The recoil also directly triggers the fuel injection system with a preset delay to introduce fuel into the scramjet at the correct pressure before the arrival of the test gas. The LC880 puts the electronic system into wait mode, and momentarily interrupts the laser from its 10 Hz pulse cycle to prevent premature triggering of the laser. When the shock wave reaches the nozzle reservoir, the stagnation pressure transducer re-triggers the laser, the oscilloscopes and the cameras after a preset delay. The laser pulse that excites the OH molecules has a duration of 10 ns, while the camera intensifier was gated for of 50 ns. This gate time was sufficient to capture all the OH fluorescence at these conditions without too much

contamination from chemiluminescence. The complete trigger logic for the PLIF experiments is outlined in Figure 2.13.

After the run, an additional laser scatter image and a camera dark noise image are obtained. The second scatter image is often closer to the experiment because of the deposit of soot on the duct during the nozzle start-up process, so these images were used in the image analysis process. It is also necessary to acquire a background image of the sheet profile camera. The background images acquired are used to account for the noise offset on the CCD sensor. The pressure histories are downloaded from the oscilloscopes and stored to hard disk.

2.5 Data Reduction

The processing of the pressure and PLIF data presented in this report was performed using MATLAB[®] scripts. This section describes the procedures followed to achieve the results presented in Chapter 5.

2.5.1 PLIF

The raw images the ICCD camera produces are an array of 576×384 16-bit values, corresponding to the fluorescence intensity measured by each pixel of the camera's CCD sensor. This raw PLIF data has to be corrected for:

1. the laser scatter and reflections of the scramjet top and bottom surface
2. the camera background and accumulated dark noise, about 500 counts out of 65535, which introduces a positive signal offset
3. the non-uniformity of the laser sheet, which usually leads to lower signal at the laser sheet edges and to higher values in the center
4. pulse-to-pulse variations in overall laser energy

Note that systematic errors in the PLIF signal caused by collisional broadening, collisional shift and Doppler shift were not accounted for. As described in Section 4.2.4, the transition was chosen to minimize the systematic error in signal due to changes in temperature.

Figure 2.14 shows false color images of (a) a typical raw PLIF image and (b) the corresponding scatter image plotted on a logarithmic scale to magnify signal variations. The PLIF

image on the left clearly shows where OH is present, but it also exhibits very high signal on the scramjet duct floor, especially on the cavity floor and to a lesser extent on the top of the duct where the fused silica window provides access for the laser. These high signal regions can also be identified on the scatter image on the right, indicating that the signal is not PLIF but is due to Rayleigh and Mie scattering from molecules and particles respectively. For the final images this is accounted for by subtracting the scatter image (b) from the actual PLIF image (a). In doing this, the (constant) camera background is also subtracted.

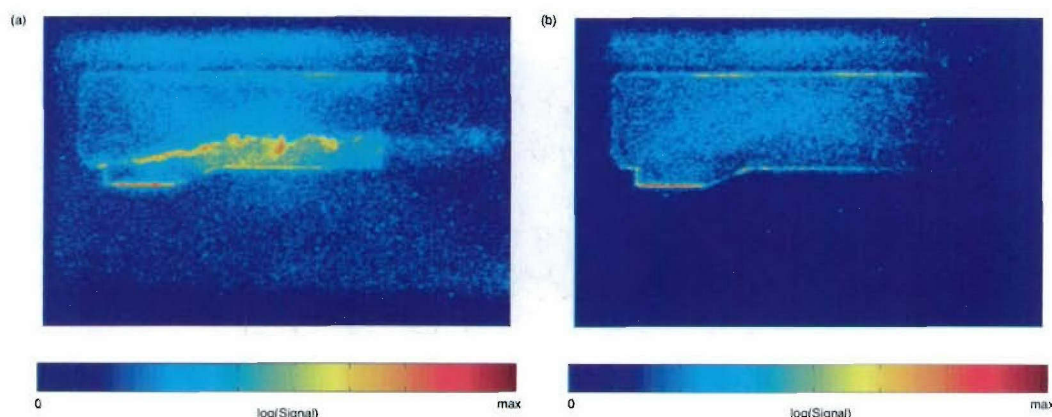


Figure 2.14: Raw false color images: (a) typical raw PLIF image, (b) corresponding scatter image, both plotted on a logarithmic scale to magnify signal variations.

Since the scatter on the PLIF image and on the scatter image are never exactly the same, further steps are necessary to get decent results. Subtracting pixels with high signal values from pixels with lower values artificially broadens the signal range of the image by introducing negative values. This is prevented by setting all negative pixels to zero. In turn, subtracting pixels with low or zero values from pixels with very high values, very high signal remains where virtually no OH exists, which can reduce the signal range in the region of interest significantly. This is accounted for by thresholding all "out-of-flow" pixels (i.e. scatter from surfaces) at the peak value of the "in-flow" field. The global laser sheet energy is measured for the pulse at which the PLIF image is acquired and for the one at which the scatter image is recorded. Therefore the scatter image is multiplied with the ratio of laser energies before subtracting it from the PLIF image.

Then the image is corrected for spatial laser energy distributions as described in detail in Section 4.2.3. The laser sheet's location is selected manually on both the PLIF image and the sheet profile image. The spatial energy distribution is determined (see Figure 4.5) and the PLIF image subsequently divided by the normalized energy trace. An extra correction factor needs to be included to account for the gain setting of the camera, as images for different runs were obtained at different gain settings to prevent saturation of the detector. Section 4.2.2 describes how the calibration factor for the camera gain variation was arrived at.

Having corrected for all the previously mentioned parameters, there still remains a certain amount of extra signal due to flow luminosity. This is particularly strong in regions where the flow is very hot, such as combustion areas, hot plumes and areas where oblique shock waves impinge. The luminosity varies significantly from one tunnel run to the next, thus making it impossible to subtract a single luminosity image from the PLIF images acquired at equal fuel conditions. The best option would be the use of a calibrated second camera measuring the luminosity for each tunnel run, but this resource was not available for these experiments. Therefore it was decided not to correct for luminosity but to present the PLIF image and the corresponding luminosity image side-by-side, giving a better impression of the flow field and the combustion process. The luminosity captured on the images is the complete luminosity integrated over the entire duct depth, in contrast to the PLIF images where only the excited plane produces a signal. Therefore the luminosity pictures are slightly blurred, because the camera has a depth of field of approximately 2 mm, compared with the 52-mm width of the combustor duct. Note that the luminosity images are only indicative because of the previously mentioned run-to-run variations, but they do give a good indication of the relative sizes of the fluorescence and luminosity signals for each condition. The PLIF data reduction process is schematically summarized in the flow chart in Figure 2.15.

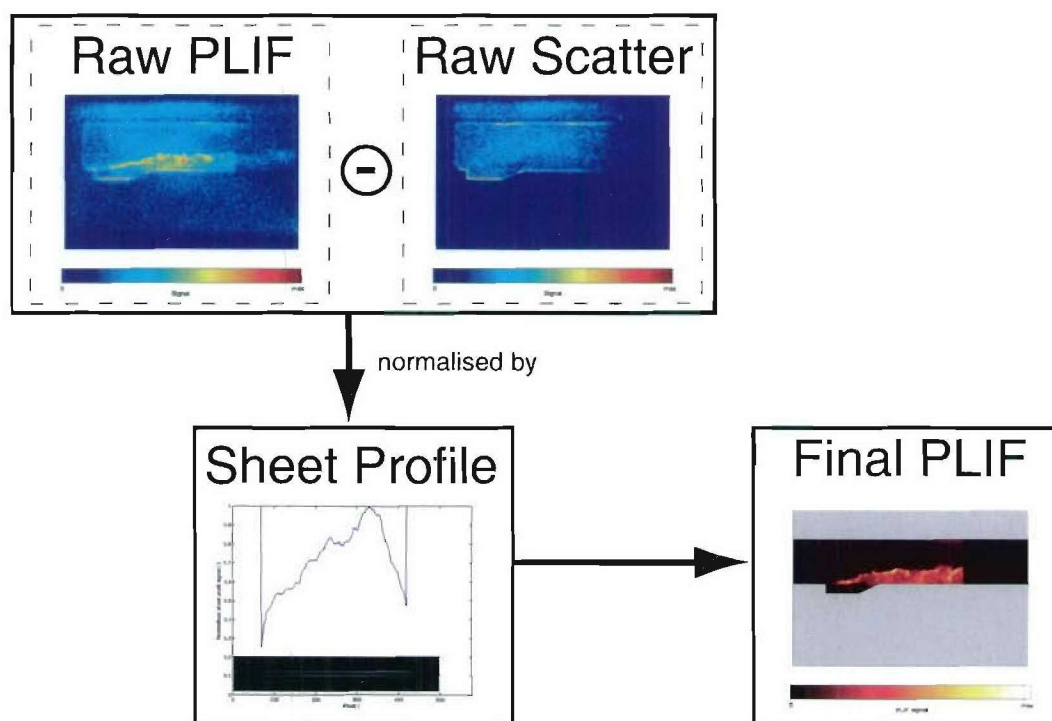


Figure 2.15: Flow chart of the PLIF data reduction process.

In addition to the actual images, graphs were produced, to allow for quantitative comparisons between images. The signal was averaged in the axial and transverse directions and plotted against the y-coordinate and the x-coordinate respectively, showing the axial development and the penetration height of the OH plume. The graphs presented are smoothed using a

running average over 5 data points, filtering noise but retaining information about large-scale flow structures. The plots are also normalized to their peak value. These results are presented in see Section 5.1. A distinct region downstream of the cavity trailing edge was chosen and the mean signal calculated, as an attempt to compare the relative amount of OH produced for different fuels and equivalence ratios. This region starts about 1 mm aft of the trailing edge and spans about 15 mm downstream with a height of approximately 8 mm as shown in Figure 2.16,

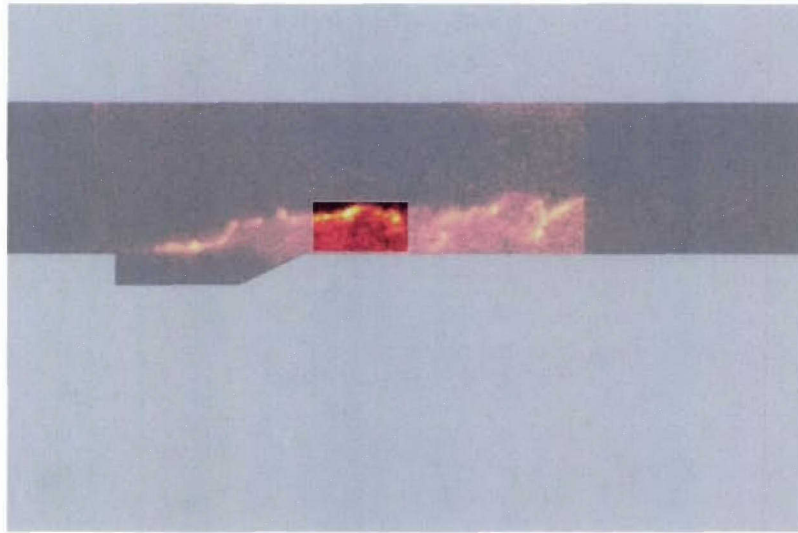


Figure 2.16: Region within the flow, selected to compare averaged OH signals for different equivalence ratios and fuels with each other.

2.5.2 Pressure Measurements

The pressure history within the scramjet is recorded using piezoelectric pressure transducers and stored using digital storage oscilloscopes. The locations of the transducers are specified in Section 2.2.1 and shown in Figure 2.5. To interpret the data, the pressure traces are shifted in time to account for the transit time through the nozzle. This is particularly important because the individual traces will be divided by the stagnation pressure to get normalized pressure traces. Following this the output voltage signals of the transducers have to be converted to pressure using the conversion factors given in Table 2.4. Since the pressure histories are recorded on oscilloscopes with different sample rates, the traces are all subsampled to the lowest sample rate, allowing us to divide the pressure traces sample-by-sample by the stagnation pressure. The recorded noise was filtered using a running average over $40\ \mu\text{s}$.

In order to visualize how the pressure develops throughout the duct, pressure versus distance graphs are produced from the pressure history traces. Having introduced a transducer-independent time scale, it is possible to instantaneously plot the pressure as a function of distance for each discrete time step by simply plotting the values for each transducer. To aid the in following the pressure distribution by eye, the measurement locations along the duct are connected by a cubic spline function, although this is not physically correct, since e.g. oblique shocks cause unsteady pressure changes. The spatial distribution of transducers along the duct floor is sparse, and the distribution is too under-sampled to capture all of the detail of how the spatial static pressure distribution changes with time. The time dependence of the scramjet flow field can be visualized best by generating time-resolved animations from each of the pressure traces. A MATLAB[®] script has written for that purpose.

Chapter 3

Initial Scramjet Experiments

This chapter details the initial experimental campaign of combustion tests. These tests consisted of static pressure measurements along the duct surface throughout the test time of the facility. These results were important in determining the overall performance of the combustor and in determining the best time at which to perform the OH PLIF measurements presented in Chapter 5. The facility and scramjet model used for these tests has been described in Chapter 2.

The initial experiments described here investigate the combustion of hydrogen and ethylene fuel in the scramjet duct incorporating a cavity flame-holder. The aim was to determine the degree of combustion achieved (if any) for a range of equivalence ratios. These experiments, performed over a range of equivalence ratios ($\Phi_{ethylene} = 0.13 - 0.64$, $\Phi_{hydrogen} = 0.24 - 0.47$) measured wall pressure histories in the region immediately downstream of the cavity. Once it was confirmed that combustion was occurring in all cases, subsequent experiments measured wall pressure histories along the full length of the scramjet duct (Fig. 2). In this initial test campaign, for each combination of equivalence ratio and fuel type, four sets of wall pressure data were obtained; fuel-off air, fuel-off nitrogen, fuel-into-air and fuel-into-nitrogen. The two fuel-off tunnel runs were only performed once, while the fuel-on runs were made for each equivalence ratio and fuel combination. Comparison of the fuel-into-air and the fuel-into-nitrogen tunnel runs provides the best indication of the extent of combustion occurring in the duct as indicated by the net pressure rise. The injection of the fuel will also influence the flow field in the duct and the axial pressure distribution, even in the absence of combustion, so comparison with the fuel-off data is used to quantify this.

3.1 Data Analysis

3.1.1 Pressure Comparisons

The stagnation pressure at the end of the shock tube, which supplies the nozzle, decreases with time as the test gas exhausts through the nozzle, as shown in Fig. 2.2. The pressure levels in the duct also nominally follow this trend as seen in the figure. Standard practice is to consider useful test flow to occur when the ratio of static pressure to nozzle supply pressure (i.e. the stagnation pressure) is approximately constant. This can be seen in Fig. 3.1, where normalized pressure histories are compared. This normalized pressure data is used in all further discussion as it removes any dependency on shot-to-shot variation.

The pressure histories in Fig. 3.1 illustrate the signal-to-noise ratio of the data and also give clues to the nature of the flow at each of the transducer positions. While the majority of the normalized pressure histories along the duct floor appear steady, it can be seen that for the combustion run shown, large static pressure perturbations occur at transducer 3 ($x = 272$ mm) and to a lesser extent at transducer 9 ($x = 392$ mm). Examination of the pressure magnitudes (Fig. 3.2) indicates that shock impingement occurs in the immediate vicinity of both of these transducers and therefore it can be concluded that the impingement point is not completely steady. The transducer ($x = 52$ mm) in the inlet roof and the transducer ($x = 170$ mm) in the cavity floor both exhibit significantly more noise than the downstream gages.

Finally the very slow rise time of the signal from transducer 1 ($x = 232$ mm) is also noted and the data at this point was therefore questionable. This gage is located immediately downstream of the cavity and would be well within any expansion fan centered on the rear cavity lip. Subsequent experiments in the latter PLIF campaign described in Chapter 5 incorporated improved thermal shielding on this pressure transducer, revealing that it was in fact inaccurately reading low in the first experimental campaign.

Figures 3.2–3.5 compare the wall pressure distributions for fuel-into-air and fuel-into-nitrogen runs for a number of different combinations of fuel and equivalence ratio. Some general trends are apparent from these data plots. In all cases there is a significant increase in the static pressure in the cavity over that measured upstream in the inlet. It is noted that this is true even in the absence of combustion as seen from the fuel-into-nitrogen data. This would indicate that this pressure rise is predominantly a product of the injection of additional mass into the cavity and its effect on the local flow field and is not simply a product of combustion.

This conclusion is confirmed by the fuel-off data for both air and nitrogen test gases as shown in Fig. 3.7 to Fig. 3.10. That said, when the fuel is injected into a flow of air rather than nitrogen, an additional pressure rise is observed for both fuels for all equivalence ratios tested, indicating the presence of combustion in the duct. It is noted that unlike previous work that used

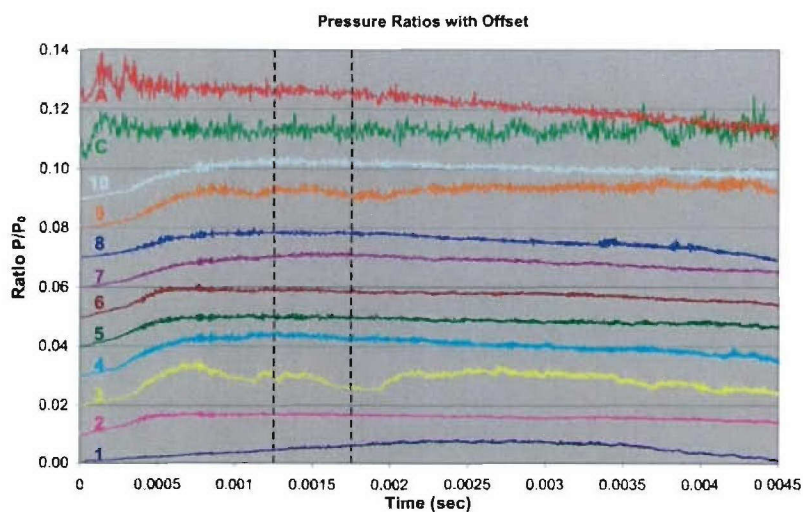


Figure 3.1: Normalized wall pressure histories for hydrogen injection into air test gas ($\Phi = 0.24$) with nominal test time indicated. (Note that the levels for each indicated transducer are offset for clarity)

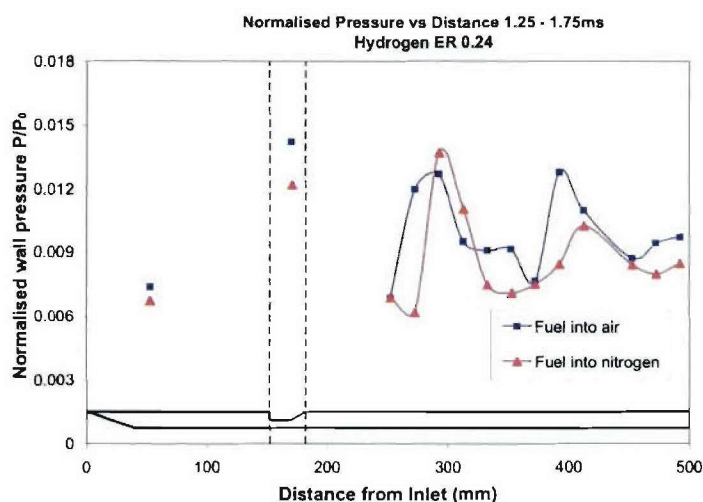


Figure 3.2: Normalized floor pressure distribution ($\Phi = 0.24$, hydrogen fuel)

artificial means such as spark plugs (Mathur et al. 2001) or hydrogen flames (Taha et al. 2002) to initiate combustion, no such means were used in these experiments. The observed combustion is the product of auto-ignition. In the cavity we could expect a subsonic recirculation. The high

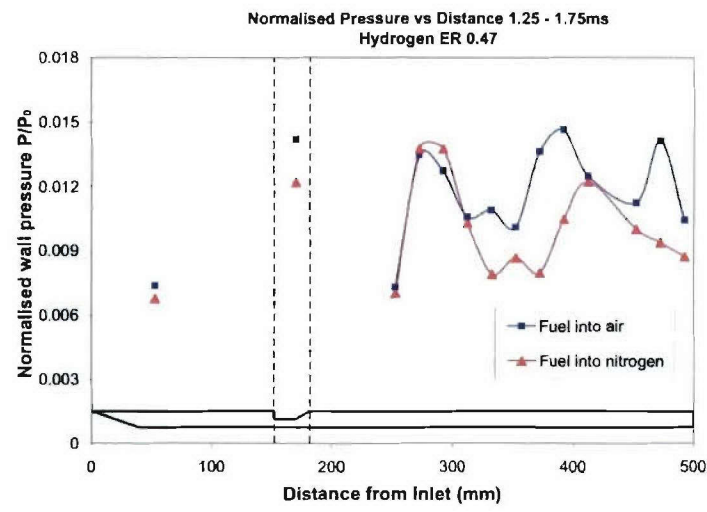


Figure 3.3: Normalized floor pressure distribution ($\Phi = 0.47$, hydrogen fuel)

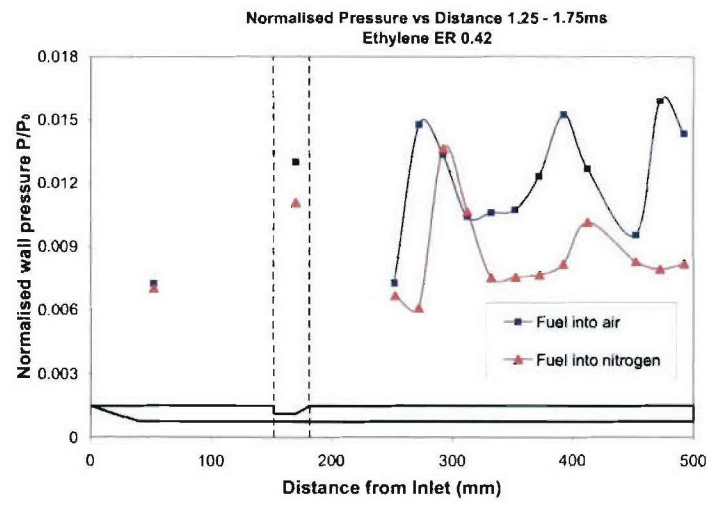


Figure 3.4: Normalized floor pressure distribution ($\Phi = 0.42$, ethylene fuel)

static temperature of the free stream flow in the duct is increased further as the high stagnation temperature of the free stream flow is partially recovered in the shear layer across the cavity opening. This hot flow will mix with the cold fuel that is injected into the cavity and raise its temperature significantly. For the Mach 11.5 flight condition simulated it is possible that there

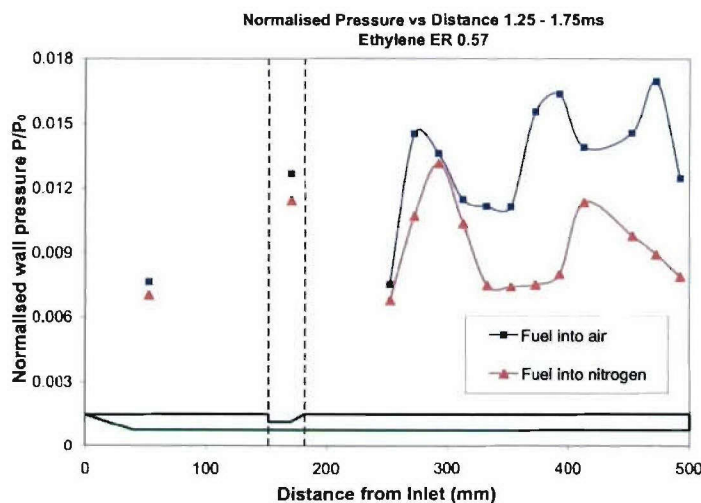


Figure 3.5: Normalized floor pressure distribution ($\Phi = 0.57$, ethylene fuel)

are regions in or above the cavity where the fuel-air mixture will be at sufficient temperature for ignition.

Static pressure distributions are presented here as a ratio to the nozzle reservoir pressure during the test time. The absolute value of the inlet pressure is between 120 and 130 kPa during the test time. This is some 20–30 percent higher than the free stream pressure predicted in STUBE and presented in Table 2.3. The most likely reason for this higher pressure is the finite diameter ($190 \pm 20 \mu\text{m}$) of the duct leading edge. Initially there was some concern that the normal shock forming at the front of the scramjet may have caused spillage of hot, high-temperature and high-pressure gas into the inlet. A luminosity photograph of the inlet to the scramjet duct, presented in Fig. 3.6 and obtained during the nominal test time, shows that the hot gas from the bow shock (the bright yellow part of the flow field) around the front of the scramjet model is not ingested into the duct at these flow conditions.

Immediately downstream of the cavity ($x = 232 \text{ mm}$) the wall static pressure falls, suggesting that combustion has been extinguished. It is noted that there is nominally no difference in the pressure levels for fuel-on runs in both air and nitrogen test gases at this location. A sharp pressure decrease could be expected to occur in the presence of a strong expansion centered on the downstream lip of the cavity.

Further downstream the pressure at the floor rises sharply again indicating the impingement of a shock wave, most likely induced by the presence of the cavity and reflected back from the roof of the duct. This is observed for both the air and nitrogen test cases. For the remaining

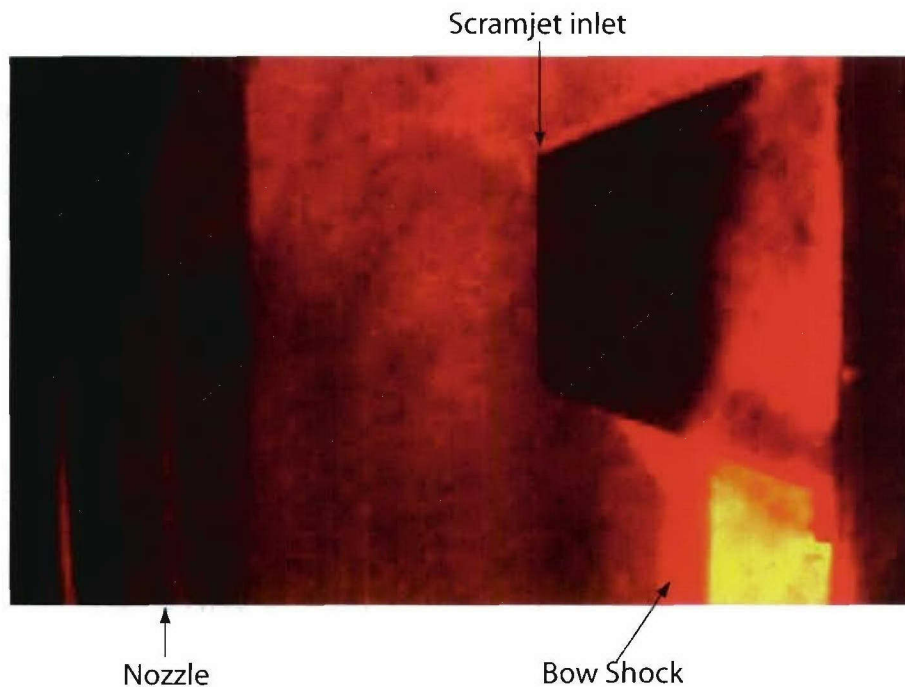


Figure 3.6: Luminosity image of the scramjet inlet

length of the instrumented duct, this progression of peaks and troughs is observed in some form for all experimental cases indicating the presence of an oblique shock train induced by the cavity and the injection process. The pressure distributions for the fuel-off cases also exhibit this behavior confirming that an oblique shock train is induced by the geometry of the cavity even without fuel injection (Fig. 3.7 and Fig. 3.9) as would be expected for the impingement of the shear layer on the floor or rear wall of the cavity.

The oblique shock train is observed to move axially in the duct under different flow conditions. There is no significant difference between the pressure distributions for the two fuel-off cases (Fig. 3.7 to Fig. 3.10). When fuel is injected into the nitrogen flow the floor pressure distributions show that the impinging shock behind the cavity moves upstream (Fig. 3.8 and Fig. 3.10). The shock train moves further upstream when fuel is injected into air and combustion occurs (Fig. 3.2 to Fig. 3.5).

The net pressure rise observed for the fuel-into-air case over the fuel-into-nitrogen case is a measure of the pressure rise due to combustion. Such pressure rises are observed to occur for all fuel-into-air runs and this is clearly indicated in Fig. 3.2 to Fig. 3.5. The pressure data indicate that the main area of combustion (at least in the region along the floor centerline) begins downstream of the cavity after the point at which the oblique shock train first impinges on the duct floor after reflection from the roof. As stated, the combustion that occurs in the cavity appears to be locally extinguished by an expansion downstream of the cavity, but the impingement of the shock further downstream appears to reignite the flame.

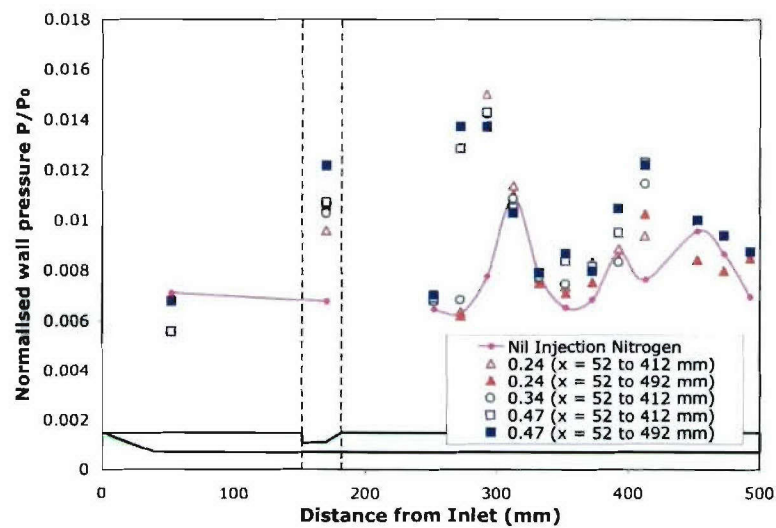


Figure 3.7: Normalized floor pressure distribution for injection of hydrogen into nitrogen at various equivalence ratios.

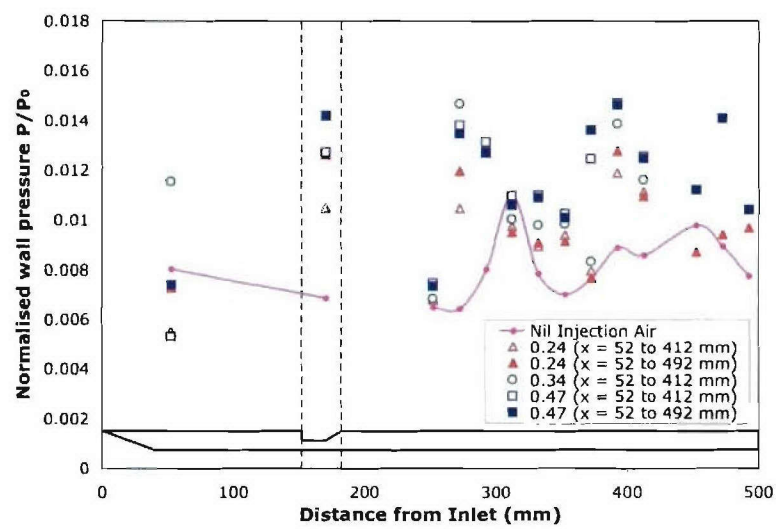


Figure 3.8: Normalized floor pressure distribution for injection of hydrogen into air at various equivalence ratios.

It is suggested that the apparent initial pressure rise observed in this region ($x = 232\text{--}292\text{ mm}$) for the fuel-into-air runs is more a product of the upstream movement of the oblique shock train rather than a combustion rise. When combustion occurs in or above the cavity, the

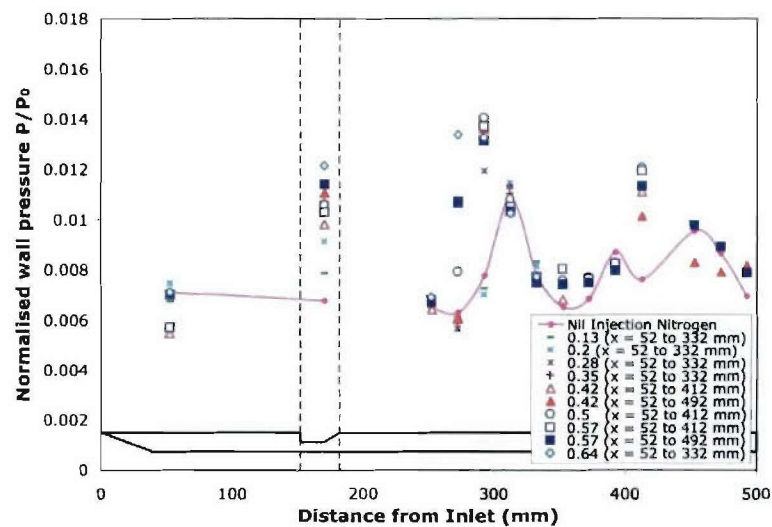


Figure 3.9: Normalized floor pressure distribution for injection of ethylene into nitrogen at various equivalence ratios.

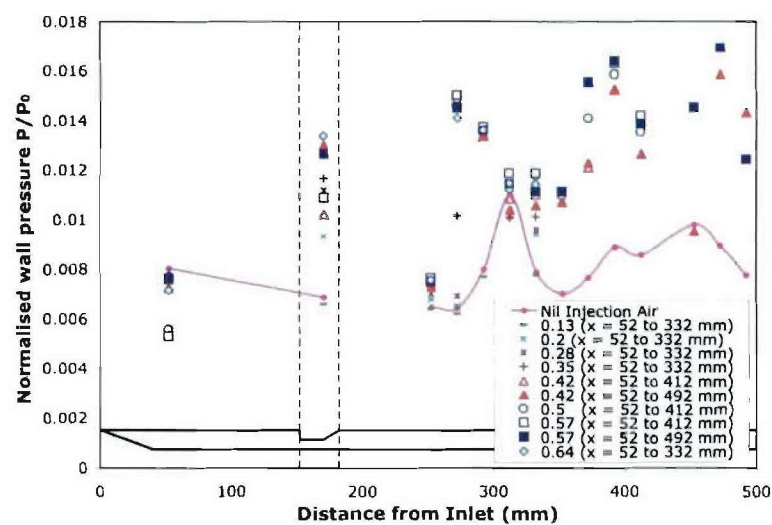


Figure 3.10: Normalized floor pressure distribution for injection of ethylene into air at various equivalence ratios.

shock origin and angle are influenced, moving the shock reflection upstream.

3.1.2 Equivalence Ratio Effects

The pressure data can be used to determine the variation of the degree of combustion with increasing equivalence ratio. Fig. 3.7 to Fig. 3.10 directly compare the axial pressure distributions for a range of equivalence ratios for both fuels. The graphs collect data for fuel-into-nitrogen and fuel-into-air runs separately for each fuel. In each case the pressures observed for the range of equivalence ratios are compared with the corresponding fuel-off case.

Examination of the hydrogen-into-nitrogen and the ethylene-into-nitrogen data sets shows a large increase in the duct floor pressure when mass is injected into the cavity. It is noted once again that these measurements were made 10 mm off the centerline in the cavity floor, 17.5 mm downstream of the step. This pressure increases with equivalence ratio, as we would expect. Fig. 3.11 plots this dependence of cavity floor pressure on equivalence ratio. Again it can be seen that a further increase in pressure due to combustion is observed for injection into air. Interestingly, whereas we may expect a higher pressure increase for ethylene injection than for hydrogen injection at a given equivalence ratio, the opposite is observed.

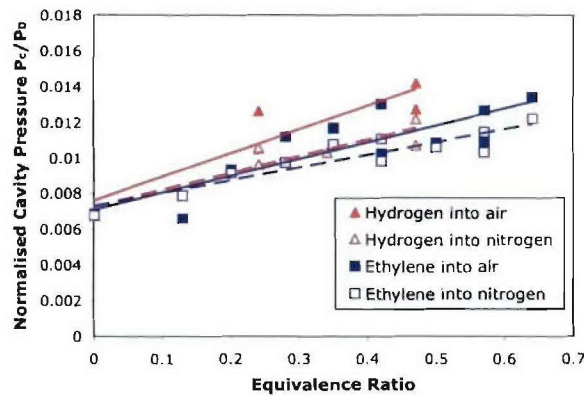


Figure 3.11: Dependence of cavity floor pressure on equivalence ratio.

To more clearly quantify the dependence of the combustion process on the equivalence ratio, the integrated net pressure rise for each combustion case was calculated starting from a displacement of 312 mm from the duct inlet and continuing downstream to the last data point. This starting position was chosen as it was considered, in all cases, to be the closest point to the re-ignition of the flame. It also avoided including the data immediately upstream, which was heavily influenced by any movement of the oblique shock train and therefore was potentially

misleading.

These integrated pressure rises are plotted against equivalence ratio in Fig. 3.12. Best-fit lines are shown for each of the longer data sets, one for each fuel. These lines were constrained to pass through the origin as could be physically expected. It is noted though that a comparison of the fuel-off runs for both air and nitrogen (representing $\Phi = 0$) yields a non-zero value. This is indicative of the level of accuracy of this method of manipulating the data, which is very sensitive to any movement of the oblique shock train.

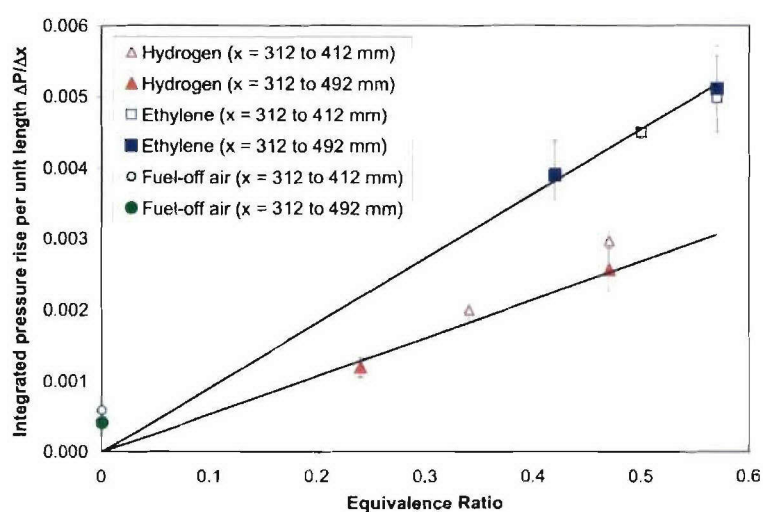


Figure 3.12: Normalized pressure difference per unit length vs equivalence ratio for the injection of hydrogen and ethylene fuel. Best-fit lines are shown for each of the longer data sets.

The trends shown in Fig. 3.12 are strongly linear, showing that a greater integrated pressure rise due to combustion is observed for increasing equivalence ratio as expected. What is not expected is the comparative levels of this trend for the two fuels. This is discussed in detail in the next section.

3.2 Discussion of Static Pressure Results

3.2.1 Combustor Flow Field

The presence of the cavity and the injection of fuel both contribute to the formation of oblique shock waves in the scramjet duct. This structure is caused by the presence of the

cavity, since a constant area duct with sharp leading edges and no cavity would have only weak wave structure caused by boundary layer growth and finite radius leading edges. The exact distribution of this shock structure varies with particular conditions. For the fuel-off cases, the incoming flow enters the combustor section with the given inlet conditions. The shear layer created as the air flows over the cavity no longer remains parallel with the floor, but directs downwards in such a way that it impinges somewhere on the rear ramp angle (Fig. 3.13). A shock wave develops at this point, reflects off the ceiling of the duct, then off the floor, and so on. This process of reflecting off the walls occurs continuously along the duct, and hence the strong spatial fluctuations observed in the axial floor pressure distributions.

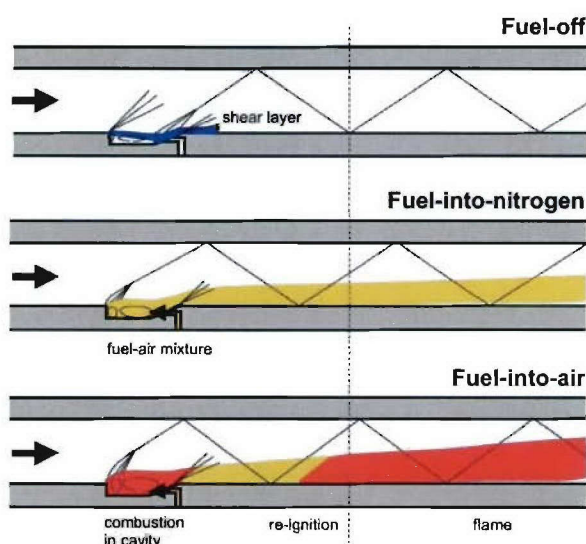


Figure 3.13: Sketches of possible combustion chamber flow field structures for the three flow cases.

For fuel injection shots, the floor pressure distributions indicate the movement of the shock system further upstream than for the nil-injection cases. This occurs because the cavity is the fuel source. The fuel must leave the cavity (by conservation of mass) and thus an obstruction is formed that directly affects the oncoming flow. The incoming flow interacts with this obstruction, and provides mixing between the fuel and the air. A shock wave will form at the obstruction, and reflect obliquely off the walls as it travels downstream. Unfortunately, the limited spatial resolution of the pressure measurements prevented more precise conclusions about the shock structure, particularly in the vicinity of the cavity. The PLIF and flow luminosity visualizations obtained in the second series of experiments (Section 5.1) reveal more detail of the flow structure in the duct, as do the initial CFD simulations reported in Section 5.2.

3.2.2 Combustion Pressure Rise and Ignition Length

Whilst there appears to be a pressure rise in the cavity due to combustion, it is believed that this initial region of combustion may be local to the cavity. The data indicates that the pressure for this region of combustion increases with increasing equivalence ratio. Downstream of the cavity the rapid decrease in the floor centerline pressure appears to indicate that the cavity flame is extinguished. The pressure data then suggests that the flame re-ignites after the fuel-air mixture is compressed and heated by the oblique shock reflecting downstream from the cavity. The point at which the pressure begins to increase due to heat release appears to be approximately the same for both fuels, for all equivalence ratios. An accurate value cannot be given, due to the finite spacings between transducers, however combustion does occur in this region at approximately 100 mm downstream of the cavity. This downstream distance is a function of the shock impingement rather than an indication of ignition length.

The true ignition length is not only a function of the fuel itself, but of the conditions in the duct. The recirculation region in the cavity causes the local temperature to be quite high, because the local velocities are low and the kinetic energy of the main stream has been converted to thermal energy. The temperature is reduced when the cold flow is injected, but good air/fuel mixing can occur. The most likely location for initial combustion reactions to occur is just above the cavity at the main air/fuel interface where temperatures have not been reduced as much as in the cavity and the local equivalence ratio is favorable. The resolution of the pressure data in these initial experiments was not sufficient to resolve ignition lengths in the shear layer above the cavity. The PLIF experiments reported in Section 5.1 provide sufficient spatial resolution in this region to allow calculation of the ignition lengths for the range of equivalence ratios tested.

However since the main combustion pressure rise, observed downstream of the cavity, occurs at approximately the same location, it is reasonable to conclude that the cavity is not only helping the mixing but may also allowing the combustion reactions to proceed to the extent of providing a continual supply of radicals to the main flow. Re-ignition is then able to occur via shock-induced compression and heating immediately downstream of the strong shock reflection that occurs downstream of the cavity. Between the cavity and that shock reflection, temperatures are significantly lower due to the expansion from the trailing lip of the cavity, as indicated by the observed pressure drop, and the combustion reactions may well be extinguished there. The radicals would remain chemically frozen until they reach the region of higher temperature at the shock reflection, and so it is here that combustion occurs. This process of extinguishing and re-ignition may repeat down the duct as the reflecting expansion and shock propagate downstream.

As all of the fuel-into-air runs sustain combustion right to the end of the instrumented duct, no conclusions can be drawn about the effect of the cavity on flame length.

3.2.3 Equivalence Ratio Effects

The experimentally observed pressure rise is a result of the combustion process and thus the integrated pressure rise should be a measure of the energy released in that combustion process. The stoichiometric overall combustion reactions for both hydrogen and ethylene fuels are described by Equation 2.13. Six times as many moles of hydrogen are required for stoichiometric combustion than are required for the stoichiometric combustion of ethylene. When we account for the molecular weights of the two fuels, approximately 2.33 as much mass of ethylene is required as compared to hydrogen for stoichiometric combustion. We must also consider the energy densities of the fuel. The lower heating value of hydrogen is 119554 kJ/kg while the lower heating value of ethylene is 47185 kJ/kg (Turns 1996). Thus every kilogram of hydrogen burnt will release 2.53 times as much heat as a kilogram of ethylene. When we combine these two effects, we could expect that fuel/air mixtures of the same equivalence ratio will release approximately the same energy and therefore produce approximately the same pressure rise in the duct. Instead, ethylene was observed to exhibit a consistently higher integrated pressure rise than hydrogen for a given equivalence ratio.

The simple analysis above assumes perfect mixing and complete combustion for both fuels, neither of which are likely to occur in the scramjet combustor. It also does not take into account differences in the rates of turbulent and diffusive mixing, which for turbulent mixing in the current experiments may be greater for ethylene or the likely differences in the penetration of the fuel jets into the air stream. Further, more detailed measurements and simulations are required to understand the relative combustion levels observed. It is important to note that the greater pressure yield from ethylene that was observed here has also been observed in recent non-cavity ethylene-fueled experiments in the T4 shock tunnel at the University of Queensland (Paull 2003).

3.2.4 Summary

In the initial experimental campaign, detailed wall pressure measurements were performed at a simulated flight Mach number of 11.5 in a constant area scramjet duct incorporating a single cavity flameholder. Hydrogen and ethylene were independently injected upstream into the cavity at a range of equivalence ratios. These are the first measurements reported in the open literature investigating the performance of a cavity flameholder in which combustion was induced and sustained at high Mach numbers without external means. The geometry of the cavity generates a train of oblique shocks that extend downstream in the duct. This oblique shock train moves upstream when mass is injected into the cavity and further upstream again when combustion occurs.

The wall pressure measurements indicate that for the duct flow conditions tested, com-

bustion was initiated and maintained for an appreciable length of duct in all fuel-into-air runs. Combustion was observed in the cavity, was seen to be extinguished immediately downstream, possibly by an expansion and then re-ignited by the impingement of an oblique shock reflecting downstream from the cavity. This process of extinguishing and re-ignition is apparent along the floor centerline of the duct as the structure of alternating shock waves and expansions reflects downstream. Ignition lengths could not be resolved within the spatial resolution of the pressure instrumentation. This cavity geometry was concluded to contribute to the mixing, ignition and combustion of the fuel in the scramjet combustor duct for the flight Mach 11.6 flow condition investigated.

As anticipated, increasing the equivalence ratio increased the net pressure rise due to combustion. Interestingly though this pressure rise was observed to be higher for ethylene than for hydrogen at comparable equivalence ratios. It is hard to conclude the mechanism for this without further data detailing the flow field and the combustion processes in the duct.

Chapter 4

Preliminary PLIF Experiments and CFD Methodology

This chapter is split into two main parts. It begins with a brief introduction to the relevant aspects of fluorescence spectroscopy for the main experiments in the report, presented in Chapter 5. A series of preliminary experiments that assisted in the choice of transition and excitation energy to produce linear fluorescence at the conditions experienced in the scramjet combustor is presented.

The remainder of the chapter describes the computational aspects of the investigation, beginning with a general outline of the numerical schemes used and then describing how the CFD++[®] code was used to investigate the mixing and combustion processes investigated in the experiments.

4.1 Theoretical Aspects of Laser-Induced Fluorescence

4.1.1 Laser-Induced Fluorescence (LIF)

Laser-induced fluorescence (LIF) is a process in which molecules or atoms are excited to higher electronic energy states via laser absorption, and subsequently fluoresce. The intensity of the fluorescence is a function of the species concentration (or number density), the gas temperature, pressure and velocity. For low levels of irradiance, the fluorescence is linearly dependent on the absorber number density. As a result of the fact that the energy states of molecules and atoms are quantized, the spectral absorption regions are discrete. For large molecules, however, the spacing of the discrete transitions can become sufficiently small and the number of transitions sufficiently great, that discrete absorption regions blur to continuous absorption bands. Fluor-

rescence is incoherent and isotropic, and due to the dephasing effect of collisions it is largely unpolarized.

LIF can be used for both qualitative and quantitative flow field investigations. Initially it was used to determine number densities and temperatures (by considering the dependence of the ground population on temperature) in flames and other high-temperature flows, but it is also used for measurements of velocities (by measuring the Doppler shift of the transition) and pressures (by observing pressure-dependent transition broadening). Quantitative measurements are difficult to achieve for LIF of radical species, as calibration with a known radical concentration must be performed, and this can be difficult to generalize to the flow field of interest.

The excitation of atoms or molecules is usually achieved using pulsed lasers, such as Q-switched Nd:YAG-pumped dye lasers or excimer lasers. For most experiments, these lasers have sufficiently short pulse durations (typically of the order of 5–30 ns) to obtain a “frozen” image of the flow field, even for supersonic or hypersonic flow.

Laser-induced fluorescence has the threefold advantages for combustion studies of being non-intrusive, species-specific and highly sensitive, being able to detect radical or trace species at ppm and sub-ppm levels. Radical species such as OH, CH or NH usually reside in the concentration range of 100 ppm (0.01%), which cannot easily be detected using other nonintrusive diagnostic techniques such as Raman-scattering. LIF transitions can be excited for a variety of species of interest in combustion research: more than thirty combustion intermediates can be detected.

A drawback of LIF is its complex dependence on number density, temperature, non-radiative quenching, pressure (line broadening and shifting) and Doppler shift (velocity). Quenching dependence is a particular problem in combustion studies because the quench rates vary with pressure, temperature, composition and in the case of OH, the excited rotational quantum number. When analyzing fluorescence measurements these effects must be accounted for if quantitative interpretations are required. Line broadening and Doppler shift have only minor effects if the corresponding parameters are held within a reasonable variation range, whereas the influence of temperature is not negligible and therefore makes it difficult to interpret raw LIF measurements on a quantitative level if the temperature is unknown and/or the modeling of electronic quenching is not sufficiently accurate.

4.1.2 Planar Laser-Induced Fluorescence (PLIF)

As mentioned in Section 4.1.1, laser induced-fluorescence can be extended to two spatial dimensions by expanding the laser beam into a thin sheet, typically using a set of cylindrical and spherical lenses. The technique is then referred to as planar laser-induced fluorescence (PLIF).

If the laser wavelength is resonant with a transition of a species present in the flow (in the case of these experiments, the hydroxyl radical), the incident light will be partially absorbed at each point within the illumination plane, and a fraction of the absorbed photons may subsequently be re-emitted as fluorescence at a different wavelength. The excitation wavelength for fluorescence is different depending on the molecular species of interest.

For two-dimensional measurements such as those presented in this report, the emitted fluorescence is usually recorded with a CCD (charge-coupled device) camera. Intensified CCD cameras are used if temporal filtering of the fluorescence signal is required. This can be particularly useful for highly luminous environments like the one investigated in this report. The signal strength detected by the camera depends on the concentration of the species of interest within the corresponding observed volume and again on the local flow field conditions such as temperature, pressure and gas composition. To discriminate the fluorescence from laser scatter, luminosity and other negative effects, wavelength filtering in the form of interference filters or colored glass absorption filters is required.

The OH radical is often used as a detection species for fluorescence-based flame studies. The fluorescence signal is relatively strong, making it easy to detect. Near the ignition point, the OH radical is a good indicator of flame front location, while further downstream it becomes a quasi-stable component of the combustion products, and can be used to determine the extent of combustion. We restrict ourselves in this report to investigation of the flow in and near the cavity.

For a more general and detailed discussion of LIF, the reader is referred to the books by Demtröder (1996) and Eckbreth (1996) and the review paper by Seitzman and Hanson (1993b).

4.1.3 The Two-Level Model

As an idealization, laser-induced fluorescence can be described as a two-step process; excitation from one rovibronic (rotational-vibrational-electronic) state to another followed by the subsequent emission of radiation (or fluorescence). As the species investigated are usually molecules rather than atoms, the electronic levels are split into sub-levels according to the molecular electronic, vibrational and rotational energy. These levels are normally referred to as rovibronic levels. The vibrational levels are numbered with $v = n$, ($n = 0, 1, \dots$), rotational levels numbered with $J = m$, ($m = 1.5, 2.5, \dots$). Double primes are used to mark the state vibrational (v'') and rotational (J'') levels of the ground electronic state, while single primes mark the excited state levels (v') and (J'). Figure 4.1 is a simplified representation of the laser-induced fluorescence process between the $X^2\Pi$ ground electronic state and the $A^2\Sigma^+$ excited electronic state of OH. A thorough description of the symbols used to specify the different electronic states can be found in (Demtröder 1996) and (Eckbreth 1996). When using PLIF, any of the processes

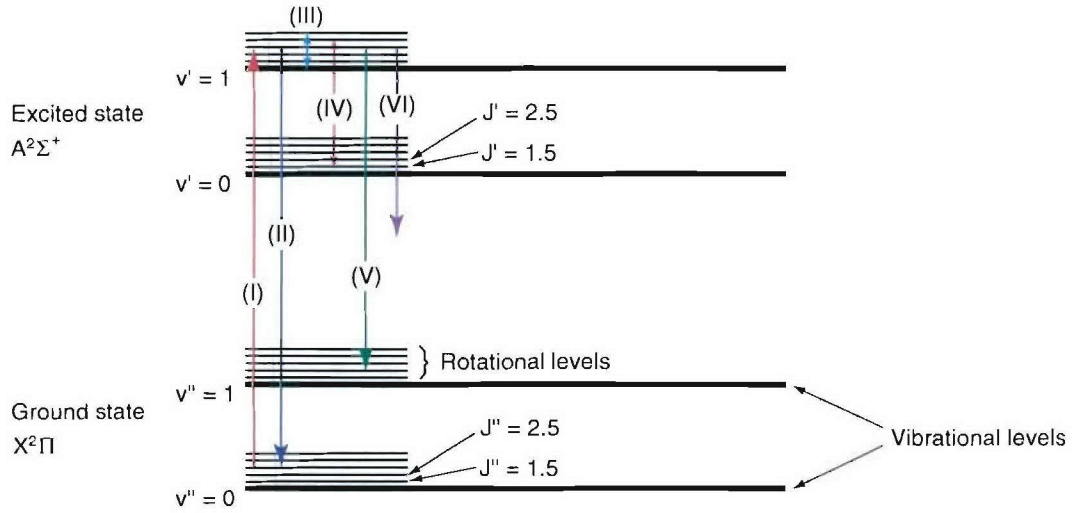


Figure 4.1: Schematic of LIF excitation between two rovibronic states of OH and subsequent relaxation

labeled in Figure 4.1 may occur (Eckbreth 1996):

- **Excitation of a transition (I)** from the ground state to an excited state by tuning the laser to a specific wavelength with a rate constant of W_{12} .
- **Stimulated emission back to the ground state (II)** which does not provide any PLIF signal. It has a rate constant of W_{21} .
- **rotational energy transfer (RET) (III)** to neighboring rotational levels.
- **vibrational energy transfer (VET) (IV)** to neighboring vibrational levels.
- **Spontaneous emission/fluorescence (V)** at a rate A_{21} determined by the Einstein A coefficient.
- **Collisional quenching (VI)**, de-excitation to the ground electronic state by collisions with other atoms or molecules. As these de-excitations do not produce photons, quenching decreases both the amplitude and the lifetime of the fluorescence signal. Its rate constant is given here by Q_{21} .

Without derivation, the fluorescence signal S_f imaged on the camera is given by

$$S_f = N_T f_B B_{12} E g \Phi \frac{\Omega}{4\pi} d\eta \quad (4.1)$$

where E is the laser energy, $\Omega/(4\pi)$ the solid camera angle and η the camera efficiency (with $\eta \leq 1$). B_{12} is the Einstein coefficient for stimulated emission, d is the depth of the illuminated gas volume with the cross-sectional laser sheet area A , the laser sheet thickness and g is the unity-normalized spectral overlap integral, which describes the amount of overlap between the laser and molecular transition profiles. N_T is the total species population and f_B is the fraction of those molecules in the lower rovibronic state excited by the laser, also known as the Boltzmann fraction. The factor Φ which is defined as $\Phi = A_{21}/(A_{21} + Q_{21})$, is known as the fluorescence efficiency or fluorescence yield. Equation 4.1 shows that, in the linear regime, the detected LIF signal (S_f) is independent of the cross-sectional area of the laser sheet A and the duration of the laser pulse.

The two-level model is a good description of the fluorescence process provided the laser intensity is not great enough to perturb the Boltzmann distribution of molecules in the population, and loss mechanisms such as vibrational/rotational energy transfer and predissociation are negligible. If the irradiance becomes too great, the transition saturates and the behavior of the fluorescence is no longer described by Equation 4.1. In this case, more sophisticated multi-level models, like the four-level model used by Berg and Shackelford (1979), become necessary for a full description of the fluorescence process. The LIFBASE code (Luque and Crosley 1999) was used for all the modeling used to choose appropriate transitions, and is discussed in Chapter 4.

There are several possible mechanisms by which fluorescence can be excited in the OH molecule (Seitzman and Hanson 1993a). The most commonly used of these involves exciting transitions in the $A^2\Sigma^+ \leftarrow X^2\Pi(1,0)$ band at 283–285 nm. This excitation scheme has been chosen for the current experiments for three reasons. Firstly, the signal is strong because this scheme excites transitions from the lower vibrational level of the ground $X^2\Pi$ electronic state. Second, the excitation wavelengths for the $A^2\Sigma^+ \leftarrow X^2\Pi(1,0)$ band of OH do not coincide with excitation spectra of other species, and so measurements are not susceptible to contamination from other sources of fluorescence. This is particularly desirable for hydrocarbon combustion, where several other fluorescing species can occur as intermediate species in combustion reactions. Finally, this excitation scheme mostly generates fluorescence from radiative transitions in the (1,1) band near 315 nm and the collisionally populated (0,0) band near 308 nm. As the fluorescence is spectrally well isolated from the excitation wavelengths, stimulated emission and laser scatter at the excitation wavelength can be effectively removed by spectral filtering of the fluorescence signal.

4.2 Preliminary PLIF Calibration Experiments

4.2.1 Saturation Irradiance Measurements

As mentioned above, saturated fluorescence occurs when the laser irradiance is sufficient to significantly depopulate the ground rovibrational state. Additional laser energy cannot excite as many molecules, so the fluorescence is no longer proportional to the laser irradiance. In practice this occurs either when a transition is excited with high irradiance or when the gas pressure is low. The saturation intensity varies between transitions and with different flow conditions. The equation for fluorescence signal, Equation 4.1, can be generalized to account for saturation. It becomes then (Palma 1998)

$$S_f = N_T f_B B_{12} E g \Phi \frac{\Omega}{4\pi} d\eta_c \left(1 + \frac{I}{I_{sat}}\right)^{-1} \quad (4.2)$$

where I is the laser irradiance, I_{sat} the saturated laser irradiance and η_c the collection efficiency of the PLIF system. The dependence of saturation on the transition, the laser and the state of the gas is given by (Palma 1998)

$$I_{sat} \propto \frac{p}{B_{12} g \sqrt{T}} \quad (4.3)$$

Saturation is a source of systematic error in PLIF measurements. The degree of saturation depends upon laser irradiance, transition line strength, and the pressure and temperature of the gas. A thorough investigation of the degree of saturation in the scramjet combustor would require a large number of runs at different excitation irradiances. Even in the case where such measurements could be readily made, the turbulent nature of the flow field would require a large number of measurements to achieve a good averaged signal. Rather than attempting this, the PLIF signal of a hydrogen/oxygen torch flame at atmospheric pressure, which depends on the irradiance, was measured for fuel-rich through fuel-lean mixtures.

The pressure (≈ 100 kPa) and the temperature (≈ 1800 K) of the torch flame are similar to those expected in the scramjet combustor ($p \approx 80 - 300$ kPa and $T \approx 1100 - 2800$ K). Equation 4.3 indicates that the saturation irradiance for a given transition is proportional to pressure and inversely proportional to the square root of temperature. In the worst case ($T = 3000$ K and $p = 80$ kPa), the saturation irradiance would be 64% of the torch value. Thus, keeping the irradiance below 50% of the measured saturation irradiance should ensure that the fluorescence measurements in the tunnel runs are not saturated.

To measure the saturation irradiance, the relationship between irradiance and laser energy must be calibrated. This also includes measuring the thickness of the laser sheet. For this measurement, neutral density filters were placed in front of a photodiode placed downstream of the focus of the laser sheet. The filters were used to ensure that the photodiode operated in the linear part of its response curve when fully illuminated. A sharp-edged razor blade mounted on a translation stage was traversed through the laser sheet and the intensity plotted as a function of edge position. This intensity distribution was numerically differentiated and the thickness of the laser sheet taken to be the full-width at half-maximum of this trace. The calculated laser sheet thickness was 0.32 mm. The setup for the laser sheet thickness measurement and the plot of the differentiated intensity distribution are shown in Figure 4.2.

The experimental arrangement for the saturation irradiance measurement is sketched in Figure 4.3(a). As previously mentioned, the saturation measurement was performed using a hydrogen/oxygen flame. The 5×10 mm mask was placed in front of the intensity detector, to ensure that the laser sheet is trimmed to a length of 10 mm, for detection by an Ophir energy meter. The laser energy was randomly varied, and PLIF images, exciting the $Q_1(8.5)$ transition of OH, taken for each energy. After this, a region within the flame was chosen and the mean of the PLIF signal in this region calculated.

Having measured the laser sheet thickness before, it was now possible to calculate the energy density for the laser sheet by dividing the measured signal by the irradiated area. A typical saturation curve for a fuel-rich flame is shown in Figure 4.3(b). The measured points were assumed to fit a distribution of the form (Palma 1998):

$$S_F = CI \left(1 + \frac{I}{I_{sat}} \right)^{-1} \quad (4.4)$$

where C is a constant and I_{sat} is the saturation irradiance. The form of this plot derives directly from Equation 4.2. The data shown in Figure 4.3(b) was fitted by varying these two quantities, providing a saturation irradiance at these conditions of $I_{sat} = 1000 \text{ MW/cm}^2$. As a comparison, typical irradiances for the OH PLIF visualizations in the scramjet combustor experiments were approximately 400 MW/cm^2 .

4.2.2 Response of the ICCD Camera

A 576×384 -pixel Princeton Instruments 576-S1 intensified CCD camera with 16-bit digitization dynamic range and variable gain was used to obtain the PLIF images. It was expected that different equivalence ratios yield different PLIF signals and therefore images were captured at different camera gain settings in order not to saturate the camera while still using a reasonable

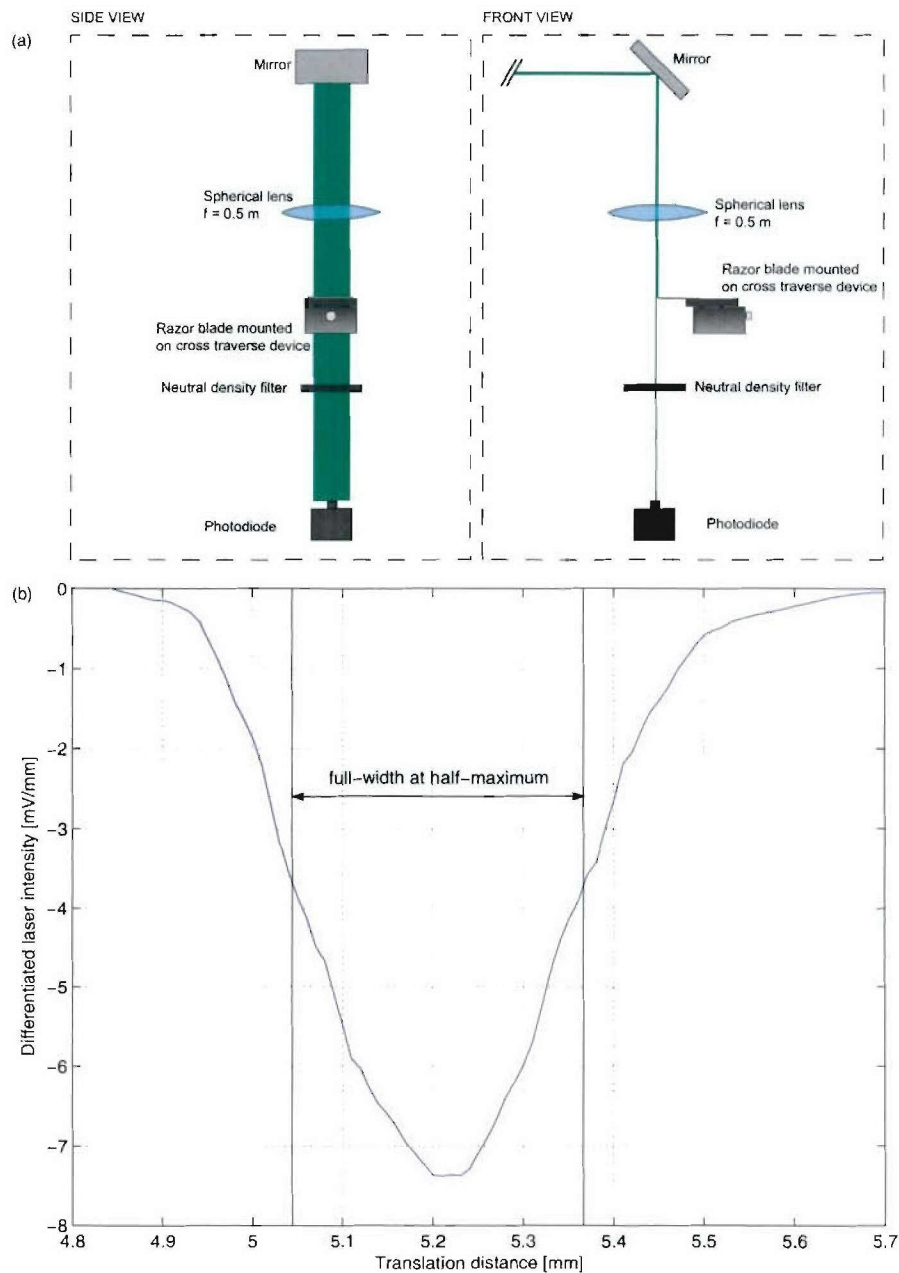


Figure 4.2: (a) Experimental apparatus for the laser sheet thickness measurement. (b) Measured profile (full-width at half-maximum 0.32 mm)

portion of the camera's dynamic range. This necessitates testing the linearity of the camera's response with changes in irradiance. For this reason the camera's response was examined at a series of different gain settings.

Once again for this calibration, we used the hydrogen/oxygen torch used for the saturation measurement. The torch was located at the the same position as the scramjet. The setup is the same as that sketched in Figure 4.3.

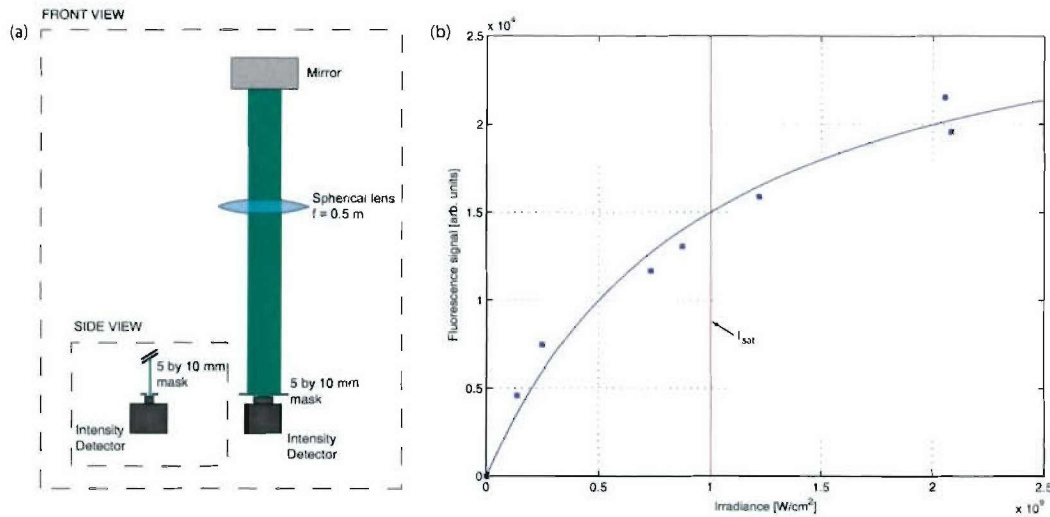


Figure 4.3: (a) Experimental setup for the saturation irradiance measurement. (b) Measured saturation irradiance and curve fit to the experimentally acquired data points.

The laser was adjusted to excite the $Q_1(8.5)$ transition of OH and the laser sheet was placed in the the same position as for the scramjet experiments cutting roughly through the middle of the flame. The energy of the laser was held at a constant level of about 10 mJ (measured with a Gentec ED-200 energy meter) and PLIF images of the flame were obtained at two different positions on the camera's CCD array, while varying the camera gain adjustment. Nominal camera gains of 3,5,6,7,8,9, and 10 were chosen, in random order. Figure 4.4 (a) shows an example of an OH PLIF image of the torch flame obtained at a camera gain of 8.

The average dark background signal, obtained with the lens covered, was subtracted from the images to eliminate the offset. A 15×15 -pixel region within the flame was chosen and the mean fluorescence signal within this region was calculated. Figure 4.4 (b) shows the resulting data points and an exponential fit to the measured points. This curve fit is necessary, due to the non-linear camera response. Using Equation 4.5, it is possible to compare the signal counts of images taken at different camera gain settings.

$$\text{Signal} = 10^{(0.2369 \cdot \text{gain} + 2.9827)} \quad (4.5)$$

This relation was used to compensate for the different camera gain settings between the different OH PLIF combustor experiments.

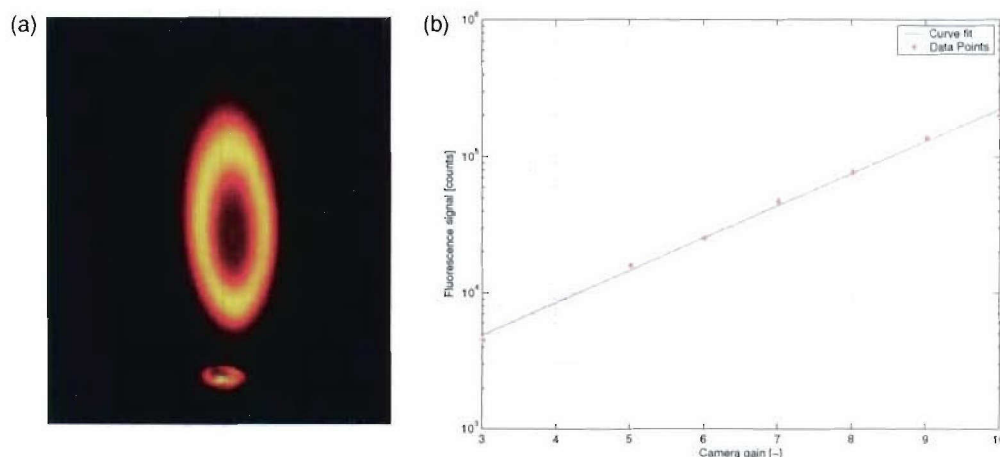


Figure 4.4: (a) Example OH PLIF image in a flame. The small disk at the bottom of the image is reflection of fluorescence from the torch (b) Camera response for different gain settings

4.2.3 Spatial Laser Profile Corrections

A laser beam has a non-uniform spatial energy distribution. Ideally it is Gaussian in both spatial and frequency domains, as is the energy of a laser-sheet generated from such a beam. Equation 4.1 highlights the linear dependence of the PLIF signal S_f on the laser energy E . Therefore PLIF images taken with heterogeneously distributed laser energies have to be corrected for spatial energy variations. Note that this correction assumes unsaturated fluorescence.

There are two commonly used methods used to determine spatial laser energy distributions in a laser sheet. If there exists a region of uniform fluorescing flow (e.g. the free stream) across the laser sheet and this is captured on the actual PLIF image, this region can be used to correct nonuniform flow regions. Since the flow field in a cavity flame-holder scramjet is highly turbulent and OH does not occur everywhere in the flow field, this method cannot be used to account for spatial variations in the sheet profile. Instead a CCD camera was used to capture the laser sheet image on a dye cell as shown in Figure 2.12.

The profile normalization procedure, which is part of the data reduction process using MATLAB®, consists of the following steps. First the separately captured background image is subtracted from the laser sheet image. Following that, the row with the maximum average signal (usually in the middle of the sheet profile) is identified. To obtain a smoother trace, 10 pixel rows above and below this maximum average signal row are averaged. The beginning and the end of the laser sheet are then determined. This can either be done by clicking on distinct points in the image or by using an automated algorithm that determines the maximum positive and negative gradients of intensity in the image. For some sheet profiles, the latter method showed problems finding the correct locations of the edges, therefore it was decided to manually select the laser sheet's extension. Once acquired, the sheet profile is normalized

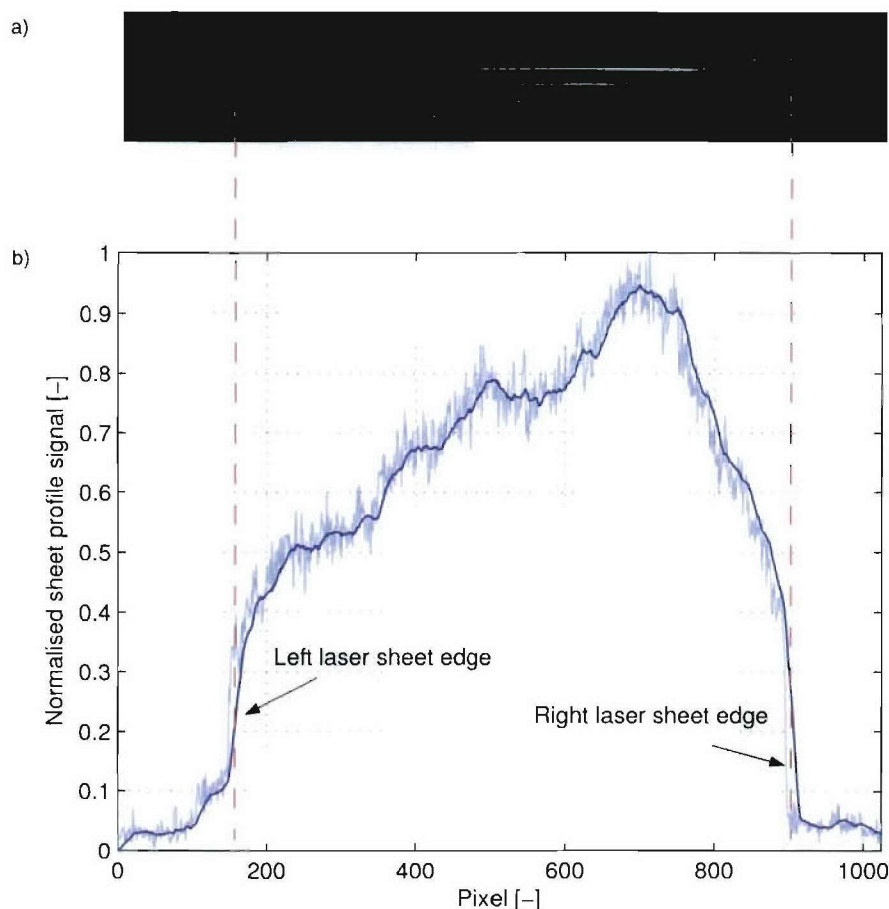


Figure 4.5: (a) Image of a laser sheet. (b) Plot of the Laser sheet profile. The light-blue line is the measured intensity (normalized to its peak value), the dark-blue line the smoothed trace.

to its peak signal and smoothed using a running average filter to remove high-frequency noise. Figure 4.5 shows an image of a typical sheet profile (a), a plot of the measured laser sheet intensity distribution, and the corresponding smoothed trace (b). The smoothed profile is then scaled so that the left and right edges map to the start- and end-pixels of the laser sheet in the PLIF image, as the PLIF image and the sheet profile image occur over a different number of pixels. The profile array must therefore be interpolated to the same length as the sheet image from the ICCD camera. Finally the values in the areas outside of the sheet profile are set to 1 so that this region of the flow field, outside the laser sheet, is not normalized. Each pixel in the PLIF image is then divided by the appropriate value of the smoothed profile to produce the final normalized PLIF image. It is apparent from Figure 4.5 that distortions in the optics generating the laser sheet can cause the profile to be fairly non-uniform. The relative intensity of the laser sheet profile was not allowed to be less than 0.3, as the normalization process becomes unreliable at low relative intensities.

4.2.4 Transition Choice

Before the experiments could be performed an excitation transition had to be chosen. Preliminary tunnel experiments and numerical simulations were conducted to determine a suitable transition. Three different excitations wavelengths yielding in reasonable fluorescence were identified resulting in a choice between the following transitions: R_1 (10.5), a combination of Q_2 (5.5) and R_{12} (5.5) and the eventually chosen Q_1 (8.5) transition. M^cIntyre et al. (1997) previously used the R_1 (10.5) transition with good results, hence this was a possible candidate of choice. Numerics predicted low temperature dependency for the combination of Q_2 (5.5) and R_{12} (5.5) transitions as Hubschmid and Bombach (2002) reported for the Q_1 (8.5) transition which was also used by Gruber et al. (2004) for their OH PLIF scramjet experiments. The Q_1 (8.5) transition was finally chosen because of its good combination of low temperature sensitivity, high fluorescence yield and lack of interference from surrounding transitions. Figure 4.6 shows the fluorescence signal strength plotted against the temperature indicating that the Q_1 (8.5) transition, as calculated by the LIFBASE code. This transition has relatively low sensitivity to temperature variations, especially for flame temperatures above 1800 K. Low temperature sensitivity is important because it is a requirement if the LIF signal is to be proportional to the OH mole fraction (Allen et al. 1993).

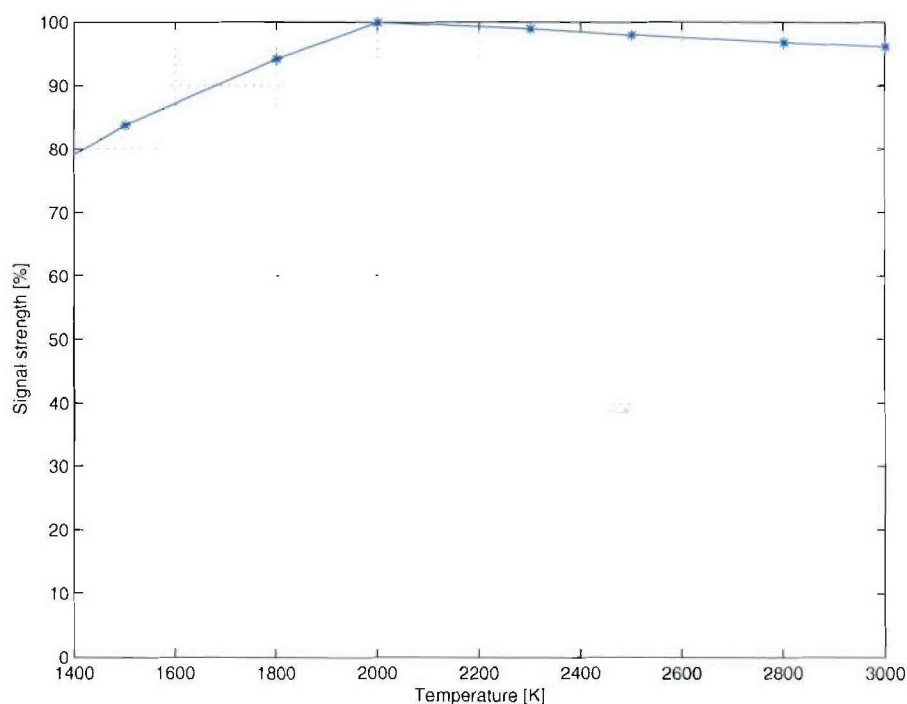


Figure 4.6: Variation of the Q_1 (8.5) transition LIF signal with temperature.

Figure 4.7, is a LIFBASE prediction of the fluorescence excitation spectrum around the Q_1 (8.5) transition for an assumed temperature of 1500 K and pressure of 101 kPa. The tran-

sition is well isolated from surrounding transitions, although there is some contribution to the signal from the relatively weak $P_{21}(8.5)$ transition near 283.55 nm.

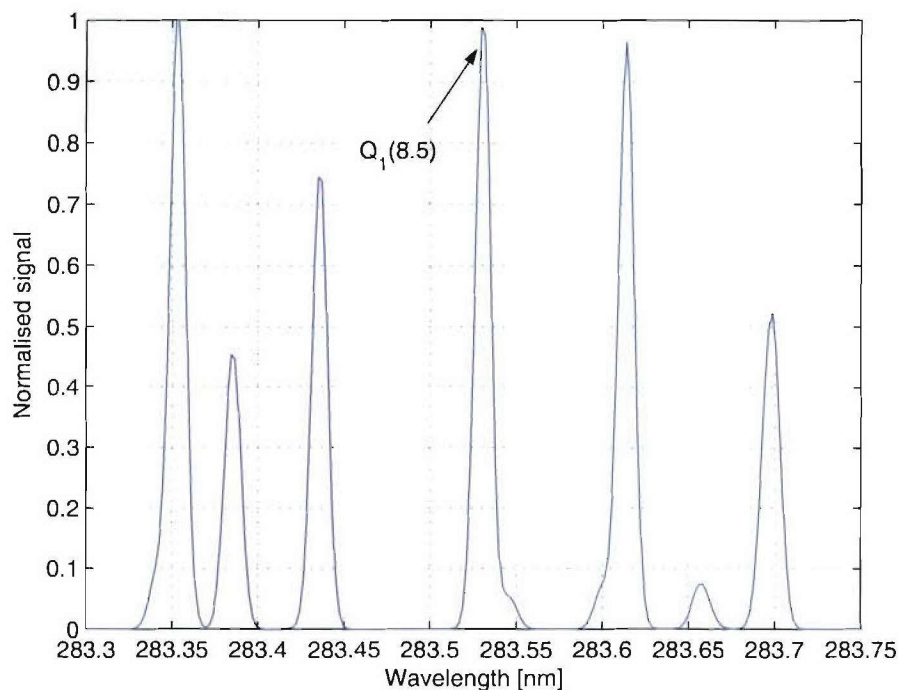


Figure 4.7: Numerical prediction of OH excitation spectrum assuming a temperature of 1500 K and atmospheric pressure.

4.2.5 Accuracy and Repeatability of Tuning on Transitions

Repeatability in PLIF signal from one tunnel run to the next depends upon how repeatably the laser can be tuned to the center of the transition. Errors in tuning will cause variations in the overall intensity of the PLIF signal. The tuning repeatability was measured by tuning and de-tuning the laser on and off the $Q_1(8.5)$ transition. The setup for this experiment was similar to the camera response experiment in Section 4.2.2. The laser energy was set to a constant 10 mJ and the hydrogen/oxygen flame was burning at constant flow conditions. The laser was tuned to the $Q_1(8.5)$ transition and ten acquisitions were taken and summed, to eliminate pulse-to-pulse fluctuations and any signal variability due to variations in the mode structure of the laser. The laser was then de-tuned several Angstroms either above or below the peak frequency and subsequently tuned back onto the line center and another ten images were acquired. This procedure was repeated ten times in total in both directions away from the center of the transition. Each of the ten images was averaged and the standard deviation calculated at each pixel. A 100-pixel-long slice from row 180 to 220 of the image, was selected and averaged. The mean signal (normalized to 1) and the fractional standard deviation are

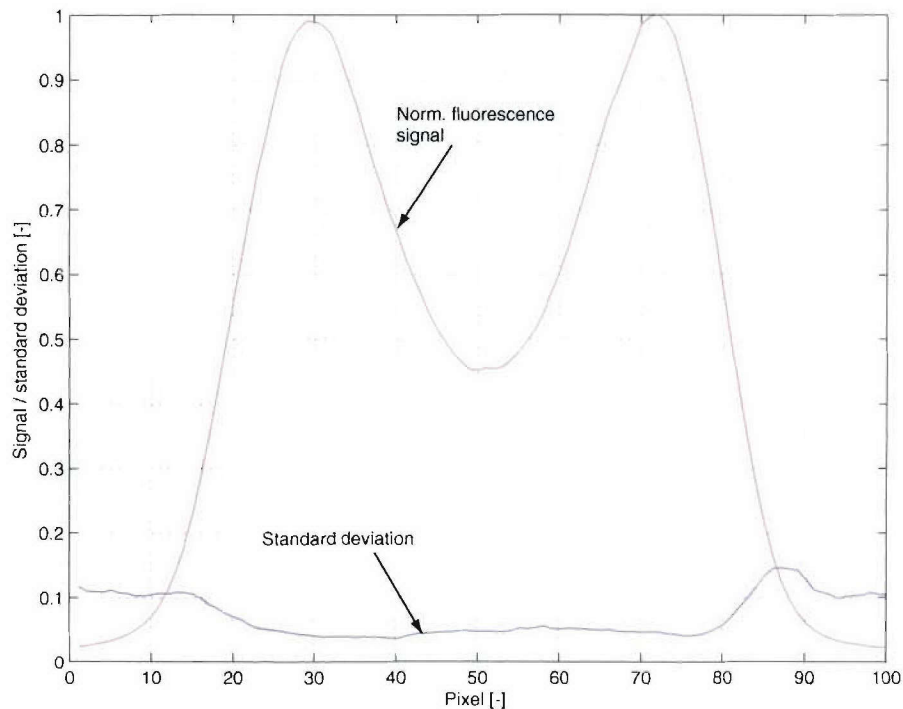


Figure 4.8: Accuracy of tuning the laser on the peak transition

plotted in Figure 4.8. Throughout the main part of the flame, the standard deviation is around 5%. The peak of the standard deviation is 15% on the edges of the flame. This is due to the low signal and the instability of the flame present in these regions rather than the tuning of the laser. Assuming the flame conditions stayed constant, this means that tuning to the transition peak is reproducible to 5% of the peak signal.

Another experiment was conducted to determine the shot-to-shot fluctuations between laser pulses. The laser was operated as usual, pulsing at 10 Hz. Ten pulses were recorded and the PLIF signal levels of each pulse compared. This again was repeated ten times. It was found that the signal varies within approximately 12% from pulse to pulse. Note that for the actual tunnel runs, fluctuations should be less than this because the overall change in laser energy is accounted for through the photodiode energy. Since this was not the case for this experiment, the fluctuations in PLIF signal of about 12% from shot-to-shot are worst-case estimates.

4.2.6 Focusing on the Image Plane

Since planar laser-induced fluorescence is a two-dimensional technique, it is required to focus the camera on a distinct plane in which the fluorescence will be excited and the resulting signal captured. For this purpose a grid was put at the laser sheet's location and the camera focused

while permanently acquiring images. Once in focus, 10 images were acquired and summed to get a distance calibration in the x- and y-directions, as shown in Figure 4.9. The resulting

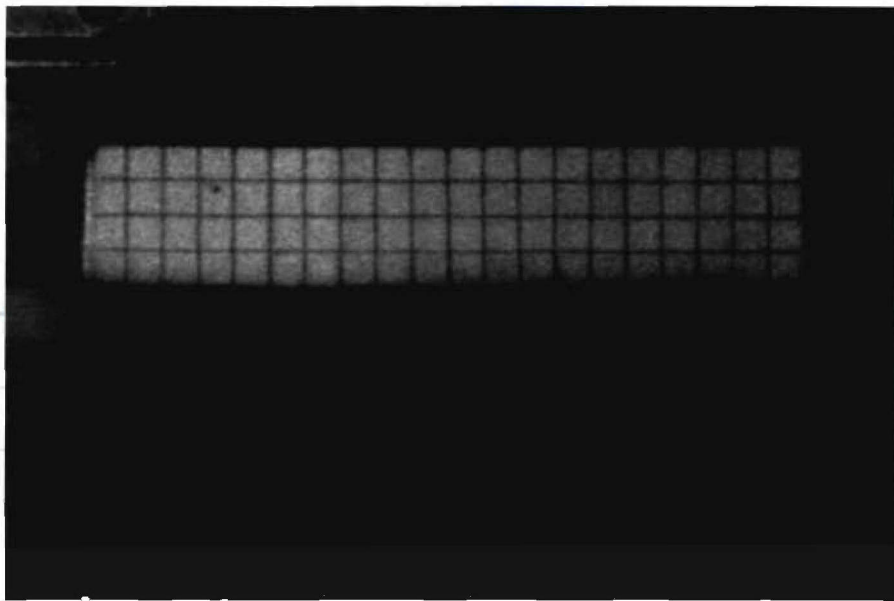


Figure 4.9: Grid image, used to focus the camera and to measure dimensions of flow structures

image can subsequently be used to determine dimensions, such as the laser sheet length or the length of turbulent flow structures. For these purposes the number of pixels in the x- and y-directions corresponding to the grid division was acquired and the ratio calculated to be 4.6 ± 0.1 pixels/mm. Each time the laser sheet was laterally translated or moved up- or downstream, this procedure was repeated to ensure consistent image scaling.

4.3 Computational Fluid Dynamics (CFD)

4.3.1 The CFD++[®] code

The CFD code to be used here is the commercial code CFD++[®], developed by Metacomp Technologies (Goldberg et al., 1997). CFD++[®] represents the state-of-the-art in commercial CFD codes. It can solve both the steady or unsteady (time-accurate), compressible and incompressible Navier-Stokes equations, including multi-species and finite-rate chemistry modeling. It is fundamentally an unstructured code, but handles Cartesian, structured curvilinear and unstructured grids (with various cell types and shapes), including hybrids. The discretization scheme

is Total Variation Diminishing (TVD). Riemann solvers are used to define interface fluxes, based on local wave-model solutions. A variety of turbulence models are available in CFD++[®], ranging from one- to three-equation transport models. Linear and non-linear (anisotropic) versions are available and all models can either be combined with wall functions or integrated directly to the wall. Large-eddy simulation sub-grid models are also available, including hybrid RANS/LES models which blend automatically according to the local mesh density. Multi-grid relaxation provides a fast and accurate solution methodology for both steady and (with dual-time-stepping) unsteady flows. Most importantly, CFD++[®] has had considerable investment concerning code validation (see for example Goldberg et al. (1997)) and has been used for scramjet applications by the CFD team at the USAF Wright-Patterson Research Laboratory.

4.3.2 Governing Equations

The governing equations that describe a chemically reacting high-speed flow are the Navier-Stokes equations coupled with $n - 1$ species mass continuity equations, where n is the total number of species considered and the last species (the *hidden* species for which the transport equation is not needed) is obtained by considering total mass conservation. These differential equations can generally be written as follows (Baurle 2004):

$$\frac{\partial \rho}{\partial t} + \frac{\partial}{\partial x_j} (\rho u_j) = 0 \quad (4.6)$$

$$\frac{\partial}{\partial t} (\rho u_i) + \frac{\partial}{\partial x_j} (\rho u_i u_j + \delta_{ij} p - \tau_{ij}) = 0 \quad (4.7)$$

$$\frac{\partial}{\partial t} (\rho e_0) + \frac{\partial}{\partial x_j} (\rho h_0 u_j + q_{ij} - \tau_{ij} u_i) = 0 \quad (4.8)$$

$$\frac{\partial}{\partial t} (\rho Y_m) + \frac{\partial}{\partial x_j} (\rho Y_m u_j + \rho Y_m v_j) = \dot{w}_m \quad (4.9)$$

where ρ is the fluid density, u_i is the velocity, p is the pressure, e_0 is the total energy, h_0 is the total enthalpy, τ_{ij} is the stress tensor, q_j is the heat flux vector and Y_m , v_j and \dot{w}_m are the mass fraction, diffusion velocity and production rate of the m^{th} species. The time-averaged equations are derived from Equations 4.6-4.9 by decomposing each transport/flow quantity Φ

into a mean and a fluctuating variable

$$\Phi = \tilde{\Phi} + \Phi' \quad (4.10)$$

and re-substituting the decomposed variables into the initial equations. Averaging the results yields the desired time averaged equations, for which subsequently further modeling assumptions are required. For a more detailed description of the complete modeling process the interested reader may be referred to Baurle (2004) and Anderson (1995).

4.3.3 Fluid Properties (Real Gas Thermodynamic Model)

Modeling chemically reacting flows makes it necessary to account for real gas effects such as variations of specific heats c_p and the computation of the chemical reactions. The thermodynamic model used is based on higher order curve fits. The entries for these quantities are those commonly found in thermodynamics property tables such as (M^cBride et al. 1963). The resulting equations are given as follows:

$$\frac{c_{p,m}}{R_m} = a_m + b_m T + c_m T^2 + d_m T^3 + e_m T^4 \quad (4.11)$$

$$h_m = R_m \left(a_m + \frac{b_m}{2} T + \frac{c_m}{3} T^2 + \frac{d_m}{4} T^3 + \frac{e_m}{5} T^4 \right) T + \Delta H_{f,m} \quad (4.12)$$

$$\frac{G_m}{R_m} = a_m (T - T \ln T) - \frac{b_m}{2} T^2 - \frac{c_m}{6} T^3 - \frac{d_m}{12} T^4 - \frac{e_m}{20} T^5 + \frac{\Delta H_{f,m}}{R_m} - g_m T \quad (4.13)$$

where $c_{p,m}$ is the specific heat at constant pressure for the m^{th} species and is a fourth order polynomial fit in temperature T with coefficients a_m , b_m , c_m , d_m and e_m . The enthalpy h_m of the m^{th} species is the integral of $c_{p,m}$ with respect to temperature T and $\Delta H_{f,m}$ is the enthalpy of formation of the m^{th} species. Finally, G_m is the Gibb's free energy of the m^{th} species. The constants a_m , b_m , c_m , d_m , e_m , g_m , and $\Delta H_{f,m}$ are tabulated in literature for various temperature ranges (M^cBride et al. 1963). Typically a two or three temperature range fit to $c_{p,m}$, h_m and G_m is applied.

4.3.4 Turbulence Modeling

The most widespread form of turbulence modeling is ensemble-averaging, in which the model accounts for all turbulent stresses arising from time-averaging the native Navier-Stokes equations. This category of modeling together with the flow equations in which it is embedded has acquired the name RANS (Reynolds-averaged Navier-Stokes).

A three-equation turbulence model was used for the computations presented in this report. This model is a combination of the commonly used two-equation $k - \epsilon$ model and Goldberg's one-equation R model. Many weaknesses of the $k - \epsilon$ model have been documented in the literature over recent years and as a result, various modifications have been suggested, one of which is the introduction of a third quantity. This results in Goldberg's $k - \epsilon - R$ model (Goldberg et al. 1988) which solves transport equations for the turbulence kinetic energy k , its dissipation rate ϵ , and the undamped eddy viscosity R in a manner that accounts for non-equilibrium conditions and avoids free stream turbulence decay under shear-free flow conditions and is recommended for supersonic/hypersonic applications.

4.3.5 Chemistry Model

Hydrogen/air combustion was modeled using both frozen and finite-rate chemistry. The forward reaction rates are given as functions of temperature according to the Arrhenius equation (Equation 4.14) for the j^{th} reaction

$$w_{f,j} = k_{f,j} T^{n_{f,j}} e^{\left(\frac{-E_{f,j}}{RT}\right)} \quad (4.14)$$

where $w_{f,j}$ is the forward reaction rate, $k_{f,j}$ is the frequency factor, $n_{f,j}$ is the temperature exponent, $E_{f,j}$ is the activation energy and R is the universal gas constant. The backward reaction rate $w_{b,j}$ is defined as the ratio of the forward reaction rate to the equilibrium constant

$$w_{b,j} = \frac{w_{f,j}}{K_{e,j}} \quad (4.15)$$

where the equilibrium constant $K_{e,j}$ again is calculated from the Arrhenius equation (Equation 4.14).

The hydrogen/air-chemistry was modeled using a 9-species 18-reaction model developed at the NASA Langley Research Center and presented by Drummond et al. (1987).

4.3.6 The Scramjet Simulation Model

Since a computational fluid dynamics code solves the RANS (Reynolds-averaged Navier-Stokes) equations on discrete points (see Section 4.3), the application of CFD to any fluid problem involves the generation of a mesh. The physical scramjet combustor as described in Section 2.2.1 was modeled using the commercial mesh-generator GRIDGEN[®] to create a three-dimensional structured hexagonal mesh. The precision of any CFD solution is dependent on the resolution of the mesh it is computed on, and hence careful consideration of the aerodynamic and computational modeling parameters is required. This aspect strongly influences the design of the mesh used to model the scramjet flow field.

The mesh needs to be refined in the vicinity of the wall to capture the boundary layer, as well as in regions where strong alterations to the flow occur, such as sharp edges, regions containing shock waves and especially injection and combustion zones. The geometry of the flow field dictates a reasonably fine mesh near the walls from the leading edge of the scramjet model since the leading shock forms from the intake tip, followed by a shock train traveling down the duct and interacting with the growing boundary layer.

Also of great importance is the region where the shear layer separates from the cavity's leading edge and reattaches further downstream. The flow field within the cavity, especially where fuel is injected, is another area of special interest and needs to be resolved properly. Hence the area where the recirculation zone is expected to form in the cavity needs to be meshed accurately.

The ability to realize the ideal mesh geometry is limited by computational resources. The simulations were conducted with the use of the Australian Partnership for Advanced Computing (APAC) National Facility supercomputer, located at the ANU, which provides the necessary interface for the CFD solver CFD++[®] as well as the computational power. The mesh geometry was broken into eight zones, each of which was computed on a single processor. Each CPU is limited to 1024 MB of system memory (RAM) and can be thereby limited in the density of cells that can be computed. This results in a trade off between precise solutions and reasonable computational effort.

Bearing in mind these restrictions, and taking advantage of the planar symmetry of the scramjet, a structured mesh containing approximately 2.3 million cells was created, simulating one half of the scramjet. The resulting mesh is shown in Figure 4.10, illustrating how the injectors were modeled and how their connection to the slanted rear wall was accomplished.

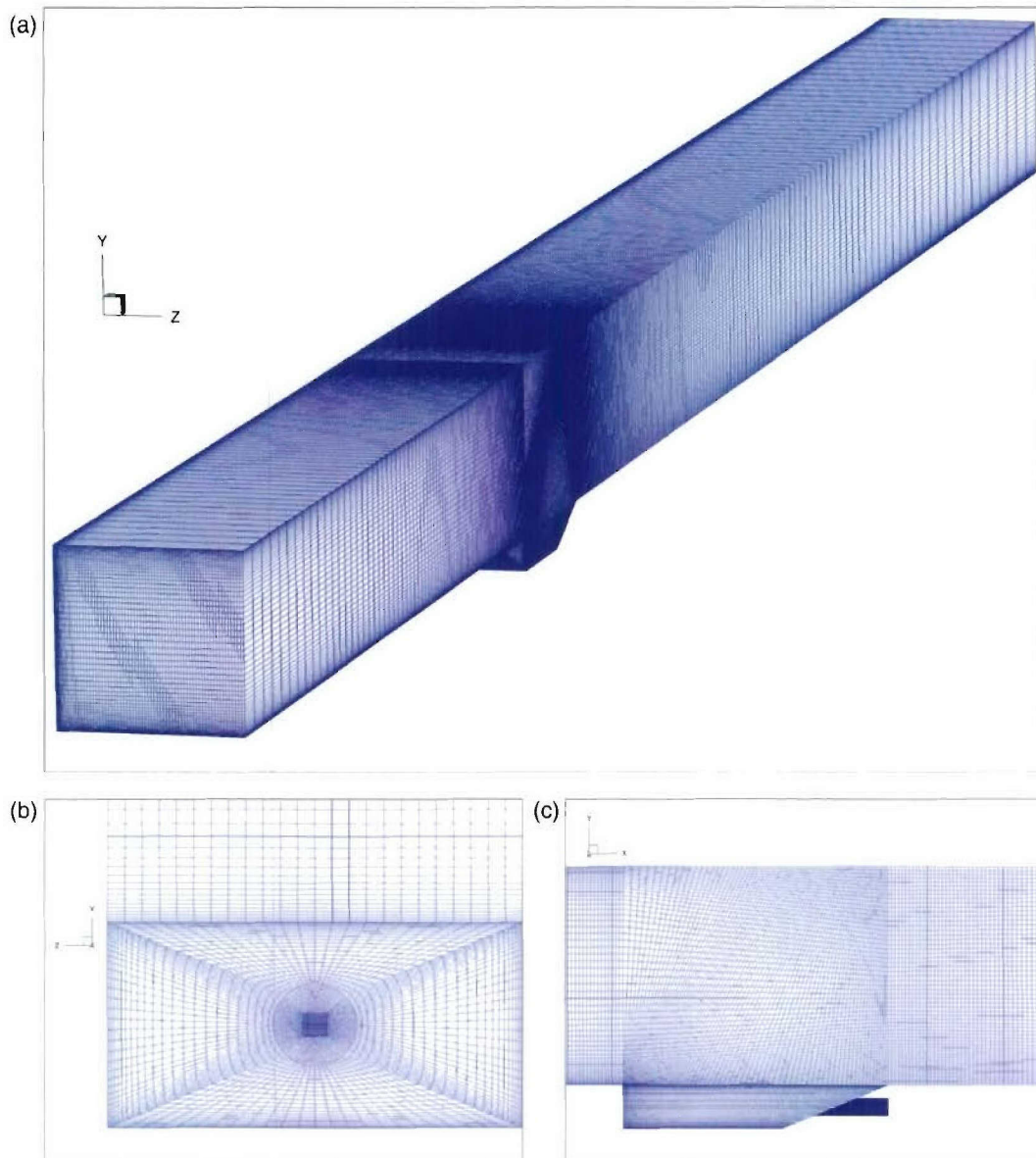


Figure 4.10: Computational mesh of the scramjet model: (a) isometric view, (b) rear view onto one injector, (c) side view

The boundary layer was not of primary interest, since the focus of this study was on mixing and combustion processes. It was therefore decided to use a wall function implemented in CFD++[®] rather than directly resolving the boundary layer including the viscous sub-layer, as this would have required too many cells. Thus the height of the first wall adjacent cells was set to be of the order of $5 \cdot 10^{-5}$ m. This results in about 18 cells within the boundary layer in the region before it separates from the leading edge of the cavity. The cavity contains about 500000 cells and the regions around the injectors were refined in more detail than surrounding regions. A portion of the injectors was modeled to allow for boundary layer development within the injectors and to represent a physically correct fuel jet (see Figure 4.10).

4.3.7 Initial and Boundary Conditions

After creating the mesh, the problem must be set up subject to initial and boundary conditions, thermochemical models and numerical procedures. Three different cases were simulated for one hydrogen equivalence ratio ($\Phi = 0.47$).

- nil-injection
- hydrogen injection into air - frozen reactions
- hydrogen injection into air - finite-rate reaction chemistry

The conditions at the intake were set to:

- inflow temperature $T = 1183$ K
- inflow pressure $p = 78500$ Pa
- inflow velocity $v = 2802$ m/s

Note that the temperature here is significantly lower than that of the STUBE calculation presented in Table 2.3. This is because the initial STUBE calculations were performed assuming vibrationally frozen flow. This leads to an underestimate of rotational temperature at the nozzle exit compared with the equilibrium calculation that properly accounts for all the thermal energy in the flow. The combustion calculations are therefore not directly comparable with the experiment, but they are included in the report because they supply important insights into the general features of mixing and combustion in these cavity combustors.

The composition of the oncoming flow was assumed to be standard air consisting of 21% oxygen and 79% nitrogen, a simplification of the actual flow delivered by the T3 shock tunnel, which also contains radicals generated in the stagnation region of the nozzle, as shown in Table 2.3.

The walls were set to a constant temperature of 300 K and a no-slip boundary condition was applied. This accounts for the fact that the flow does not have the time to heat the combustor walls over the very short experimental test period.

For the simulations incorporating fuel injection, the hydrogen mass flux was initialized to 5.65 g/s (see calibration in Section 2.3) which is half of the experimental flow rate since only half of the scramjet was modeled. The hydrogen injection temperature was approximated with 250 K, which corresponds to sonic conditions presumed to exist at the choked nozzle exit as the fuel is expanded from the Ludwieg tube.

If a solution with chemical reactions was sought, a 9-species 18-reactions hydrogen/air chemistry model presented by Drummond et al. (1987) was implemented, treating nitrogen as inert to reduce the complexity of the computation. Hence, dissociation of nitrogen and formation of NO_x was not considered by this chemistry model.

Chapter 5

OH PLIF and CFD Results

This chapter describes the second series of experiments, measuring the qualitative distribution of OH concentration and pressure in a supersonic combustor flow. CFD calculations of the cavity combustor flow field are also presented and discussed. Planar laser-induced fluorescence was applied on the cavity scramjet described in Section 2.2 to visualize OH radicals produced during combustion. Additionally, pressure measurements were obtained at twelve positions in the scramjet duct. This is an extension of the “pressure-only” experiments conducted in Chapter 3. Two different fuels, hydrogen and ethylene, were investigated at three equivalence ratios each and at combustor entrance conditions outlined in Section 2.1.4, corresponding to a flight Mach number of 11.5. CFD calculations, using the CFD++[®] computational fluid dynamics package were conducted and the results compared to the experimental data.

The pressure analysis in this chapter will be constrained to new objectives such as comparison with PLIF images and CFD and to highlight differences between these measurements and the previous investigation. MATLAB[®] scripts were written to visualize the time dependency of the pressure traces, resulting in time dependent pressure animations allowing a immediate visualization of the pressure history immediately after a tunnel run, providing the ability to compare tunnel runs obtained at different conditions.

Figure 5.1 shows the three positions relative to the cavity at which fluorescence measurements were obtained. The first plane (*laser sheet position 1*) was located in the middle of the scramjet duct, starting approximately 5 mm upstream of the cavity leading edge and extending about 2.5 cavity lengths downstream.

The second location, (*laser sheet position 2*), was laterally shifted by 5 mm but had the same dimensions in terms of starting position and length as position 1. The last plane examined,, (*laser sheet position 3*), coincided with position 2 but began one cavity length downstream of the rear-facing step. In total approximately 3.5 cavity lengths downstream of the rear-

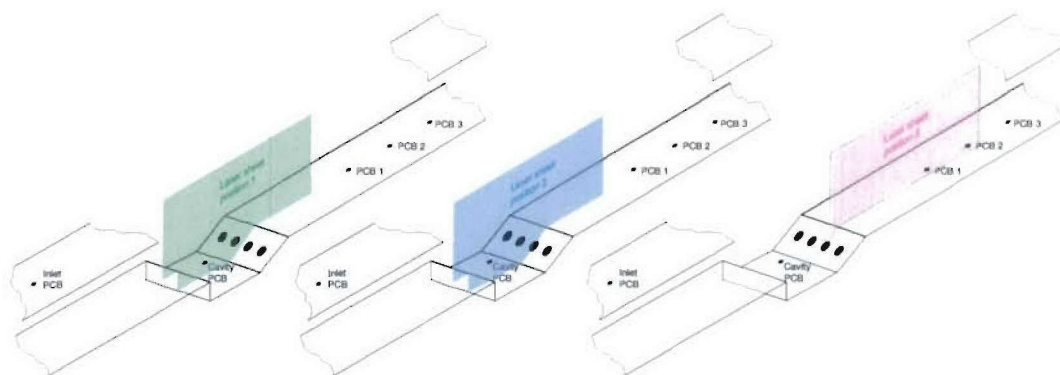


Figure 5.1: Laser sheet locations (from left to right): in the middle of the duct above the cavity, above a fuel injector port above the cavity and above a fuel injector port shifted downstream of the cavity.

facing step were covered. As Fig. 5.1 shows, the location of *position 3* allows some comparison between PLIF and pressure measurements as it overlaps with the locations of transducers 1 and 2.

5.1 Experimental Results

5.1.1 General Observations

Throughout the course of this experimental study, several OH PLIF images at three different locations — above and about the cavity and downstream of the cavity (see Figure 5.1) — were obtained using the $Q_1(8.5)$ transition of the $A^2\Sigma^+ \leftarrow X^2\Pi(1,0)$ rovibronic band of the hydroxyl (OH) radical excitation spectrum. Since the shock tunnel generating the free stream conditions (at a flight Mach number of 11.5) is a pulsed facility, only one image could be acquired during each facility run. Hence, the number of images acquired for the different fuel conditions is restricted to only one or two each, except for the highest hydrogen equivalence ratio where three images were acquired at laser sheet position two (above an injection port) as a repeatability study. With such a small sample size, it is not possible to conduct a quantitative uncertainty analysis of the measured PLIF signal based on run-to-run signal variations. The data reduction process used to obtain the results presented in this section is described in Section 2.5.

Figure 5.2 shows a typical image of the spatial OH distribution for the highest hydrogen equivalence ratio ($\Phi = 0.47$) acquired at position 2. All the major flow features that can be observed on the images have been labeled for easier referencing in the text.

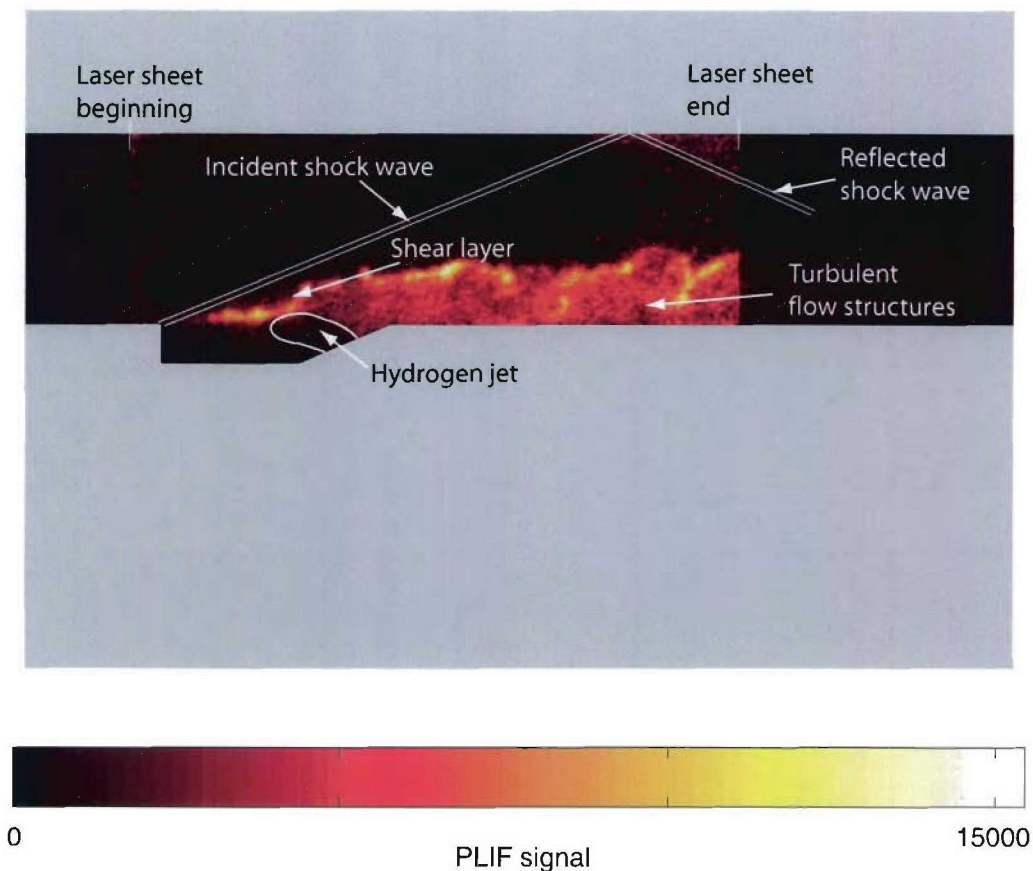


Figure 5.2: Typical image of the spatial OH distribution, hydrogen fuel ($\Phi = 0.47$), acquired on a plane over an injection port. Max. signal counts = 15000, camera gain = 9.

The color bar indicates the intensity of fluorescence signal collected by the ICCD camera. The spatial signal distribution shown in Figure 5.2 does not match the one initially imaged on the camera, since the scatter has been subtracted from the raw image which has additionally been corrected for spatial laser intensity variations as described in Section 4.2.3. The peak signal on the resulting image is 15000 counts at a camera gain of 9. The high velocity gradient between the slow-moving cavity flow and the supersonic free stream causes a separated shear layer to form above the cavity. This shear layer enhances the mixing of the oncoming flow with the fuel introduced into the cavity. The friction within the detached shear layer results in high temperatures and consequently leads to auto-ignition of either hydrogen or ethylene fuels. Since OH is an intermediate combustion product helping to maintain and stabilize the combustion process, it can be used to indicate where ignition is occurring in the flow. Figure 5.2 shows that the highest PLIF signal is present in the region where the shear layer ignites the mixture, at the interface between the free stream and the fuel.

The filling of the cavity with fuel provides an obstacle for the oncoming supersonic flow,

and an oblique shock wave forms. This oblique shock impinges on the scramjet roof and is reflected, as seen in the brighter region in the PLIF image in Figure 5.2. Since no OH exists in this part of the duct, the higher signal is due to luminosity as the flow gets heated and is therefore more luminous as it passes through the oblique shock wave.

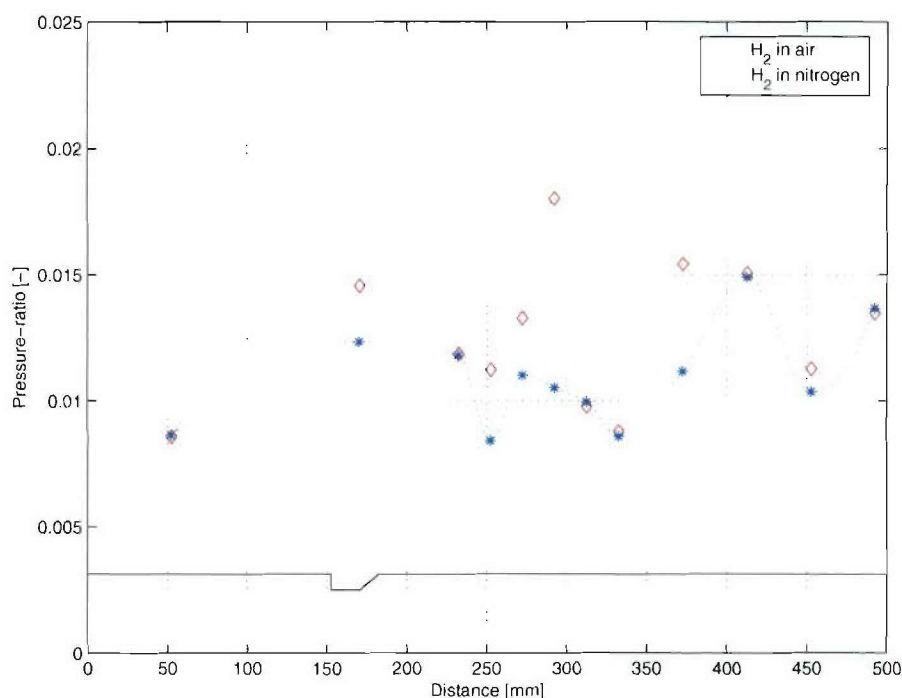


Figure 5.3: Pressure distribution during nominal test time for hydrogen injection into air and nitrogen, ($\Phi = 0.47$).

The geometry of the cavity generates recirculating flow, that together with the comparatively low velocities within the cavity assists the mixing process by increasing the residence time of the fuel/air mixture in the combustor. In the cavity itself the hydrogen/air-mixture is highly fuel-rich ($\Phi \gg 1$) and the temperature is below the auto-ignition temperature. Although there may be some degree of mixing between the fuel and the air in the cavity, the temperature is too low for the mixture to react within the cavity. This is borne out by the fact that no OH signal is evident within the cavity. As there is no OH evident in the cavity, we cannot directly comment on the amount or efficiency of mixing.

Above the maximum penetration height of the OH plume the conditions are fuel lean. The hydrogen jet pressure is not sufficient to penetrate far into the free stream, so the OH signal is limited to the lower portion of the duct. Figure 5.3 plots the pressure ratio against axial distance (the pressures measured were normalized to the stagnation pressure) for both injection into air and into nitrogen. This plot shows only a very small difference in static pressure for the first pressure transducer downstream of the cavity. As OH was imaged only as far as transducer 2, it is not entirely clear whether the combustion process extinguishes downstream of the cavity

before re-ignition occurs due to the flow passing through the reflected shock originating from injection.

The reflected oblique shock wave can be seen clearly near the top of the duct and inferred elsewhere in the duct for Figure 5.4, a PLIF image captured further downstream at position 3.

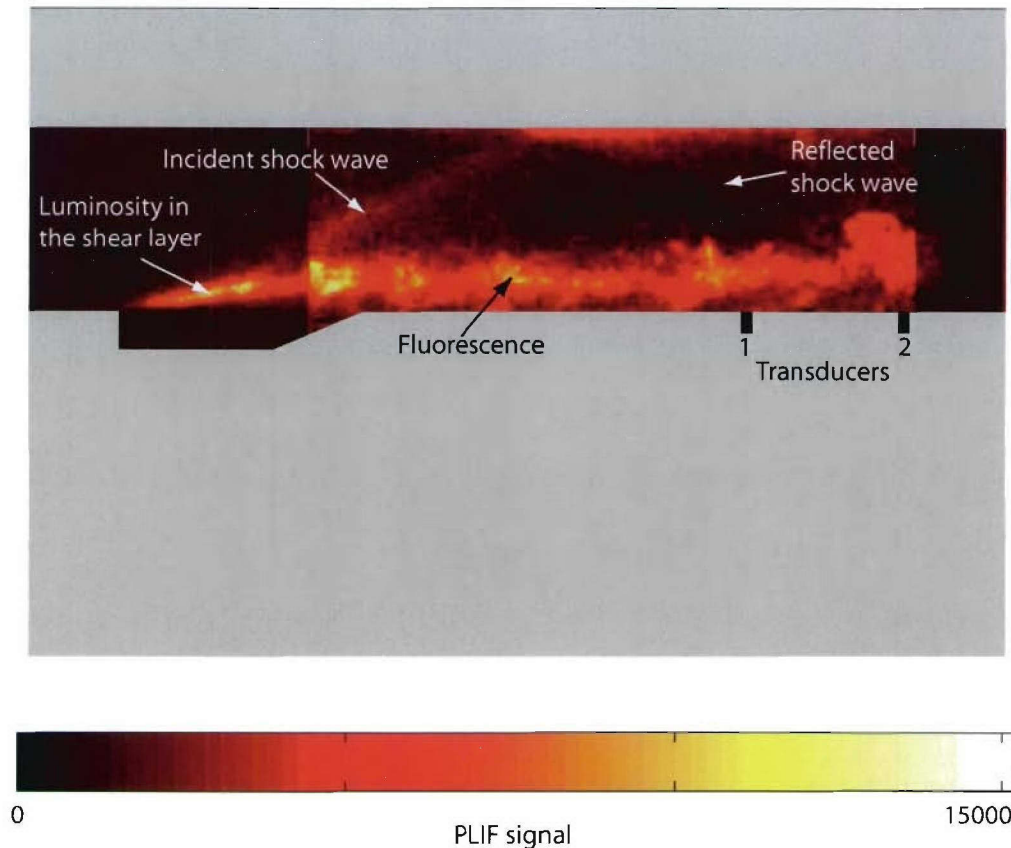


Figure 5.4: Typical image of the spatial OH distribution, hydrogen ($\Phi = 0.47$), acquired on a plane over an injection port downstream of the cavity, max. signal counts 15000, camera gain 8.

The path of the reflected shock wave through the fuel plume appears to correspond to a sudden increase in OH PLIF signal, indicating that the passage of the shock through the fuel increases the combustion. The locations of the first two pressure transducers are also shown in Fig. 5.4. Transducer 1 appears downstream of the duct, where combustion is apparent, while transducer 2 lies immediately upstream of the location of the shock impingement on the duct floor. Comparison with the axial pressure distributions for injection into air and nitrogen is interesting. Comparing the pressure distributions for injection into nitrogen and air indicates that there is no significant pressure rise for this tunnel run due to combustion at transducer 1. Transducer 2 is located immediately upstream of the impingement of the shock wave at the floor. Figure 5.3 indicates that for injection into air the static pressure increases sharply

downstream of transducer 2. This is consistent with Fig. 5.4.

The PLIF images also provide information about the turbulent structures within the flow. One possible way to visualize these patterns is to plot the longitudinal and transverse integrated signal distributions. This has been done by integrating the PLIF signal in either the y- or x-directions and plotting against the other axis. The resultant spatial signal distributions are shown in Figure 5.5. The transverse distribution identifies the penetration height of the OH

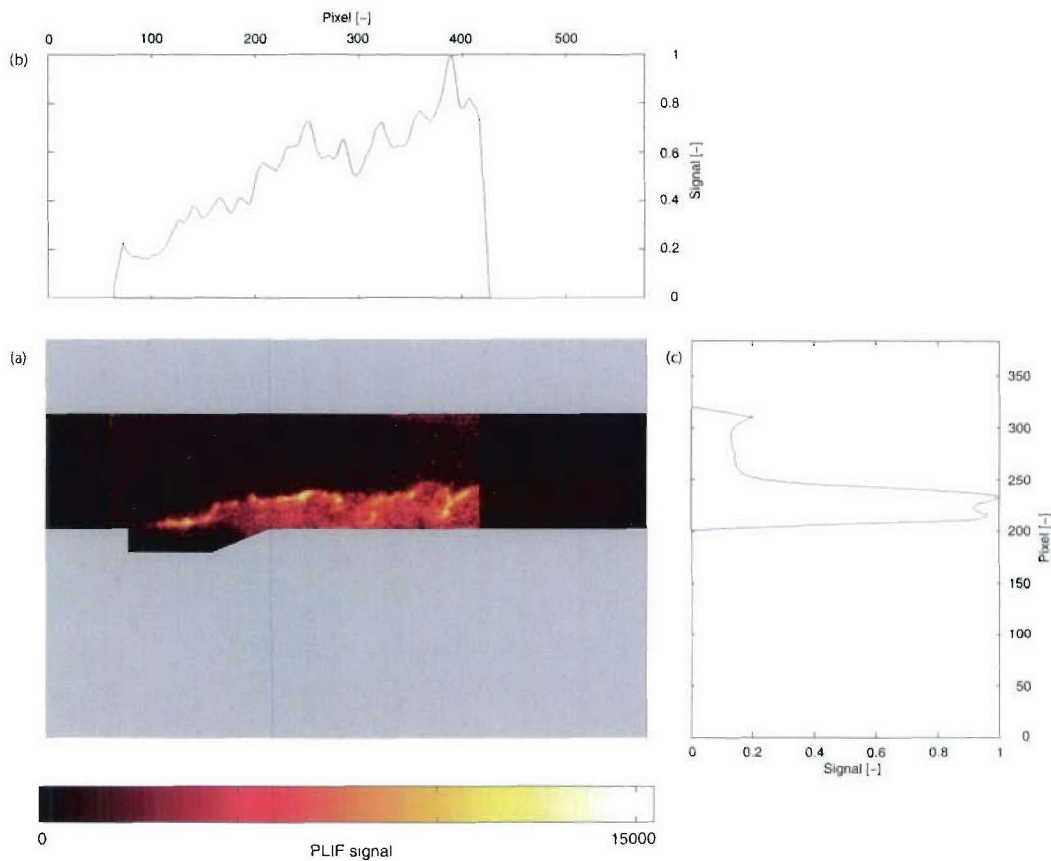


Figure 5.5: Spatial PLIF signal distributions, hydrogen ($\Phi = 0.47$): (a) shows the PLIF image (15000 counts, camera gain 9), (b) is the longitudinal plot of the PLIF signal distribution, (c) is the transversal plot of the PLIF signal distribution.

plume displayed as the lower peak of the distribution. Knowing the correlation between pixels and physical dimensions (as per description in Section 4.2.6) this height can be computed. For the example discussed (hydrogen ($\Phi = 0.47$)) it is 11.3 ± 0.5 mm. The nonzero offset above the shear layer can be explained by luminosity of the tunnel flow and residual laser scatter remaining after the subtraction. The second peak is mainly due to the shock impingement on the top window of the scramjet. The longitudinal distribution reveals a repetitive wavelike pattern of signal peaks followed by lower signal. An overall OH signal increase towards the right of the laser sheet edge can be observed as the plume is expanding. This indicates increasing

combustion with downstream distance. The identified structure in the flow pattern is caused by turbulent fluctuations in the combustor flow, perhaps due to oscillation of the cavity flow. The streamwise spacing between consecutive maxima in the PLIF signal is of the order of 10 – 20 mm.

In addition to the PLIF images, luminosity images (obtained by running the camera without a laser pulse during a tunnel run) were acquired for each fuel condition. This shows the amount of signal originating from luminous flow, high temperature regions which do not necessarily contain only OH radicals but which produce signal that adds noise to the measured fluorescence. These luminous effects can naturally also be observed on the actual PLIF images, although the amount of signal caused by luminosity is made as small as possible compared with the fluorescence signal by filtering in time and frequency. In contrast to the PLIF signal, which originates from a planar laser sheet, the luminosity images present the overall integrated signal across the imaged part of the flow field. Figure 5.6 shows a comparison between a PLIF image and a luminosity image, both acquired for equivalent fuel conditions (hydrogen ($\Phi = 0.47$)). Note that these images were obtained at different camera gains, hence relatively lower number of signal counts is measured on the luminosity image which was recorded on a (lower) gain of 8, whereas the PLIF image was captured using a camera gain of 9, with a sensitivity that is greater by a factor of 1.7. For this pair of images, the peak fluorescence signal is approximately three times the intensity of the luminosity.

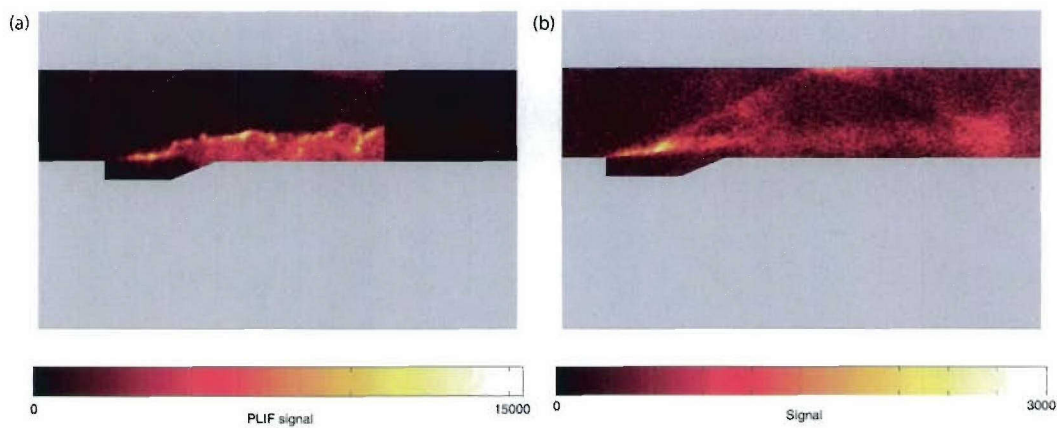


Figure 5.6: Comparison between PLIF image (a) and luminosity image (b), hydrogen ($\Phi = 0.47$). The PLIF image (a) has a maximum of 15000 signal counts at a camera gain of 9, the luminosity image (b) has a maximum of 3000 signal counts at a camera gain of 8.

The luminosity images are useful for identifying shock locations and in determining where the combustion is strong, as those regions tend to produce more luminosity. Figure 5.6 (b) highlights the region with the peak signal to be right above the first half of the cavity where the shear layer ignites the fuel/air mixture. The oblique shock wave forming on the cavity's leading edge and the reflected shock can be clearly seen, the latter perhaps reigniting the flow as

mentioned previously. The increase in luminosity signal in this region is indicative of increased combustion.

5.1.2 Repeatability

As mentioned previously, only a few PLIF experiments were conducted for each fuel condition and laser plane position, except for the highest hydrogen equivalence ratio ($\Phi = 0.47$) where three images were captured on a plane above a fuel injection port and around cavity at position 2. These three experiments were all performed at the same camera gain with similar laser irradiance. However the resulting PLIF images vary significantly in terms of the local flow structures and the maximum PLIF signal counts. This is to be expected, as supersonic combustion in a cavity is highly turbulent.

Figure 5.7 presents the resulting PLIF images showing the variations in maximum PLIF signal. As explained in Section 4.2.5 the system can be tuned and re-tuned to the peak of the $Q_1(8.5)$ transition frequency with an uncertainty of 5% and other error sources such as fluctuations in laser pulse-to-pulse energies are also relatively low (at the worst 12%). Hence the variations in peak PLIF signal are mainly due to the turbulent flow field, which is different for each tunnel run and varies significantly at different time during the same run. After normalizing to the sheet profile as described in Section 4.2.3, the signal varies from 14000 to 28000 counts (standard deviation 40%), showing that it is difficult to derive a quantitative comparison of signal for different equivalence ratios without averaging over a very large number of tunnel runs.

In contrast to the absolute PLIF signal, there are similarities in the flow that can be observed for each experiment. For this purpose the longitudinal and transversal signal versus distance plots introduced in Figure 5.5, are plotted on the same graphs (Figure 5.8) for the three experiments conducted at the high hydrogen equivalence ratio ($\Phi = 0.47$).

Looking at Figure 5.8 (b) it is apparent that the global flow conditions are quite reproducible and therefore a quantitative relation for different equivalence ratios can be derived as will be shown in Section 5.1.3. For these conditions the penetration height of the OH plume is about 11.3 mm. The axial distributions (Figure 5.8 (a)) also point out a behavior that is similar for all three experiments.

In terms of pressure the run-to-run variations are comparatively small. Besides the previously mentioned fluctuations in the inlet transducer signal, the pressure measured in the oscillating cavity and the pressure recorded at transducer 12, the measurements are very repeatable as illustrated in Figure 5.9. The variations at transducer 12 are presumed to be due to the impingement of a reflected shock wave in the vicinity of this transducer, which can cause sig-

nificant variability. The pressure fluctuations in the cavity are presumably due to oscillations as described in Section 1.1.1. Small differences in the flow field, caused by slight variations of the shock tunnel conditions, turbulent alterations from experiment to experiment and cavity induced unsteady flow phenomena cause the shock to move back and forth across the transducer varying the pressure recorded for each experiment.

It was assumed that only the peak signal varies significantly from one tunnel run to the next. Therefore another method was introduced to express similarities for equal equivalence ratios, and differences for different equivalence ratios respectively. A region within the OH plume was selected (see Figure 2.16) and the mean of the signal calculated, which is a more sensible way than comparing peak values. This method provides better results than just comparing the peak fluorescence signals, but the averaged signal still varies from one run to the next with more than 20% standard deviation.

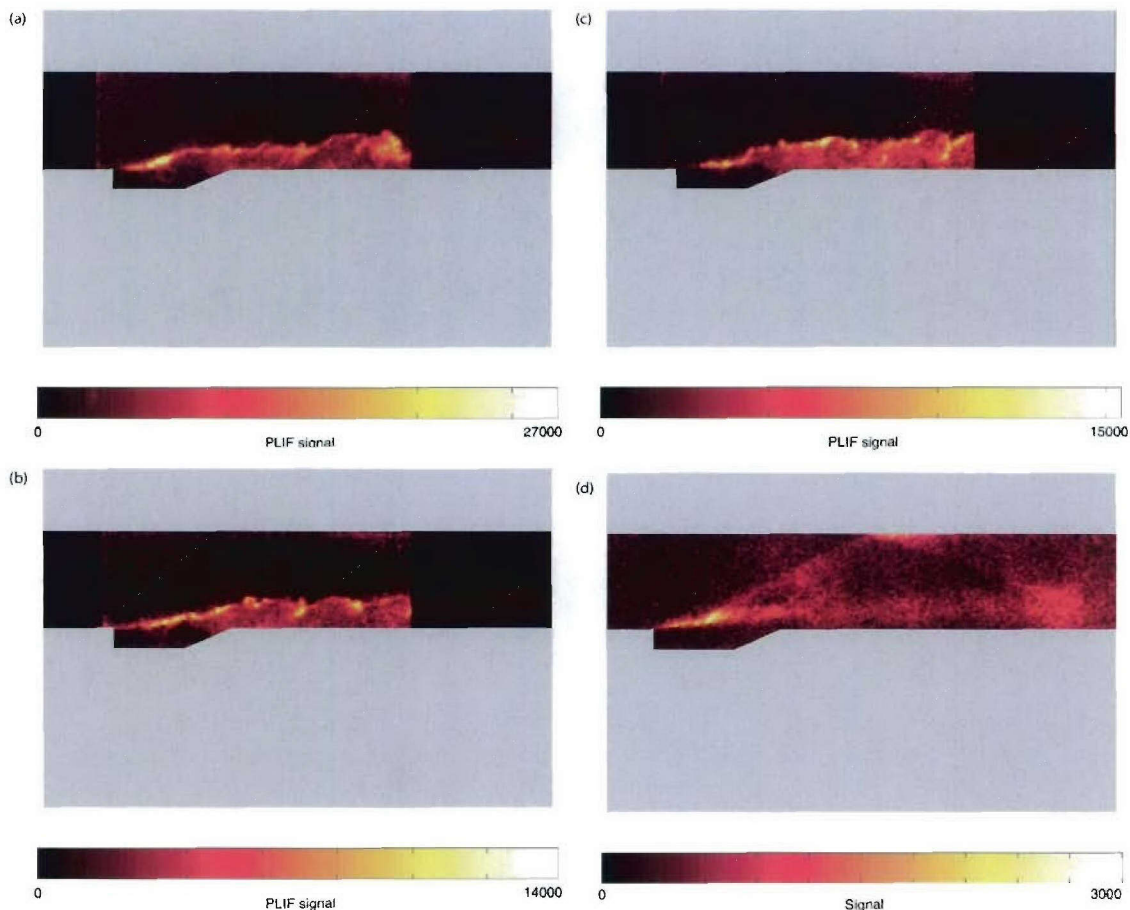


Figure 5.7: Repeatability of PLIF experiments, hydrogen ($\Phi = 0.47$), acquired on a plane over an injection port: (a) max. signal counts 27000, (b) max. signal counts 14000, (c) max. signal counts 15000, all taken at a camera gain of 9 (d) corresponding luminosity image, 3000 signal counts at a camera gain of 9.

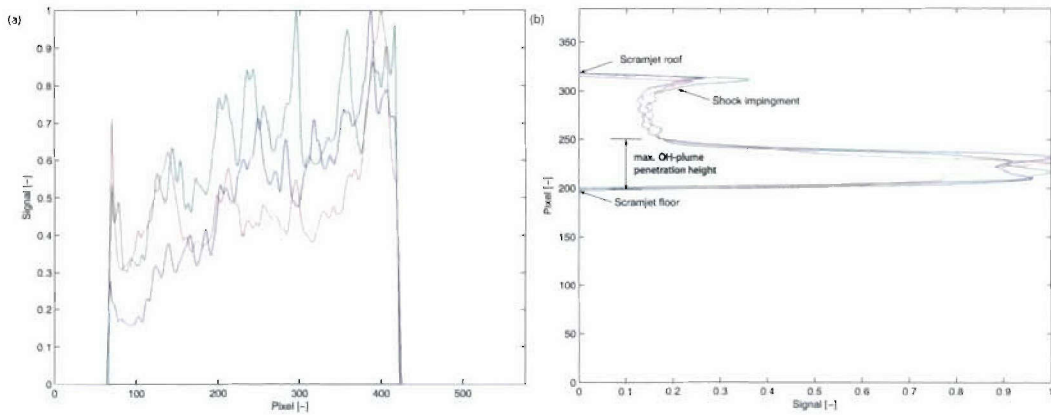


Figure 5.8: Repeatability of PLIF experiments: (a) shows the longitudinal PLIF signal distribution for three experiments conducted for the same conditions hydrogen ($\Phi = 0.47$), (b) the transversal distribution highlighting the repeatability of the experiments in terms of OH penetration height.

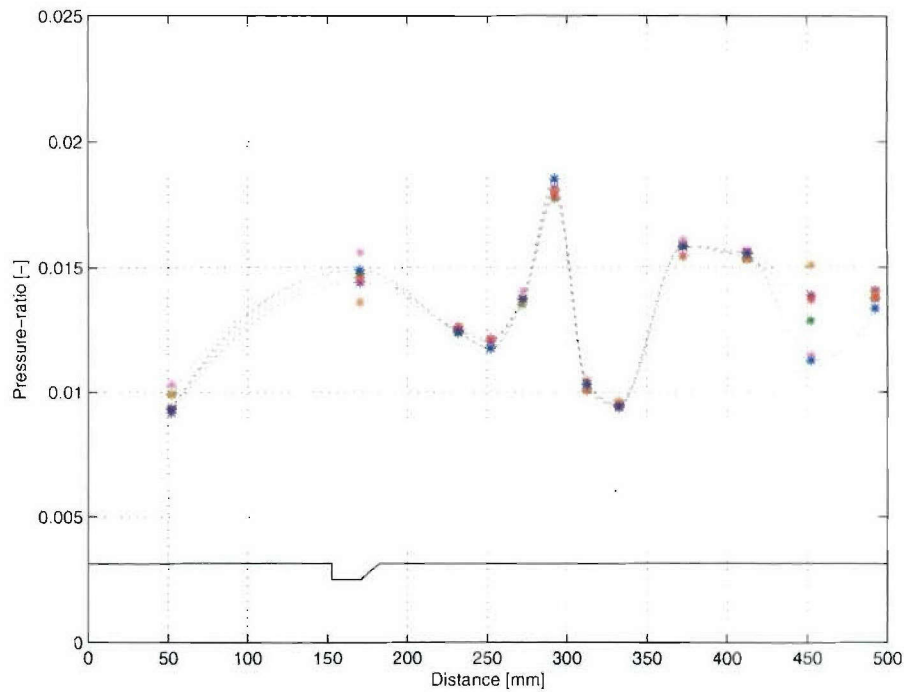


Figure 5.9: Repeatability of pressure measurements, hydrogen ($\Phi = 0.47$) axial pressure ratio plots for 6 randomly selected tunnel runs.

We can also compare axial pressure distributions between the first and second experimental campaigns. Figure 5.10 compares normalized pressure distributions along the duct between the two experimental campaigns for a range of ethylene equivalence ratios injected into air. Data from the second campaign is indicated in the figure legend by the suffix PLIF. The general

form of the pressure distributions that indicate the locations of shock and expansion waves along the duct are consistent between the two campaigns. Large variations in local pressures are, however, apparent. Some of this variation can be explained by fluctuations in the axial location of the shock train across the sparse array of pressure tappings. However, at locations 5 and 6 (312 and 332 mm downstream of the inlet) the measured pressures from campaign 2 are consistently lower than those from campaign 1. The difference is also greater than the run-to-run variation in pressure for the campaign 2 data. The reason for this is unknown. At the other locations, the pressures generally correlate with the global equivalence ratio.

5.1.3 Influence of Equivalence Ratio and Laser Sheet Location

This Section discusses apparent similarities and differences in the visualized flow with varying equivalence ratio, and with different locations imaged in the duct. A direct comparison between fuels is relatively difficult since the experiments for hydrogen and ethylene are conducted at different equivalence ratios because of the differences in molecular mass. The highest possible Ludwig tube fill pressure (2500 kPa) was chosen for both fuels to achieve the maximum feasible equivalence ratios for the current existing fuel injection system. The other two fill pressures were originally chosen to allow the resulting equivalence ratios of ethylene and hydrogen to match. Later a mistake was found in the method of calculating equivalence ratio, with the result that only the lowest equivalence ratios (0.15 and 0.13 for hydrogen and ethylene

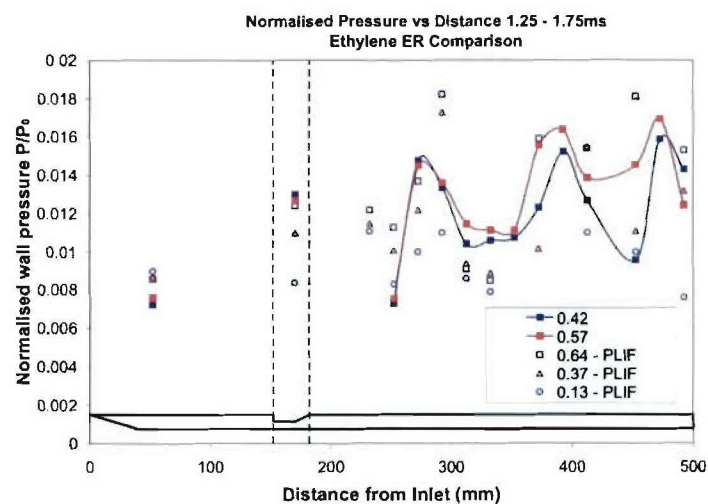


Figure 5.10: Comparison of normalized pressure distributions between experimental campaigns for a range of ethylene equivalence ratios injected into air.

respectively) allowed for a direct comparison of equivalence ratio between the two fuels.

5.1.3.1 Hydrogen Fuel

The equivalence ratios are controlled by altering the initial Ludwig tube fill pressure, as described in Section 2.3. This regulates the mass flux of fuel entering the cavity through the injectors. The effects of varying equivalence ratios will be discussed in this section. Figure 5.11 shows the PLIF images and the corresponding luminosity images for three different hydrogen equivalence ratios: (a) $\Phi = 0.15$, (b) $\Phi = 0.24$, and (c) $\Phi = 0.47$. Images were obtained on the plane above an injection port (position 2). The signal counts of the PLIF images are: 12000 for $\Phi = 0.15$, 11000 for $\Phi = 0.24$, and 15000 for $\Phi = 0.47$, the signal on the three luminosity images was 3000 counts. The included white lines aid the interpretation of the raw images which can be found in Appendix A. All images show similar turbulent flow structures, independent of equivalence ratio. The most obvious difference between the three images is the location at which OH signal first appears, which moves upstream towards the front corner of the cavity as the equivalence ratio increases. For the highest equivalence ratio (c) the flow starts to produce OH immediately after the cavity leading edge, as can be seen in both the PLIF and the luminosity image, whereas for the lowest equivalence ratio (a) observable OH signal is not apparent until about half-way along the cavity length. Such behavior can perhaps be explained by the penetration length of the hydrogen jet in the upstream direction, since lower pressure results in less penetration of the jet into the flow, and vice versa. This also effects the angle of the shear layer, which is roughly parallel to the cavity floor for the low equivalence ratio and steepens with increasing fuel pressure as observed in the luminosity images. Another possible contributing factor is apparent from the luminosity images: higher equivalence ratios increase the jet penetration and therefore increase the angle of the shock wave produced. This in turn increases the flow temperature, which will decrease the ignition delay time.

Note that the dark region on the right-hand side of Figure 5.11 (b) is due to a crack in the top scramjet window preventing the laser sheet from exciting this region of the flow. This crack was probably caused by a diaphragm fragment colliding with the window. Fortunately this happened at the end of the second campaign, so only the last few images captured were affected.

As mentioned in Section 5.1.2, the signal counts vary significantly from one run to the next at the same equivalence ratio. It is therefore not possible to compare different equivalence ratios in terms of signal strength, meaning that higher signal in one image does not necessarily prove larger amounts of OH or excessive combustion in general, particularly when the differences are small (less than 20%). The pressure measurements, however, show how different equivalence ratios influence the overall combustion process. Figure 5.12 shows pressure-ratio (normalized by the stagnation pressure) versus distance plots for three different hydrogen equivalence ratios.

Note that the relative pressure rise between them is not only due to increased combustion but is

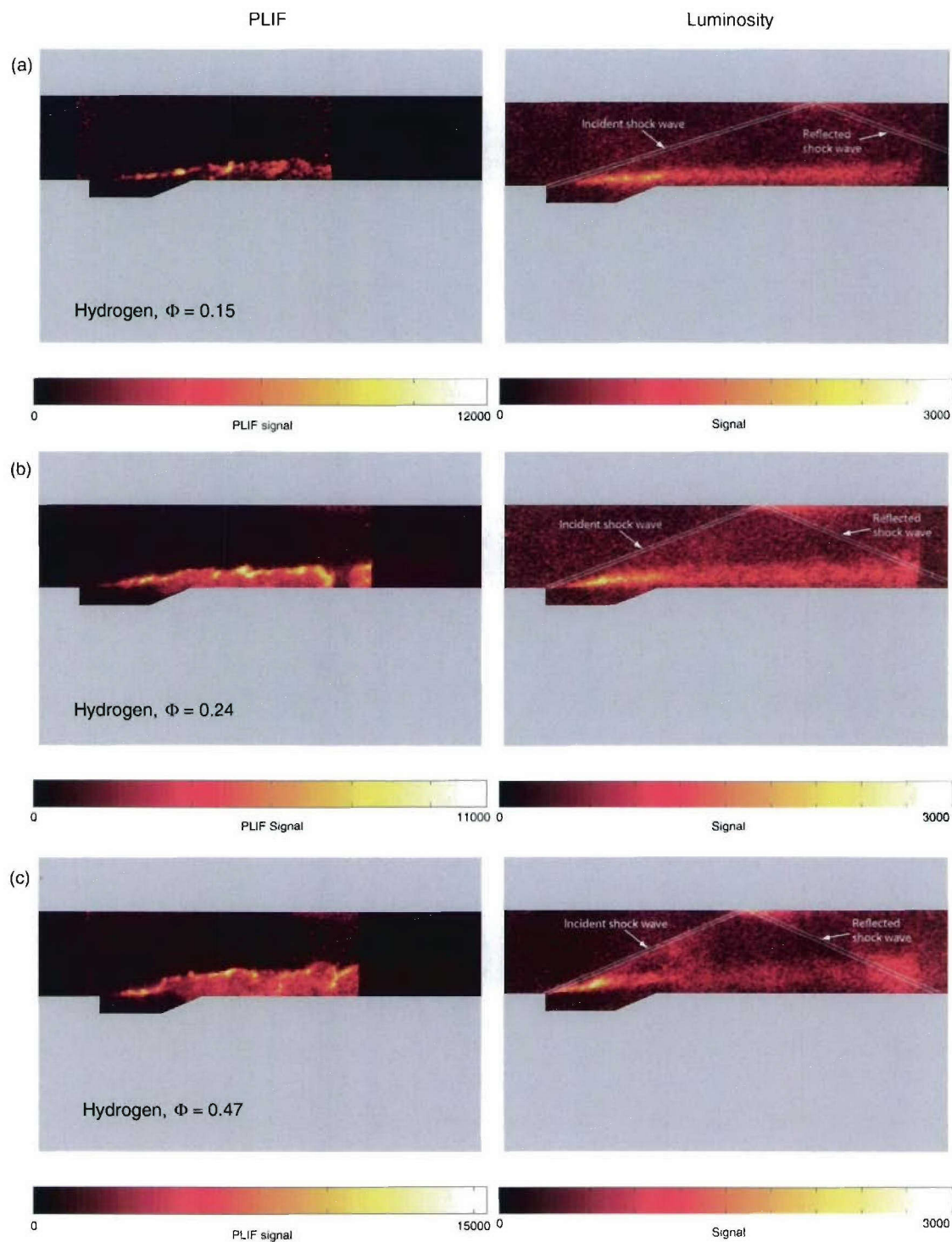


Figure 5.11: Effects of equivalence ratio variation (hydrogen), acquired on a plane over an injection port; the left column shows the PLIF images and the right the luminosity images: (a) $\Phi = 0.15$, (b) $\Phi = 0.24$, (c) $\Phi = 0.47$.

also caused by the introduction of different amounts of fuel. The first experimental campaign, and particularly Fig. 3.12 showed that the pressure increase is proportional to the fuel mass flux and hence to the equivalence ratio.

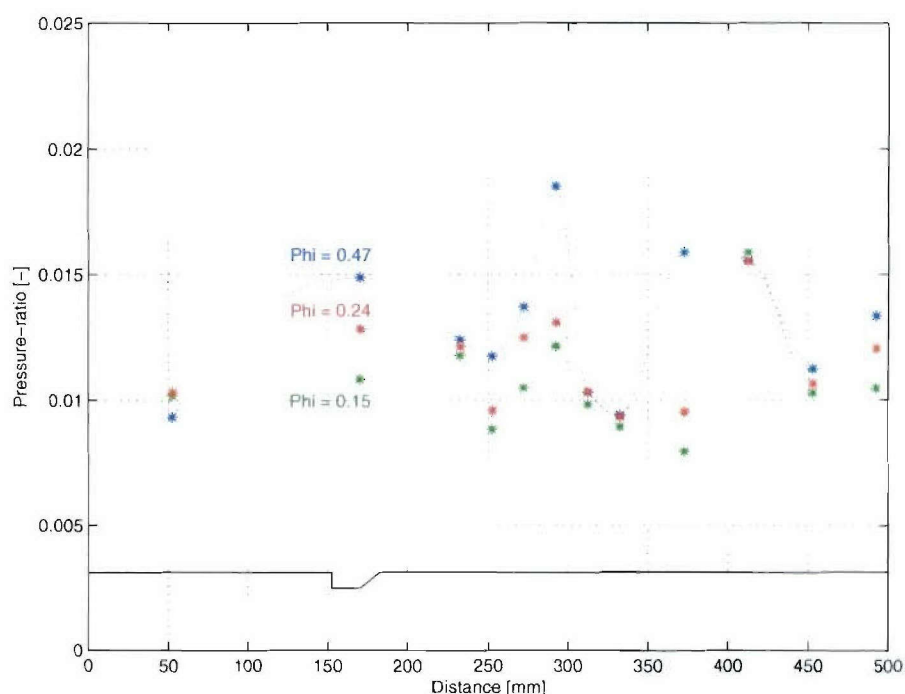


Figure 5.12: Pressure distributions for different hydrogen equivalence ratios.

Looking at Figures 5.11 and 5.12 and accounting for the results in Chapter 3, high OH signal does not necessarily coincide with strong pressure increases. This also emphasizes the importance of the pressure measurements which provide additional information besides the PLIF measurements which give information about where ignition will occur.

As mentioned before, increasing the mass flux of fuel increases the shock angle. This can be clearly seen on the luminosity images as the incident shock angle β_1 increases from 18° to 22° and 24° , for $\Phi = 0.15$, $\Phi = 0.24$ and $\Phi = 0.47$ respectively and the impingement points on the roof and the floor can be seen to move forward. This is supported by the upstream movement of the structure in the pressure plots with increasing equivalence ratio.

Higher fuel pressures also cause the fuel to penetrate further towards the duct center, hence the penetration height of the hydrogen, OH plume respectively, increases with rising pressure. The transverse signal distribution plots from which the OH plume penetration height is derived are shown in Figure 5.13 (a). From these plots a linear dependency of the penetration height over equivalence ratios can be derived (Figure 5.13 (b)).

It is also interesting to compare OH PLIF images obtained at each of the three plane po-

sitions investigated. Comparing first position 1 (middle of the duct) with position 2 (above injection port) it can clearly be seen that the OH penetrates into the free stream slightly more for the plane above the injector than for the mid duct plane. This is to be expected since the fuel is directly introduced there. Additionally, significant fluorescence is generated in the duct center plane between the injectors, indicating the presence of fuel/air mixing and combustion between the injection locations.

The OH signal becomes less intense with downstream distance, as can be seen by comparing Figures 5.14 (b) and (c) which were obtained in the same plane but at different axial locations. A noticeable increase in signal occurs in the vicinity of the impingement of the reflected shock wave. In Figure 5.14 (c) there is a very significant luminosity signal, with levels almost as high as the fluorescence signal. This supports the idea that the shock wave significantly enhances the combustion in the duct.

The variation in penetration height depending on the visualization plane for the highest hydrogen equivalence ratio is shown in Figure 5.15 (a). Figure 5.15 (b) is a plot of the penetration height against the equivalence ratio for position 1 (mid duct) and position 2 (above injector), clearly demonstrating the three-dimensionality of the flow field.

5.1.3.2 Ethylene Fuel and Comparison of Fuels

The general findings of the hydrogen experiments discussed in the previous sections are also mostly for the ethylene experiments at the lower equivalence ratio, therefore only obvious differences shall be discussed in more detail. The first images presented were obtained at position 2 (above injector port) for three different global equivalence ratios ($\Phi = 0.13$, $\Phi = 0.37$

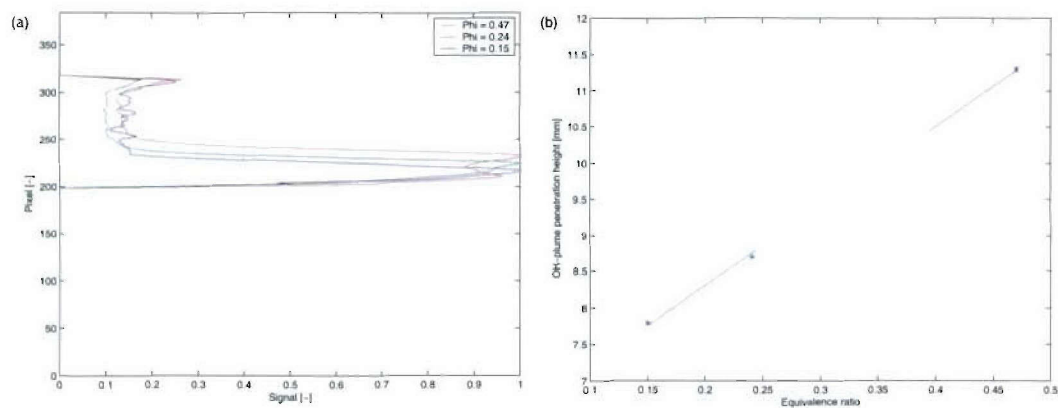


Figure 5.13: Penetration height of OH-plume (hydrogen above injection port);(a) shows the transversal PLIF signal distribution for three different equivalence ratios, (b) is a penetration height versus equivalence ratio plot.

and $\Phi = 0.64$). These PLIF images and the corresponding luminosity images are shown in Figure 5.16. Three major observations can be made: Firstly, the ignition point is shifted downstream in comparison to the hydrogen fuel conditions for all three ethylene equivalence ratio even though the equivalence ratios are equal or higher than for hydrogen. This effect is due to the longer ignition delay times for ethylene. It is interesting to compare the ignition delay time correlations of Colket and Spadaccini (2001) with the ethylene and hydrogen combustion images. If we assume the calculated free stream temperature and locally stoichiometric conditions in the shear layer, the ignition delay times are 3.1×10^{-6} and 9.8×10^{-6} s for hydrogen and ethylene respectively. The factor of three difference compares well with the difference in the downstream distances at which OH first appears in the shear layer, as can be seen from a comparison of the images in Appendix A. Furthermore, if we assume the calculated free stream velocity of 2880 m/s, the ignition delay distances become 9 and 28 mm downstream of the step. This compares very well with the measured distances of approximately 5 mm and 27 mm for

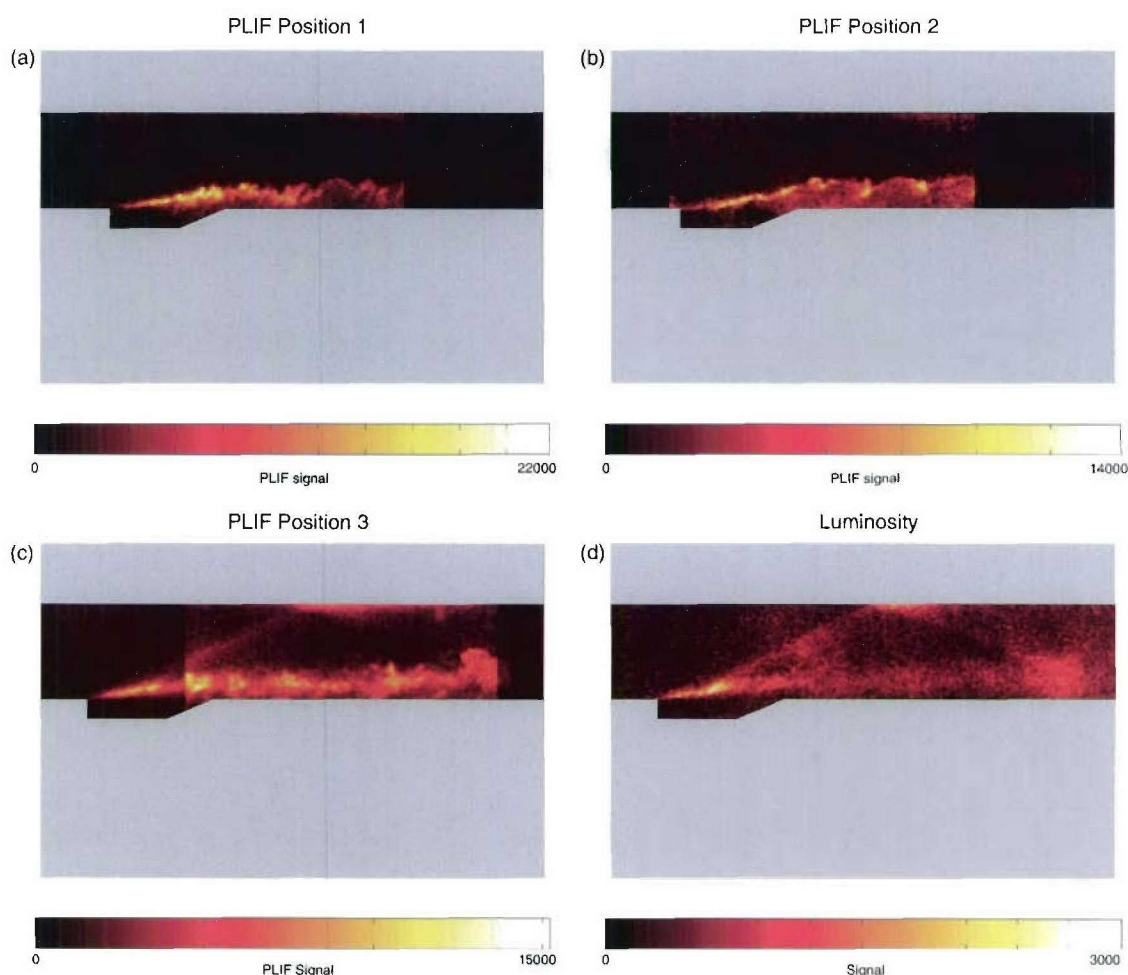


Figure 5.14: PLIF images at different laser sheet locations for hydrogen, $\Phi = 0.47$: (a) in the middle of the duct (position 1), (b) above injection port (position 2), (c) above injection port, downstream of the cavity (position 3), (d) luminosity image

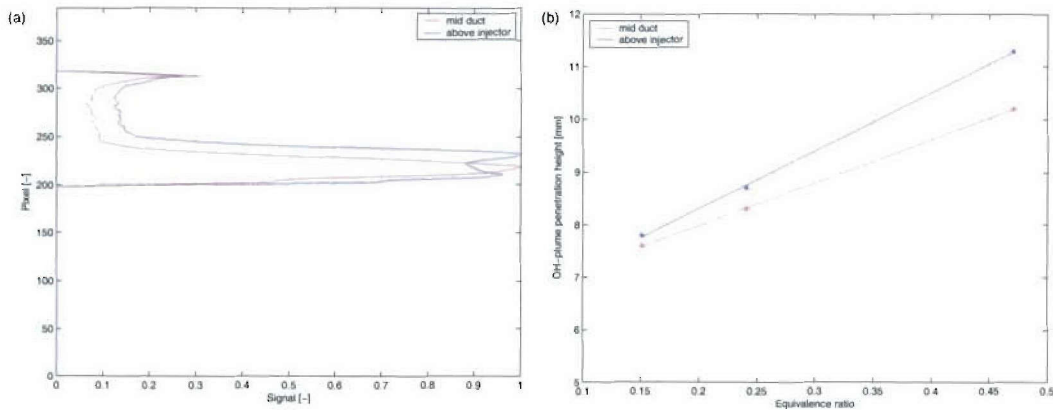


Figure 5.15: Penetration height depending on the visualization plane: (a) shows the graph for the planes above an injection port and in the middle of the duct (hydrogen, $\Phi = 0.47$), (b) is a penetration height versus equivalence ratio plot for both planes.

the OH PLIF images.

The second observation about the ethylene PLIF images is that the medium equivalence ratio (Figure 5.16 (b)) shows only small and nonuniform regions of OH fluorescence, with comparatively low signal. This behavior was verified by obtaining three images at the same conditions, all having similar low OH signals.

The final and most obvious difference occurs at the highest ethylene equivalence ratio. (Figure 5.16 (c)) shows a completely different combustion behavior with a very concentrated region of high OH concentration slightly above the injection port. The signal here was much higher than for the peak hydrogen combustion signal, although obtained at a much lower camera gain (5 for ethylene, 9 for hydrogen), in order not to saturate the camera's CCD sensor. Accounting for the different camera gains using Equation 4.5, the difference in peak signal is more than a factor of 30. The other two ethylene PLIF images, labeled (a) and (b) in Figure 5.16, were both acquired at a camera gain of 8, which is about 5 times more sensitive than camera gain 5 (compare Equation 4.5), resulting in signal counts of about 8000 for the medium Φ , and about 11000 for the low equivalence ratio.

The luminosity images confirm the previous observations. Low and inhomogeneous luminosity signal is captured for the medium equivalence ratio, whereas the luminosity image for the low ethylene equivalence ratio looks similar to the ones for the hydrogen experiments with the exception of the downstream shift of the ignition point, which again is observed for all three luminosity images. High luminosity signal is also observed for the high equivalence ratio but above the region towards the duct center where the huge OH signal is found. OH is an intermediate combustion product, which eventually reacts to form water during the combustion process. Therefore it is presumed that the OH is formed in the bright region of the PLIF image,

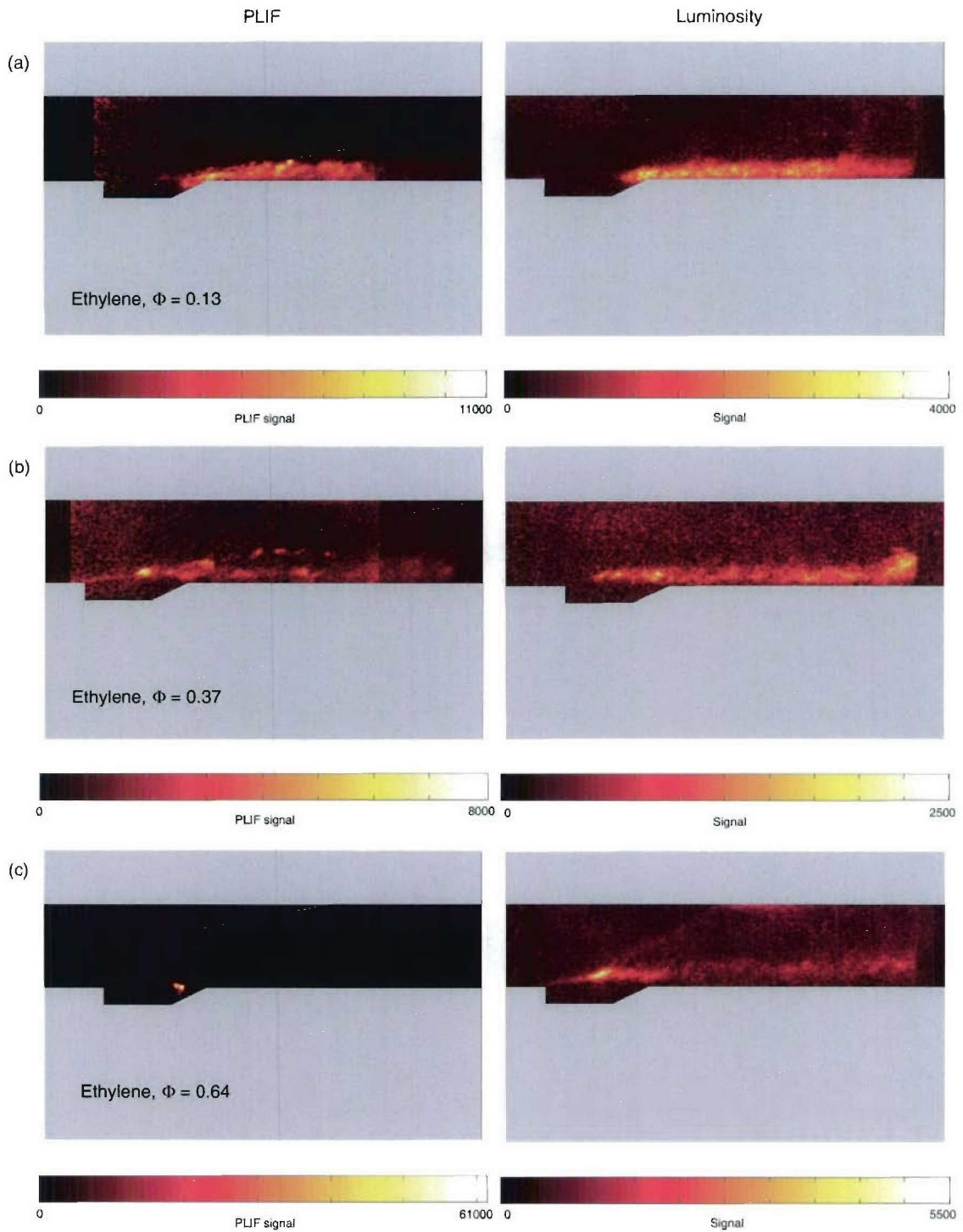


Figure 5.16: PLIF and luminosity images for three different ethylene equivalence ratios captured on a plane above an injection port: (a) $\Phi = 0.13$, (b) $\Phi = 0.37$, (c) $\Phi = 0.64$

and gets subsequently consumed by the combustion leading to a release of energy in form of heat in the region as illustrated in the luminosity image.

Unfortunately the shock structures cannot be seen as clearly for ethylene combustion as for hydrogen. Only for the highest ethylene pressure can shock structures be unequivocally made out. The shock angle found is about the same as for the highest hydrogen equivalence ratio (24°).

Pressure-ratio versus distance plots (during the 1.25–1.75 ms nominal test time) for the ethylene fuel conditions are presented in Figure 5.17. These plots reveal a similar behavior to that observed for the hydrogen conditions.

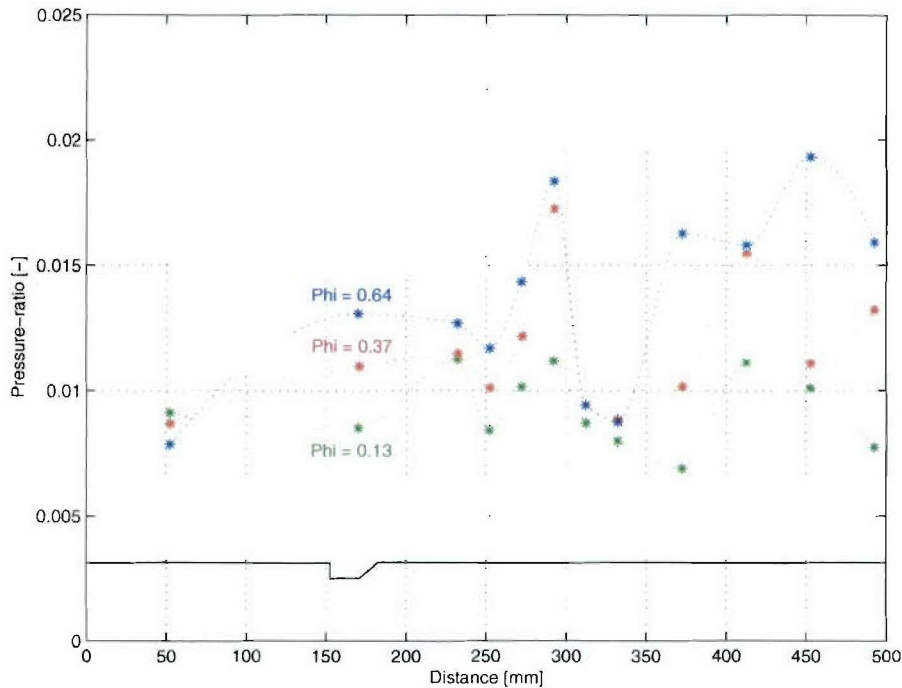


Figure 5.17: Pressure distributions for ethylene (test time 1.25 - 1.75ms).

Since the $\Phi = 0.37$ condition had not been tested in the initial pressure measurement campaign, an injection into nitrogen pressure measurement was made. The resulting pressure-ratio trace averaged over the test time is plotted against the distance together with the graph for the combustion case in Figure 5.18 showing a pressure rise for the latter, proving that combustion must have occurred. However the pressure rise due to combustion observed in the region investigated with PLIF measurements is relatively marginal, in agreement with the low PLIF observed for this equivalence ratio (see Figure 5.16). The reason for the low fluorescence signal at this equivalence ratio and the very large peak signal at the higher equivalence ratio currently remains unexplained.

The lower fuel volume fluxes of ethylene consequently lead to a (slightly) lower penetration height of the OH plume. The penetration heights for the two lowest equivalence ratios

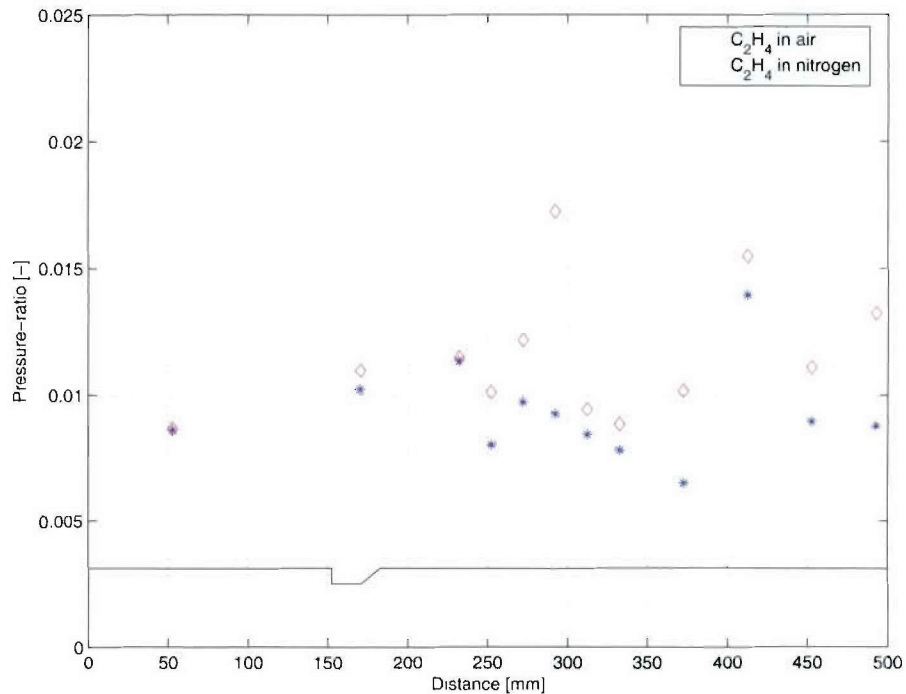


Figure 5.18: Pressure distributions for ethylene injection into air and nitrogen ($\Phi = 0.37$, test time 1.25 - 1.75 ms)

($\Phi = 0.15$ for hydrogen and $\Phi = 0.13$ for ethylene) are plotted in Figure 5.19 (a), whereas in (b) penetration heights of OH-plumes are plotted against equivalence ratios, both based on measurements at position 2. It is also assumed that the higher diffusion rates of hydrogen compared with ethylene lead to better mixing and hence to the greater OH plumes (higher penetration heights) observed for hydrogen.

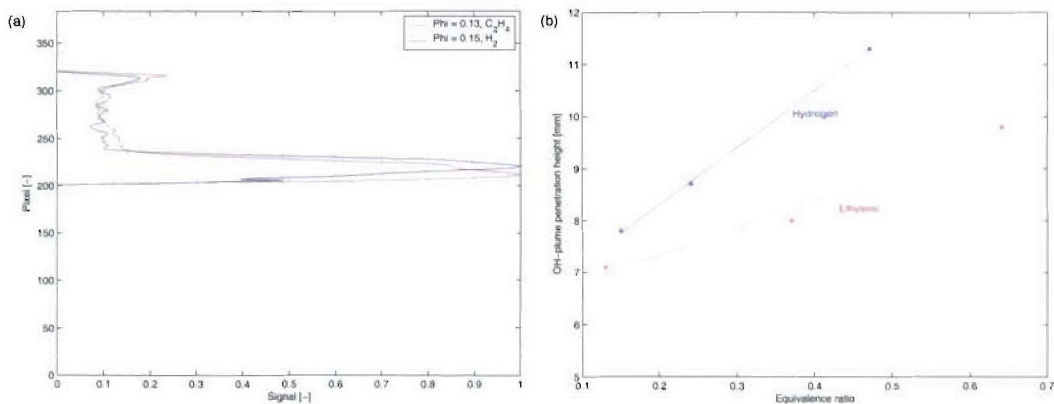


Figure 5.19: Comparison of penetration heights for different fuels and equivalence ratios for position 2: (a) Penetration height of hydrogen $\Phi = 0.15$ and ethylene $\Phi = 0.13$, (b) penetration heights versus equivalence ratio for both fuels.

The pressure-ratio comparison between hydrogen ($\Phi = 0.15$) and ethylene ($\Phi = 0.13$) is shown in Figure 5.20. Ethylene does not generate a remarkable pressure rise in/above the cavity, hence the pressure stays constant from the inlet to the cavity, besides the unresolved but relatively small variations due to shock waves and expansion fans in the shock train. The pressure distribution downstream of the cavity is quite similar for both fuels, except the greater pressure rise for hydrogen observed at transducer 10.

The development of the flow field further downstream in the duct is illustrated in Figure 5.21. For all three equivalence ratios observed images captured on both planes investigated (position 2 and 3, above an injection port about the cavity and downstream of the cavity) are presented.

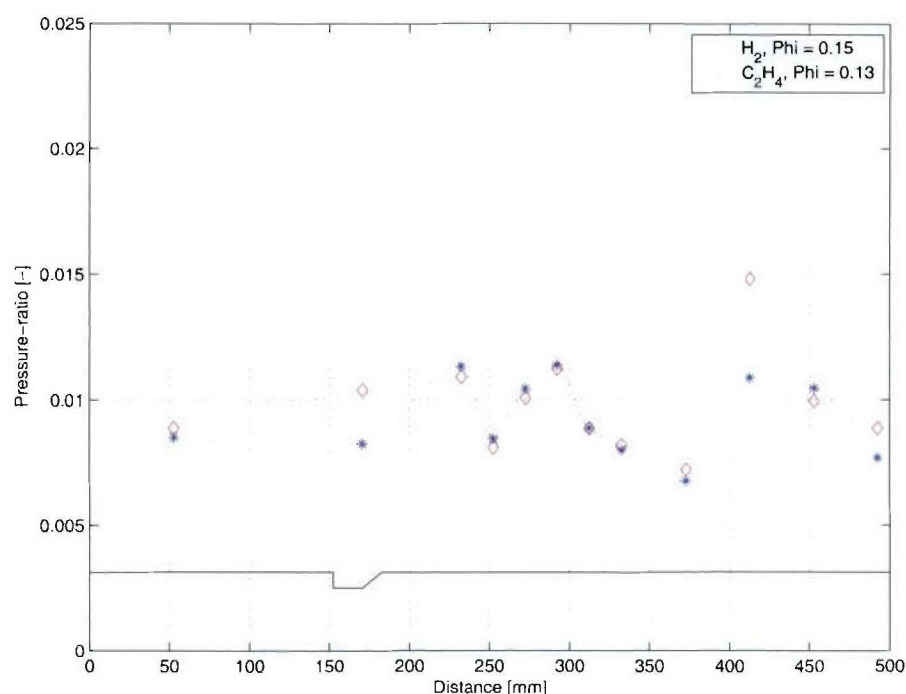


Figure 5.20: Pressure-ratio comparison of lowest equivalence ratios for hydrogen and ethylene (hydrogen $\Phi = 0.15$ and ethylene $\Phi = 0.13$)

Figure 5.21 (b) confirms the previous observations for the medium ethylene equivalence ratio, showing comparatively low OH PLIF signal all down the duct section imaged. It also shows another bright spot for the high Φ (c) around one cavity length downstream of the cavity trailing edge on the position 3 image. This bright spot is not observed on the plane spanning above the whole cavity (position 2), since the very high signal area dominates all lower signal regions. Except for the previously mentioned differences in OH distribution, the global flow field downstream the cavity is quite similar to the flow field observed for hydrogen injection.

A collection of all PLIF and luminosity images acquired during the experiments, including the ones obtained for preliminary studies, can be found in Appendix A.

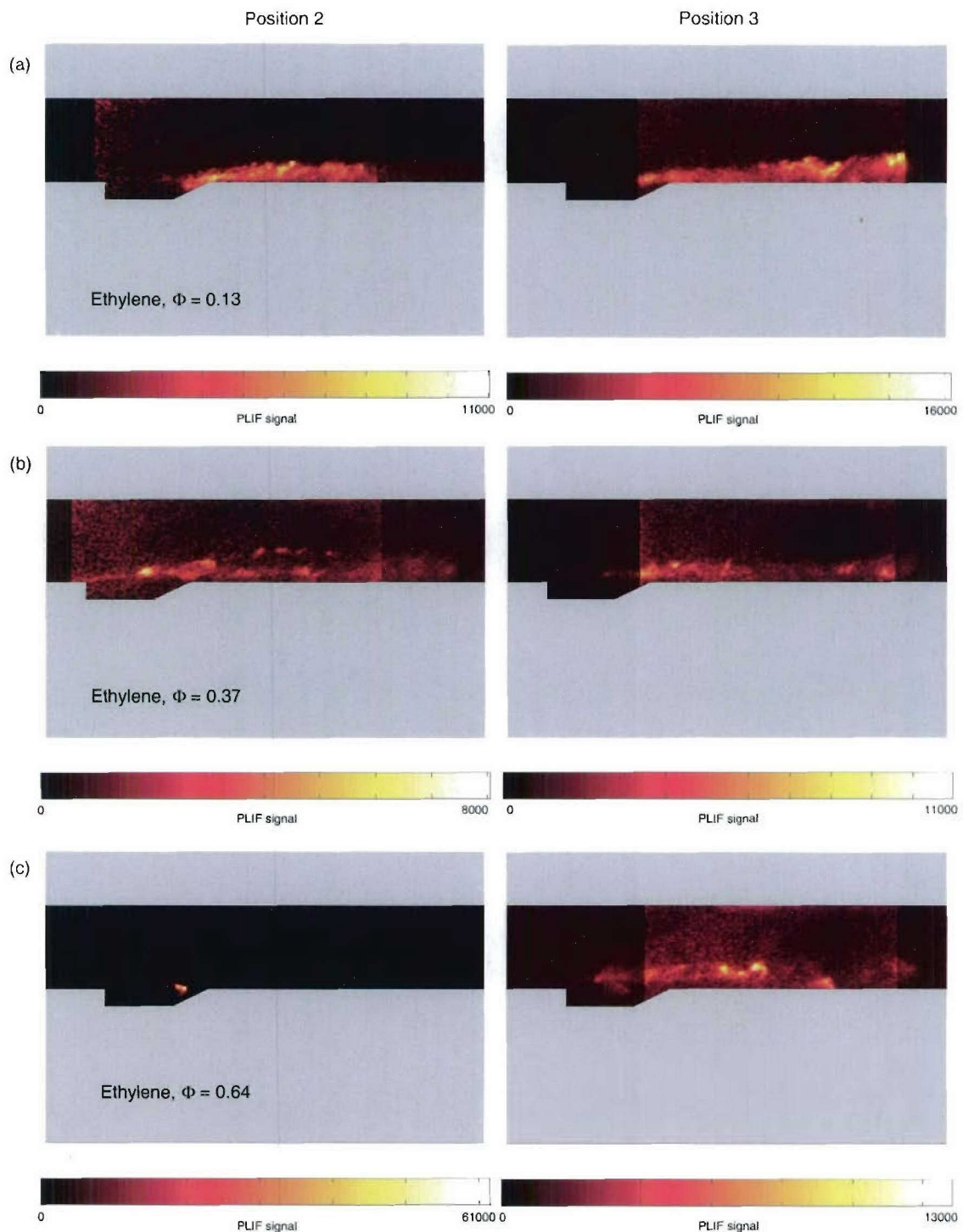


Figure 5.21: PLIF and luminosity images for three different ethylene equivalence ratios and two laser sheet locations, position 2 (left column) and position 3 (right column): (a) $\Phi = 0.13$, (b) $\Phi = 0.37$, (c) $\Phi = 0.64$

5.2 CFD Results

CFD calculations using the commercial code CFD++[®] have been performed and are presented below. As discussed earlier, the duct inlet conditions used for these calculations are erroneous, representing a higher Mach number and significantly lower static temperature than the inlet conditions of the experimental work. As a result, direct quantitative comparison between the experimental and numerical pressure distributions is not possible in any meaningful way, and such comparisons are therefore not presented here. On the other hand, the CFD results show useful qualitative trends that assist in understanding the general features of the experimental flow, and provide information that is not available from the experiments. Future work will include numerical studies at the correct inlet conditions.

The CFD simulations were performed at these inlet conditions: $p_\infty = 78.5$ kPa, $T_\infty = 1183$ K, $\rho_\infty = 0.231$ kg/m³, $u_\infty = 2802$ m/s and $M_\infty = 4.15$. Calculations were performed for the following three cases:

- nil-injection
- hydrogen injection into air - frozen reactions
- hydrogen injection into air - finite-rate reaction chemistry

whereby the two latter were performed at a simulated equivalence ratio of $\Phi = 0.47$. Hydrogen was chosen because of the relative simplicity of its combustion mechanism.

For all calculations, the maximum Eulerian norm residual of the energy, mass and x-, y- and z-momentum equations dropped about four orders of magnitude before they started to flatten out. For the simulation involving chemical reactions, some of the species mass continuity equations did not converge properly and started to flatten at about $10^{-3} - 5 \cdot 10^{-2}$, hence convergence was not completely achieved and the changes between iteration steps are not negligible. The probable reason for the flattening can be found in transient flow structures due to cavity oscillations. Thus the assumption of a quasi-steady flow is not completely accurate and a time-dependent simulation is very likely to solve these problems; a recommendation for future work. The flow is solved to second-order spatial accuracy using a multi species extension of Roe's approximate Riemann solver.

Despite the restrictions due to convergence not being completely achieved in all cells, the CFD solutions still give significant insight in the scramjet flow field and are very useful to understand certain phenomena. Especially the non-injection and frozen reaction simulations, which converged to about 10^{-4} and hence provide very reasonable results, and reliably show flow-structures and mixing capabilities of the model scramjet.

5.2.1 Basic Flow Structures

The intake region of the duct contains a series of weak oblique shock waves which form due to the growth of the boundary layer on the top, bottom and side walls. Each of these shock waves is followed by an expansion forming the diamond-shape shock train structure which can typically be observed for symmetric supersonic internal flow fields such as the ones in scramjet ducts. This can be clearly seen in Figure 5.22 which shows the pressure field in the duct center plane for the nil-injection case.

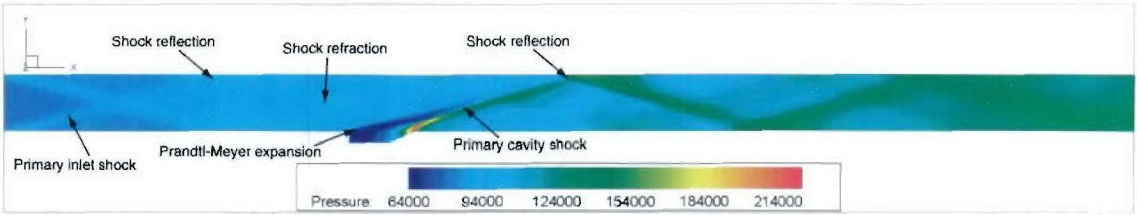


Figure 5.22: Pressure distribution on the center plane, non-injection

As the flow passes over the cavity it experiences a relaxation as the duct instantaneously expands and a Prandtl-Meyer expansion fan is formed for no injection. The shear layer which separates from the leading edge is diverted towards the cavity floor and reattaches at the slanted slanted rear ramp. This can better seen in the Mach number distribution as shown in Figure 5.23.

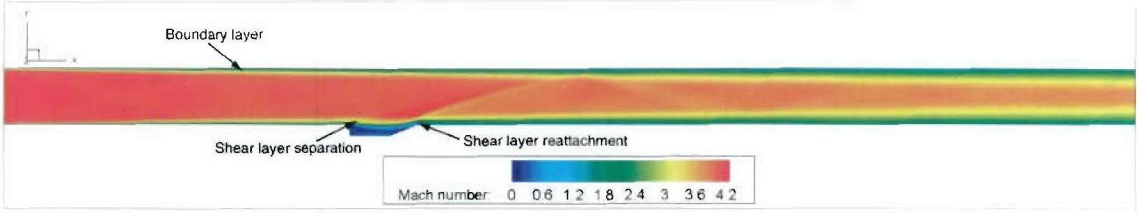


Figure 5.23: Mach number distribution on the center plane, non-injection

Since the shear layer does not reach and reattach at the bottom surface of the cavity the cavity is considered open (recall Section 2.2 where the cavity terminology is described). The reattachment/impingement of the shear layer is located at the region around the rear cavity corner where consequently the highest pressures exist. This causes another much stronger oblique shock wave to form, as can be seen on both the pressure and Mach number plots. This shock wave travels down the scramjet duct reflecting from the top and floor and interacting with the boundary layer. At the outflow the boundary layers are quite thick each consuming about 25% of the duct height.

The flow within the cavity can be studied best by plotting streamline traces as in Figure 5.24 (a). This indicates a clockwise rotating recirculation zone filling almost the complete span-width of the cavity. This recirculation zone is assumed to be the source of flame-stabilization and holding when fuel is injected and combustion is established.

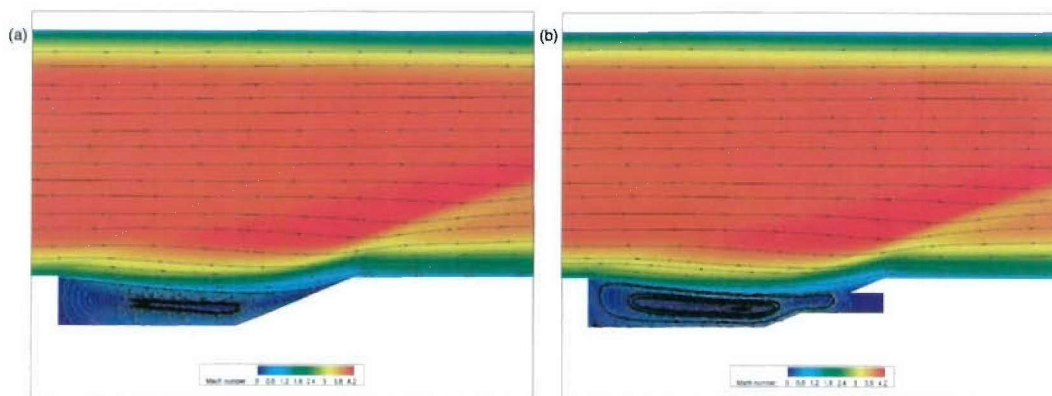


Figure 5.24: Mach number distribution and streamlines in and above the cavity, nil-injection: (a) on the center plane, (b) above an injection port

Figure 5.24 (b) which shows the Mach number field and streamlines captured on the plane above the injection port next to the centerline indicates an additional much smaller recirculation zone in the bottom left corner of the cavity.

5.2.2 Fuel/Air Mixing

A prerequisite for efficient combustion is a homogeneous and sufficient mixture of fuel and air. Introducing fuel into the cavity increases the pressure and provides an obstacle for the oncoming flow and hence causes an oblique shock wave to form from the cavity leading edge where previously the expansion fan was located (Figure 5.25). This effect causes the shock train in the cavity to move upstream involving stronger and therefore steeper shock waves. The incident shock wave has a slightly curved shape around the fuel "bubble" and straightens towards the top wall.

The alteration of the flow field within the cavity through fuel injection is shown in Figure 5.26. Streamlines are overlaid on the Mach number distribution of equal planes as presented in Figure 5.24 for the frozen reaction case. The plane above the injection port (b) indicates the formation of two counter rotating vortices which are assumed of greatly enhancing the mixing process of fuel and air.

To get a better impression of how well the hydrogen mixes with the air, Figure 5.27 shows

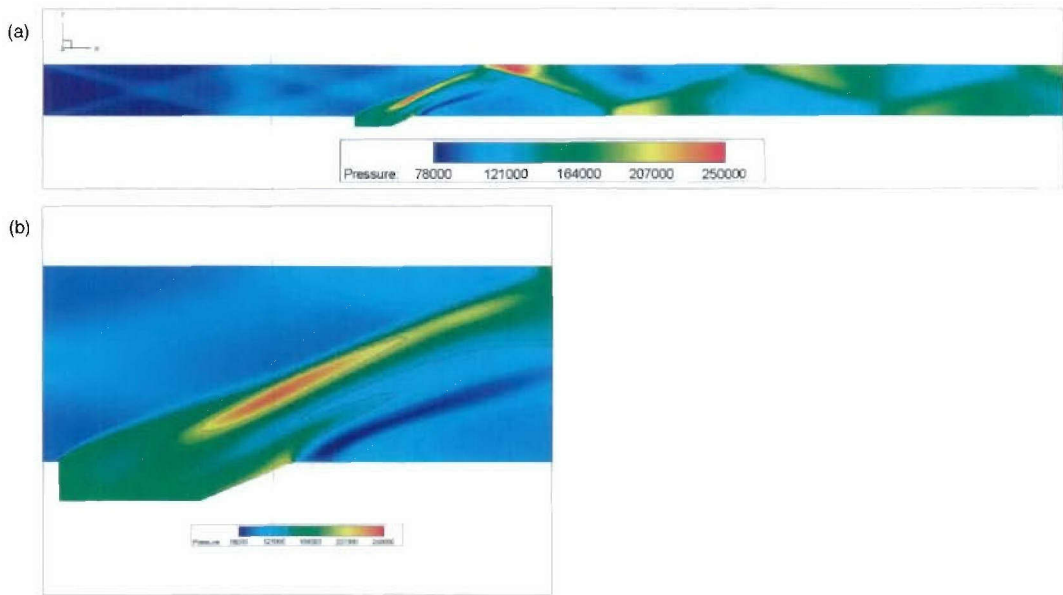


Figure 5.25: Pressure distribution in the scramjet duct on the center plane, fuel on, frozen reactions: (a) shows the whole duct, (b) shows a magnification of the sector incorporating the cavity, also including flood lines which clearly indicate the curved shape of the shock wave in the first segment.

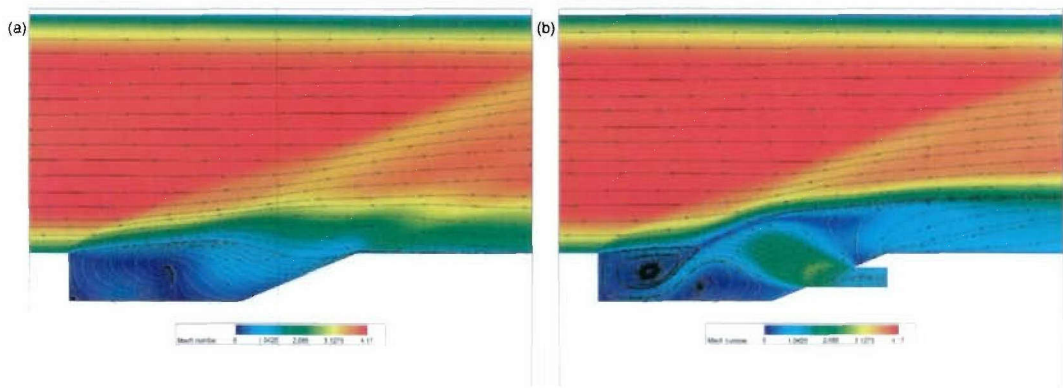


Figure 5.26: Mach number distribution and streamlines in and above the cavity, frozen reactions: (a) on the center plane, (b) above an injection port

plots of hydrogen mass fractions. Different hydrogen mass fraction and thus different local equivalence ratios are identified by the colored bands. The hydrogen distribution across the duct shows distinct bumps above the injectors and is significantly penetrating higher towards the sidewalls. These effects start to blur out as the flow travels further down the duct settling to a relatively constant level. A fairly broad band of fuel/air equivalence ratios between 0.5 and 1.5 can be observed, indicating that the fuel mixes sufficiently for combustion to occur in a reasonably large area.

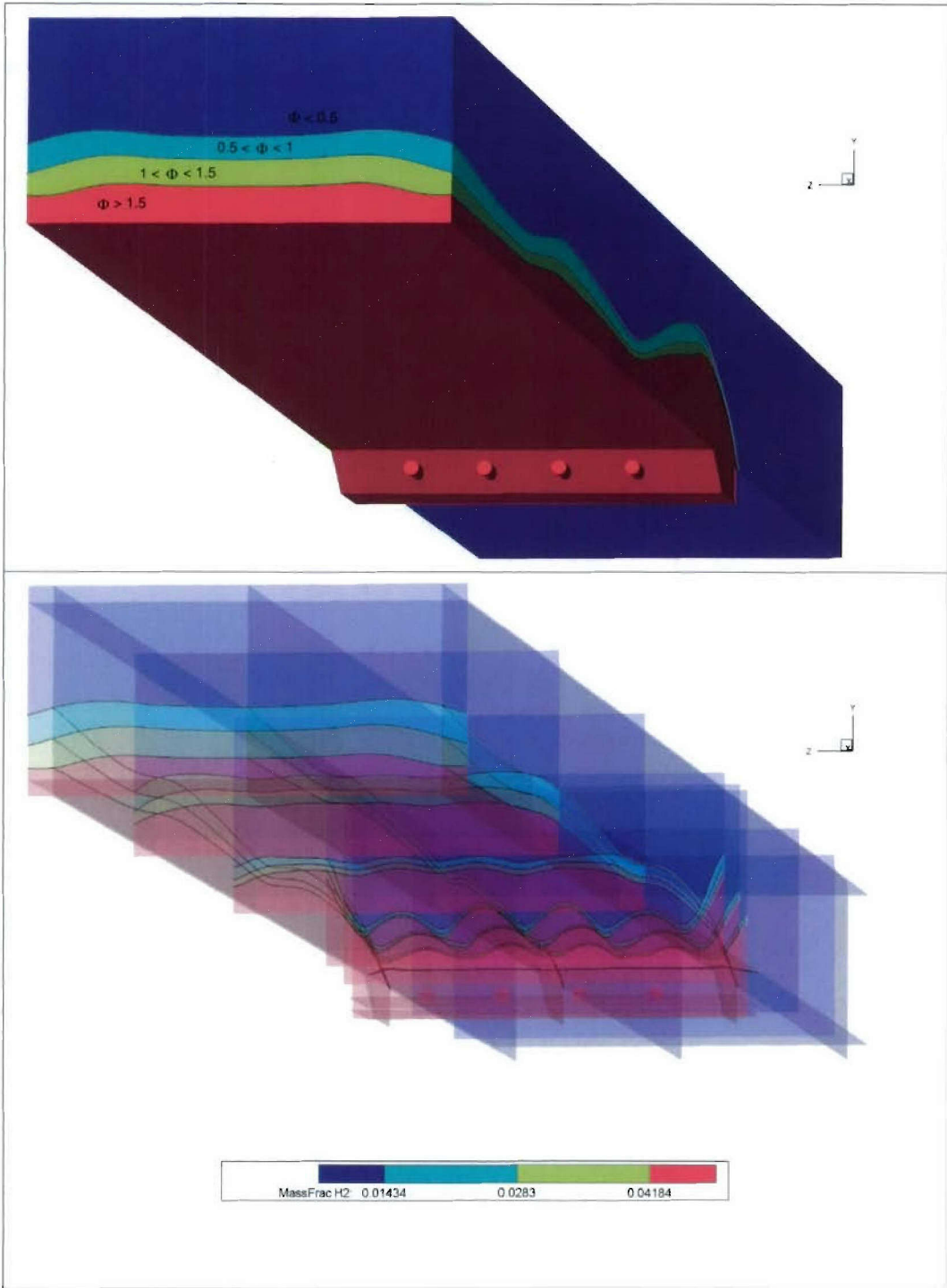


Figure 5.27: Mass fraction of hydrogen, frozen reactions: the colored bands indicate regions of different equivalence ratios

However it has also been shown that the fuel was unable to disperse through the whole duct at this equivalence ratio. Increasing the injection pressure could at least partially improve this situation. However increasing the injection pressure to much, can result in choking of the

scramjet and in a strong deceleration of the oncoming flow. Thus the amount of fuel injected has to be adjusted to the design of the duct maximizing and ensuring safe, stable and effective operation at the same time.

5.2.3 Combustion

After having provided evidence of decent fuel/air mixing the next logical step is to investigate the combustion process. A sensible way to do this is to trace combustion products, with water (H_2O) being the dominant product, and to compare pressure traces of the frozen reactions simulation with the finite-rate reactions case. Another important intermediate combustion species is the hydroxyl (OH) radical, the presence of which strongly indicates the ignition process and hence regions with high OH concentration show the location of the flame front. As CFD gives a fully 3D view of the flow field it is very useful for detecting areas where combustion is supposed to take place. The last step is to compare the computational results with the experimentally obtained data to provide the possibility of CFD code validation which in case of matching or similar results subsequently can be used for further simulations for which no experimental data exists.

Firstly images of calculated H_2O and OH distributions are presented. Different slices cutting through the flow field are plotted in Figure 5.28 showing the three-dimensional distribution of H_2O mole fractions.

The existence of H_2O in Figure 5.28 indicates a certain amount of combustion. Applying Equation 2.13 for hydrogen gives a *global* mole fraction of H_2O for a completed hydrogen/air-combustion process of about 0.35, whereas the *maximum* value in the CFD solution only is 0.028 which is more than an order of magnitude lower than the optimum. Thus the combustion process is far from completion and most of the injected fuel remains unburnt. The highest H_2O concentration can be observed at the outflow of the scramjet indicating increased combustion downstream in the scramjet duct. Another remarkable observation is the fact the essentially all of the water produced is in the vicinity of the sidewalls and virtually no water exist in the duct center. This phenomenon is presumed to be due to interactions between the walls and the free stream forming vortices which subsequently enhance the combustion process through increased production of radicals.

A similar plot to the one presented before but for OH is shown in Figure 5.29. The previously mentioned concentration peak close to the sidewalls can be observed for OH as well, although the area of high OH presence is shifted towards the top wall. Again only very low OH concentrations in the duct center are visible. Gruber et al. (2004) noticed a similar behavior in their OH PLIF experiments using a nominally similar scramjet geometry at a flight Mach number of 2, showing significantly higher OH PLIF signal in the vicinity of the sidewalls.

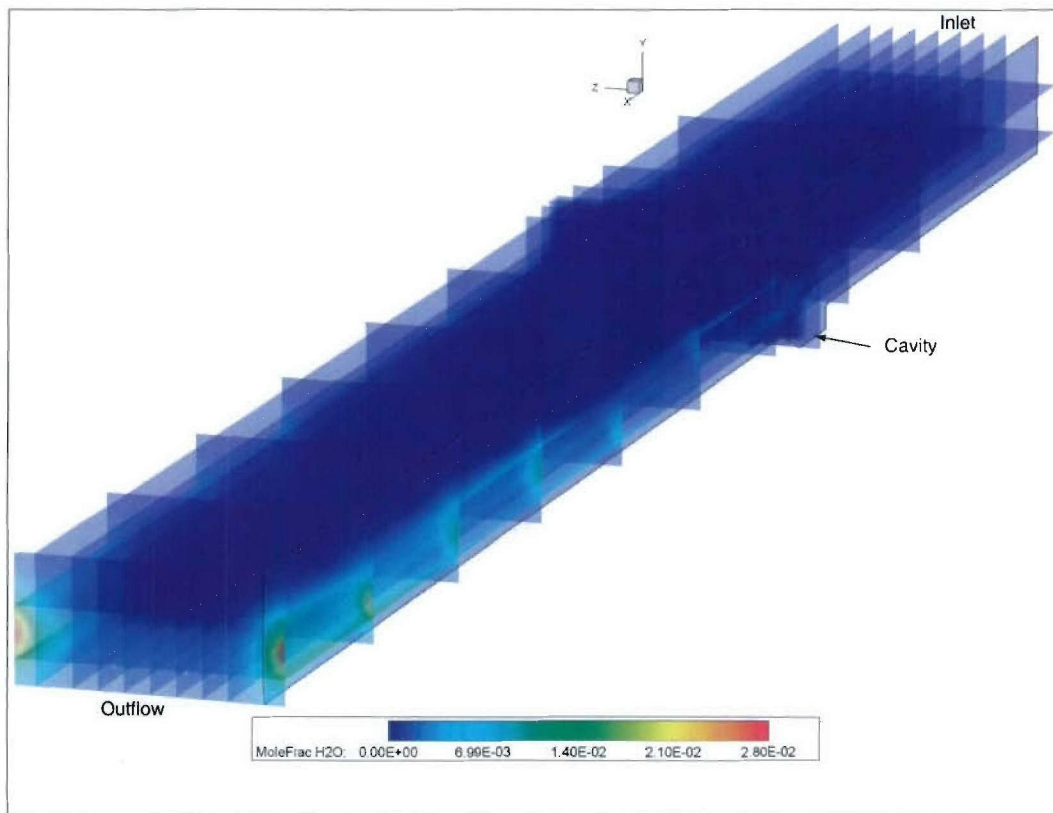


Figure 5.28: 3-dimensional plot of H₂O mole fraction, finite-rate reactions

5.2.4 Qualitative Comparison of Computation and Experiment

It is instructive to compare the experimental and computed flow structures in the vicinity of the cavity. Assuming that the fuel jets are modeled satisfactorily, discrepancies in shock angles in the air flow due to the fuel jet impingement depend only on the Mach number of the air. Figure 5.30 shows a luminosity image clearly indicating the angle of the incident shock wave (labeled "Experimental shock"). The CFD solution of the pressure field is overlaid, showing that the shock wave (labeled "CFD shock") has a less steep deflection angle, denoting that the Mach number has to be higher than for the experimental case, the static pressure lower respectively. This result is one of the reasons that led to the realization that the original calculation of the free stream conditions was erroneous.

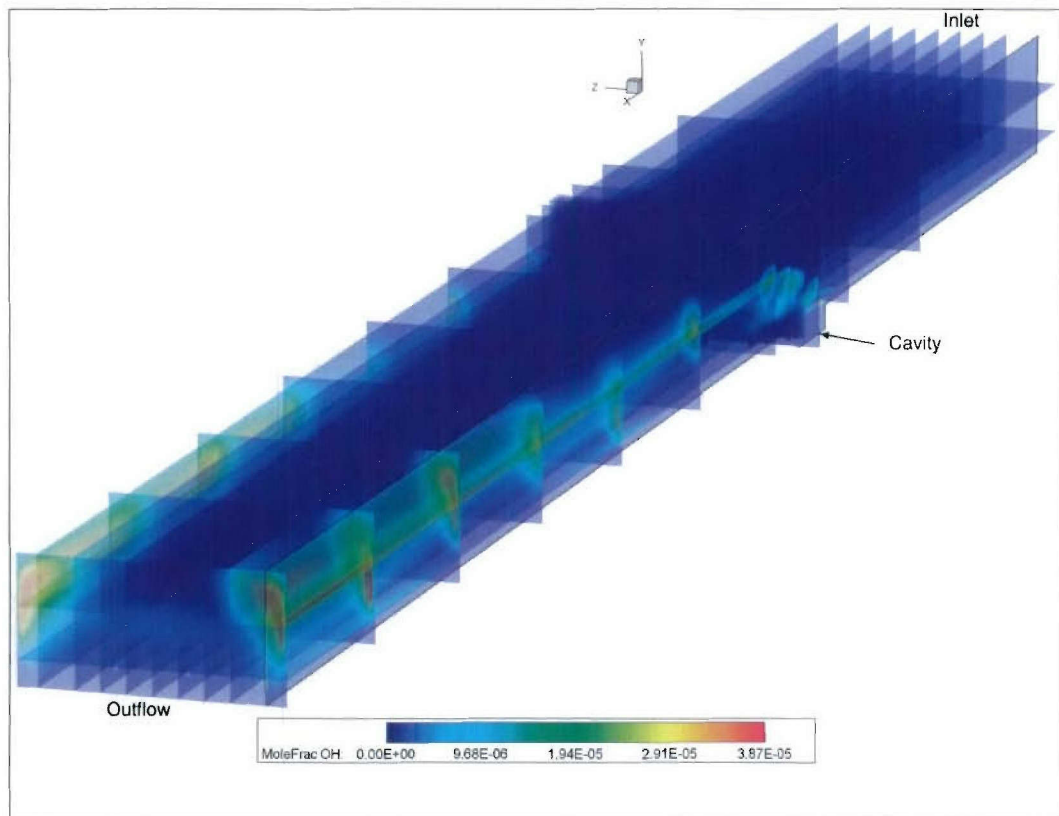


Figure 5.29: 3-dimensional plot of OH mole fraction, finite-rate reactions

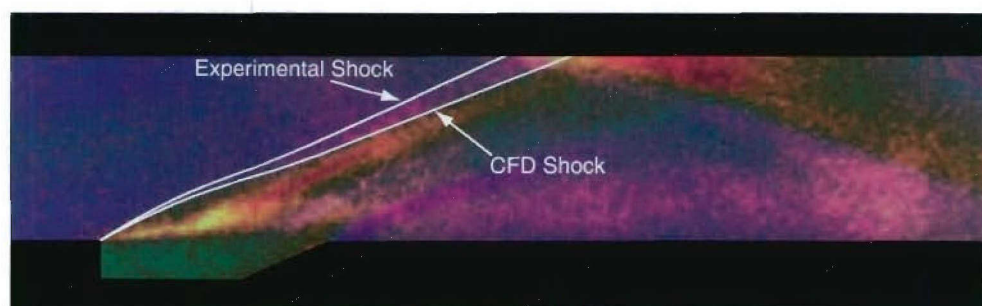


Figure 5.30: Overlay of luminosity image and computational pressure distribution, identifying shock locations and angles

Chapter 6

Conclusions and Recommendations for Future Work

The aim of this study was to investigate the behavior of a model cavity flame-holder scramjet combustor over a range of equivalence ratios for hydrogen and ethylene fuels at hypersonic Mach numbers to increase our understanding of the influence of the cavity in the mixing, ignition and combustion processes.

The experiments were conducted in the T3 free-piston-driven shock tunnel at the Australian National University. The facility was used to generate a Mach 4 semi-direct connect scramjet combustor flow field simulating a flight Mach number of 11.5 and an altitude of 29 km which corresponds to a stagnation enthalpy of approximately 6 MJ/kg. The geometry of the cavity investigated nominally matched that used in experiments conducted at the Wright-Patterson Air Force Research Laboratories in the flight Mach number range of 4–6. Both cavities had a rear ramp angle of 22, with an L/D ratio of 4.8. Fuel was injected upstream from the inclined rear face of the cavity at a range of equivalence ratios of injected hydrogen ($\phi = ?? - ??$) and ethylene ($\phi = ?? - ??$).

Axial pressures distributions were measured along the the centerline of the duct floor to map the pressure rise due to heat release resulting from combustion. Planar laser-induced fluorescence was used to measure the level of OH radicals in the vicinity of the cavity and immediately downstream. These visualizations, in conjunction with flow luminosity imaging (Chemiluminescence), were used to help determine the location of the flame-front and thus indicate where ignition and combustion occurred. Finally CFD calculations using the commercial code CFD++[®] were performed in an attempt to numerically predict flow structures and combustion in the scramjet combustor.

6.1 Experiments

The experiments showed that ignition could be induced and combustion sustained at hypersonic Mach number in a scramjet duct incorporating a cavity fuel injection system without an external means of ignition.

The wall pressure measurements indicated that for the duct flow conditions tested, combustion was initiated and maintained for an appreciable length of duct in all fuel-into-air runs. Combustion was observed in the cavity by PLIF and luminosity and as a combustion pressure rise at the floor. The pressure data suggests that the combustion immediately downstream of the cavity was quenched, possibly by an expansion and then re-ignited by the impingement of an oblique shock reflecting downstream from the cavity. PLIF and flow luminosity images support this conclusion, at least for some of the injection conditions. This process of quenching and re-ignition was apparent along the floor centerline of the duct as the structure of alternating shock waves and expansions reflects downstream. Ignition lengths could not be resolved within the spatial resolution of the pressure instrumentation but were apparent from the PLIF images in the shear layer above the cavity. Ignition delay times were calculated assuming the nominal free stream conditions and using the empirical correlations of Colket and Spaddaccini (2001). The calculated values compared well with the measured difference in ignition delay distance between the two fuels.

No OH was observed within the cavity. Rather, significant levels of OH were observed above the cavity (and downstream of it) in the region indicated by the CFD calculations to be approximately the stoichiometric shear layer between the air and fuel. Empirical ignition delay calculations are consistent with the streamwise location of the initial appearance of OH - in other words, that ignition is occurring due to shock-induced combustion ABOVE the cavity.

The PLIF images clearly showed the presence of OH above and downstream of the cavity for all conditions examined. For hydrogen fuel, the OH distribution looked similar for all three equivalence ratios tested. Increased equivalence ratios led to an upstream shift of the ignition point and to an increased OH/fuel penetration height. The two lower ethylene equivalence ratios demonstrated a similar behavior in terms of OH distribution, although the medium equivalence ratios showed significantly lower OH PLIF signal. In contrast an unique behavior was observed for the highest ethylene equivalence ratio. The fuel appeared to ignite and combust in a different manner leading to a markedly different OH distribution. Instead of the quite homogeneous OH plume observed for the other conditions a concentrated region with significantly higher OH PLIF signal was recorded.

A linear dependency on the equivalence ratio of the OH plume penetration height was derived for both fuels, also revealing the 3-dimensionality of the flow field as the penetration height changed across the duct. Turbulent flow structures in the supersonic flow were observed,

as well as the oblique shock waves forming due to the geometry of the cavity and the injected fuel.

The geometry of the cavity generates a train of oblique shocks and expansions that extend downstream in the duct. In the absence of fuel injection, pressure measurements and CFD indicate the shock originates at the impingement of the cavity shear layer on the inclined rear step. This oblique shock train moves upstream when mass is injected into the cavity producing a blockage to the flow in the duct. The shock structure moves further upstream again when combustion occurs increasing the initial shock angle and strengthening the compression. The angles of these shocks steepened as the equivalence ratio was increased by injecting more fuel.

As anticipated, increasing the global equivalence ratio increased the net pressure rise in the duct due to combustion. Interestingly though, this pressure rise was observed to be higher for ethylene than for hydrogen at comparable equivalence ratios. It is hard to conclude the mechanism for this without further data detailing the flow field and the combustion processes in the duct but is likely to be due to better mixing of the ethylene into the air flow.

6.2 CFD

CFD simulations were performed, although at significantly different inlet conditions to the experiments. These simulations were performed for three different cases at the highest hydrogen equivalence ratio:

- nil-injection
- hydrogen injection into air - frozen reactions (simulating fuel injection into nitrogen in the experiments)
- hydrogen injection into air - finite-rate reaction chemistry

Although the use of a colder free stream resulted in significantly reduced combustion when compared with experiment, these simulations have been included because they provide useful insight into the general flow structure and mixing processes in the combustor.

The nil-injection case was used to study basic cavity flow structures. A weak shock system was observed forming on the inlet and traveling along the scramjet duct. As the flow passes the cavity, an expansion fan forms at the cavity leading edge, followed by a strong oblique shock wave at the trailing edge. Inside the cavity a recirculation zone forms. The mixing of fuel and air was observed for the hydrogen injection case assuming frozen chemistry. The additional mass in the cavity provides an obstacle for the oncoming flow, hence the shock previously

forming at the inclined rear wall moves upstream, forming at the leading edge of the cavity. Plots of local equivalence ratio show that the fuel mixes well with the air above the cavity, providing sufficient conditions for combustion. Including chemical reactions however did not lead to significant combustion because of the lower free stream temperature when compared with the experiments. These simulations suggest that self-ignited combustion is marginal at lower enthalpy conditions than those used in the experiments. Therefore external ignitions sources may be required for flows at lower flight Mach numbers. The computations also highlight the three-dimensionality of the cavity flow field.

Interestingly, CFD predicted the highest level of combustion for these conditions in the vicinity of the sidewalls downstream of the cavity. This is an important observation since neither the PLIF images nor the pressure measurements were obtained in those regions. The shock locations were in reasonable agreement with the experiments, although as one would expect, the shock angles were slightly lower. This finding is consistent with the experimental observations of Gruber et al. (2004).

In summary:

- Cavity fuel injection is capable of producing stable supersonic combustion at flight Mach numbers in excess of 10.
- On the other hand, at such high flight Mach numbers the concept of flameholding, important to scramjet cavity technology for low hypersonic flight regimes, is not relevant. The combustion remains supersonic, and the flame location is fixed by chemical reaction rates at the local flow conditions (which in the present case are the conditions in the stoichiometric mixing layer above the cavity) and by the location of the combustion inducing shocks.
- At these flight Mach numbers, the cavity was initially expected to operate as a radical production zone (a radical farm) rather than as a flameholder. Since at the present conditions no OH is observed within the cavity, it is concluded that the cavity itself is NOT behaving as a radical farm at these conditions. Instead, at these conditions the cavity is the source of fuel and the means of generating the shock that induces combustion. The cavity feeds the shear layer above it, and it is the flame within this shear layer that may act as a source of radicals to assist further combustion downstream.

6.3 Proposal for Further Research

The experiments and analysis performed in this research program, while answering a number of fundamental questions about the viability of cavity-based combustion at a flight Mach number

in excess of 10, have highlighted a number of important areas where further investigation is desirable. These include:

- lowering the flight Mach number (total enthalpy) and simultaneously the cavity injection rate, to seek conditions at which fuel/air mixing and ignition can occur within the cavity (thus producing the radical farm effect) rather than in the shear layer above it. At these low flight Mach numbers radical farm behavior is needed because shock-induced reaction rates are significantly slower. This may also require additional fuel injection upstream of the cavity, after Gruber et al. (2001). Of interest would be a systematic investigation of the levels of cavity fuel required to sustain such scramjet operation, as suggested by AFRL.
- investigating the influence of the cavity on the net performance of the scramjet. While the experiments confirmed the presence of combustion in the duct incorporating the cavity, it was not clear to what extent the cavity was contributing to the combustion process and to what extent the inevitable drag that results from its presence negates any thrust gains from improved combustion. It is proposed to investigate these effects in two ways. Firstly, the drag resulting from the presence of the cavity can be indirectly measured from the distributions of pressure on the front and rear faces of the cavity. This could be achieved via the use of piezo-electric film to measure the net pressure level on each face. Additionally, the net thrust resulting from the difference between the combustion induced thrust and the internal drag could be measured by mounting a simple scramjet configuration, incorporating a thrust surface, onto a one-dimensional force balance. Combustion experiments would be performed with and without a cavity.

Additionally, a pitot rake would be used to survey the flow at the scramjet exit plane. This allows approximate calculations of the change in momentum thrust through the scramjet, for the range of equivalence ratios of interest, with and without the cavity.

- investigating the distribution of combustion pressure rise in the scramjet duct at higher spatial resolution. It is proposed to increase the very limited spatial distribution of pressure data along the duct floor in further testing by increasing the number of pressure tapings along the centerline and adding tapings off centerline. This would help to more accurately determine the movement of the shock structure downstream of the cavity under the various injection conditions and investigate the three-dimensionality of the flow field. Additionally, pressure tapings would be introduced on the front and rear faces of the cavity to measure the differential pressure across the cavity.
- investigating the distribution of combustion across the scramjet duct. The investigation has highlighted the anticipated three-dimensionality of the flow field in the duct which significantly impacts the mixing and combustion processes. Of particular interest is the predicted enhancement of combustion in the corner flows downstream of the cavity. This

phenomenon could be easily investigated and quantified by performing PLIF visualizations which use a horizontal laser sheet at varying heights above the floor. These measurements, in conjunction with further numerical simulations, would help determine whether this enhancement is due to better mixing of fuel and air in these regions or to increased reaction rates caused by increases in pressure and temperature.

- performing fast-Fourier transformations of the longitudinal OH signal distribution plots in conjunction with direct measurements of velocity to identify the cavity oscillation frequencies.
- extending the OH PLIF visualizations further downstream, to observe the combustion process in the main part of the duct where the bulk of the combustion pressure rise occurs.
- performing NO PLIF to investigate the flow structure in the presence of gross three-dimensionality in the flow. This could be performed in tandem with Schlieren imaging, possibly employing UNSW@ADFA's new focused-Schlieren capabilities to better resolve three-dimensional features.
- employing TDLAS (Tunable Diode Laser Absorption Spectroscopy) to measure (integrated) concentrations of water vapor downstream of the combustion to identify the extent of the combustion plume.
- expanding the investigation to higher equivalence ratios. These initial experiments were performed at fuel-lean global equivalence ratios due to the limitations of the fuel injection system. This fuel injection system is currently being upgraded and it is proposed to extend all of the experiments to higher equivalence ratios.
- employing surrogate fuel mixtures, which simulate cracked endothermic fuel products to more accurately represent the combustion of hydrocarbon fuels.
- investigating the dependence of combustion performance on cavity geometry and injection location and direction. This collected data could form the basis of a geometry-optimization investigation using Multi-Disciplinary Optimization (MDO) techniques.
- performing transient computations to capture the unsteady nature of the cavity flow field.
- implementing more detailed chemistry models for use in the computations.

Acknowledgements

This work was completed with help and advice from several people, and the authors would like to take this opportunity to thank them.

Mr Paul Walsh ran the facility for the tests, constructed the cavity model and contributed a great deal of technical expertise that was essential to the success of the project.

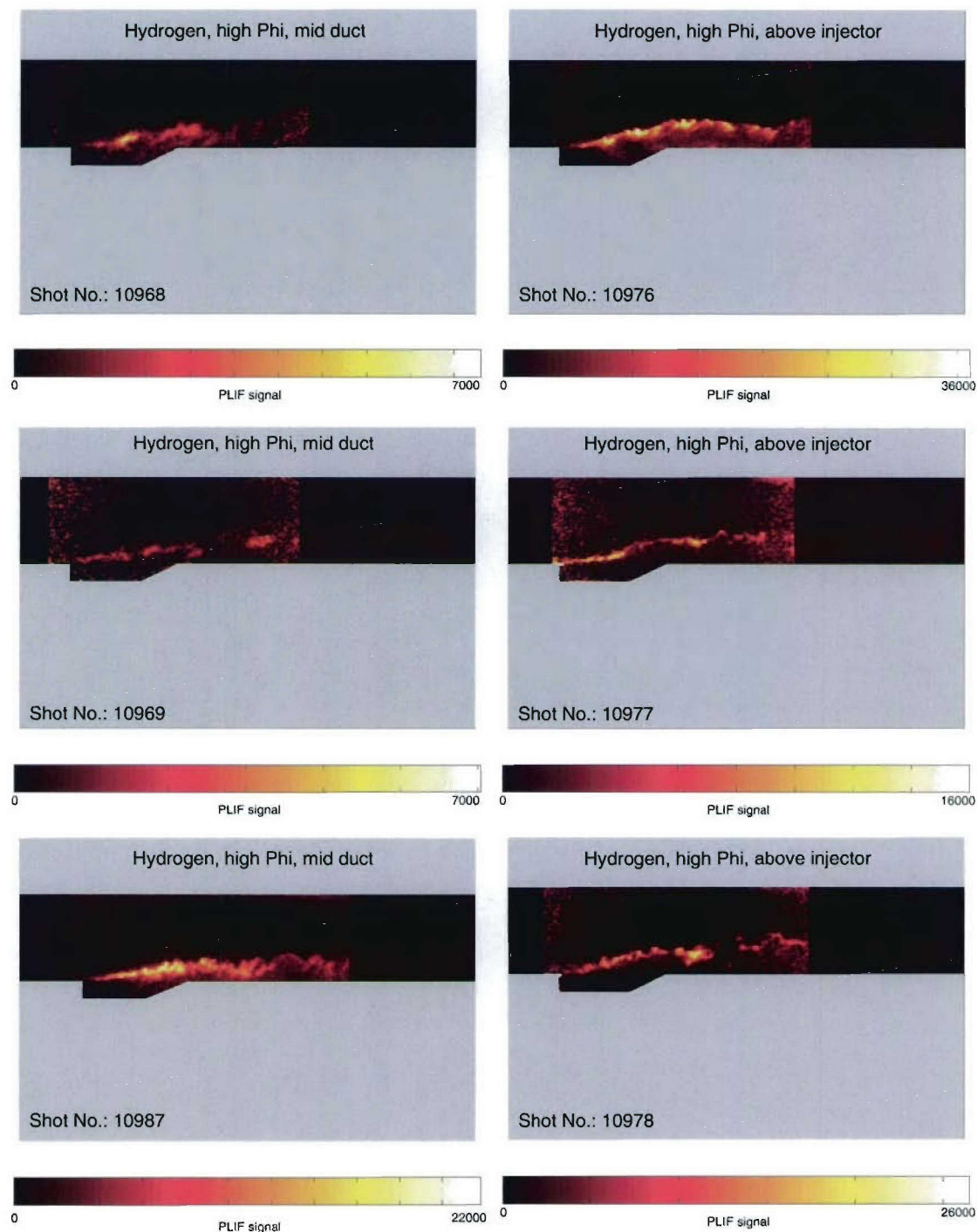
Dr Julie Reppel initiated the re-construction of the OH PLIF system used for these experiments. Mr Jeff M^cGuire helped with several of the PLIF experiments and calibrations of the laser system.

Mr Ingo Stotz worked on these experiments as partial fulfilment of his Diplomarbeit studies at the Lehrstuhl für Flugantriebe, at the Technische Universität München, and the authors thank that institution for providing an excellent student for this project.

Appendix A

PLIF and Luminosity Images

This appendix collects all PLIF and luminosity images acquired during the experiments some obtained for preliminary studies, such as transition variations or laser sheet adjustments. Each figure contains a series of images captured at equal fuel conditions (equivalence ratios).

Figure A.1: Hydrogen, high equivalence ratio ($\Phi = 0.47$)

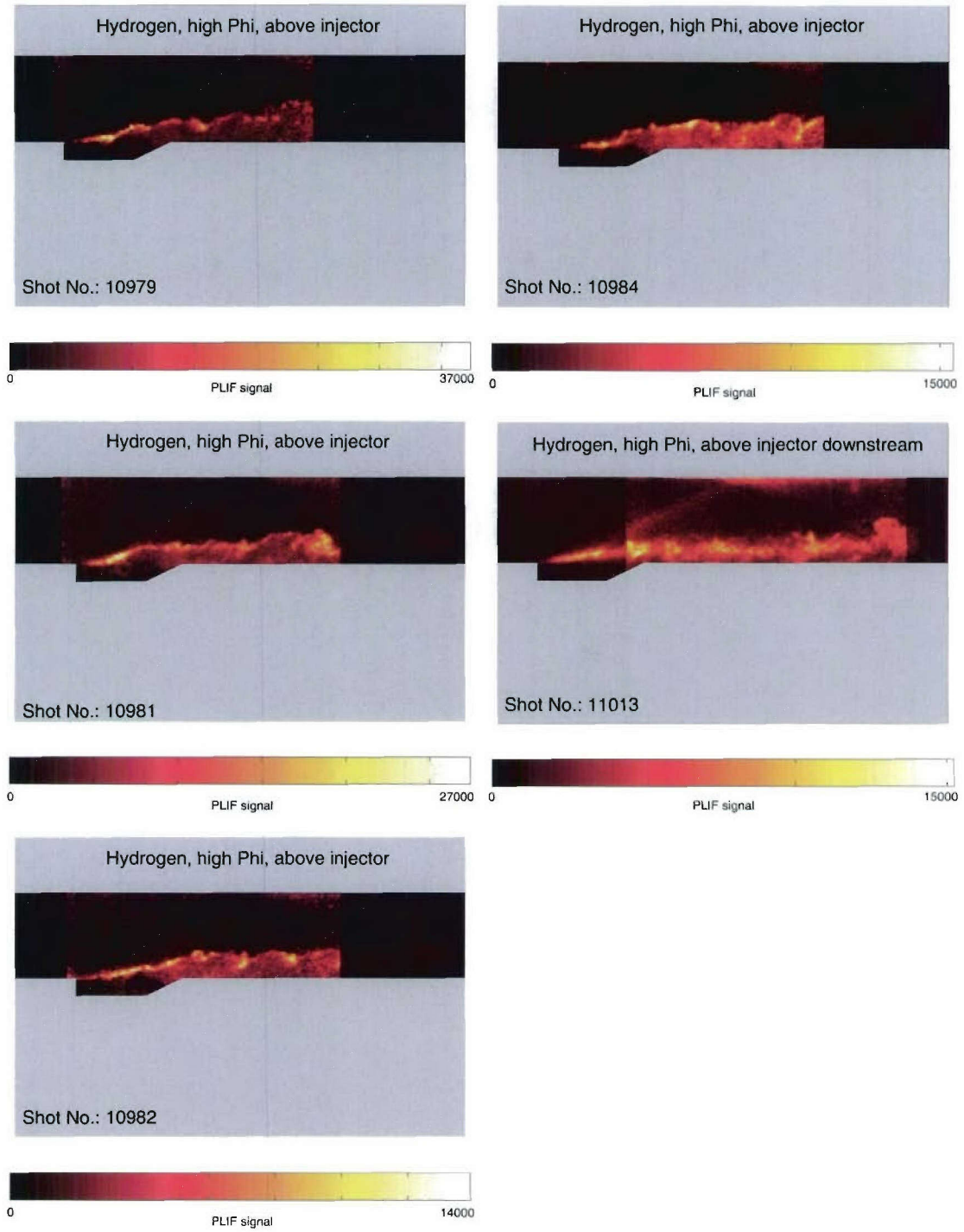


Figure A.2: Hydrogen, high equivalence ratio ($\Phi = 0.47$)

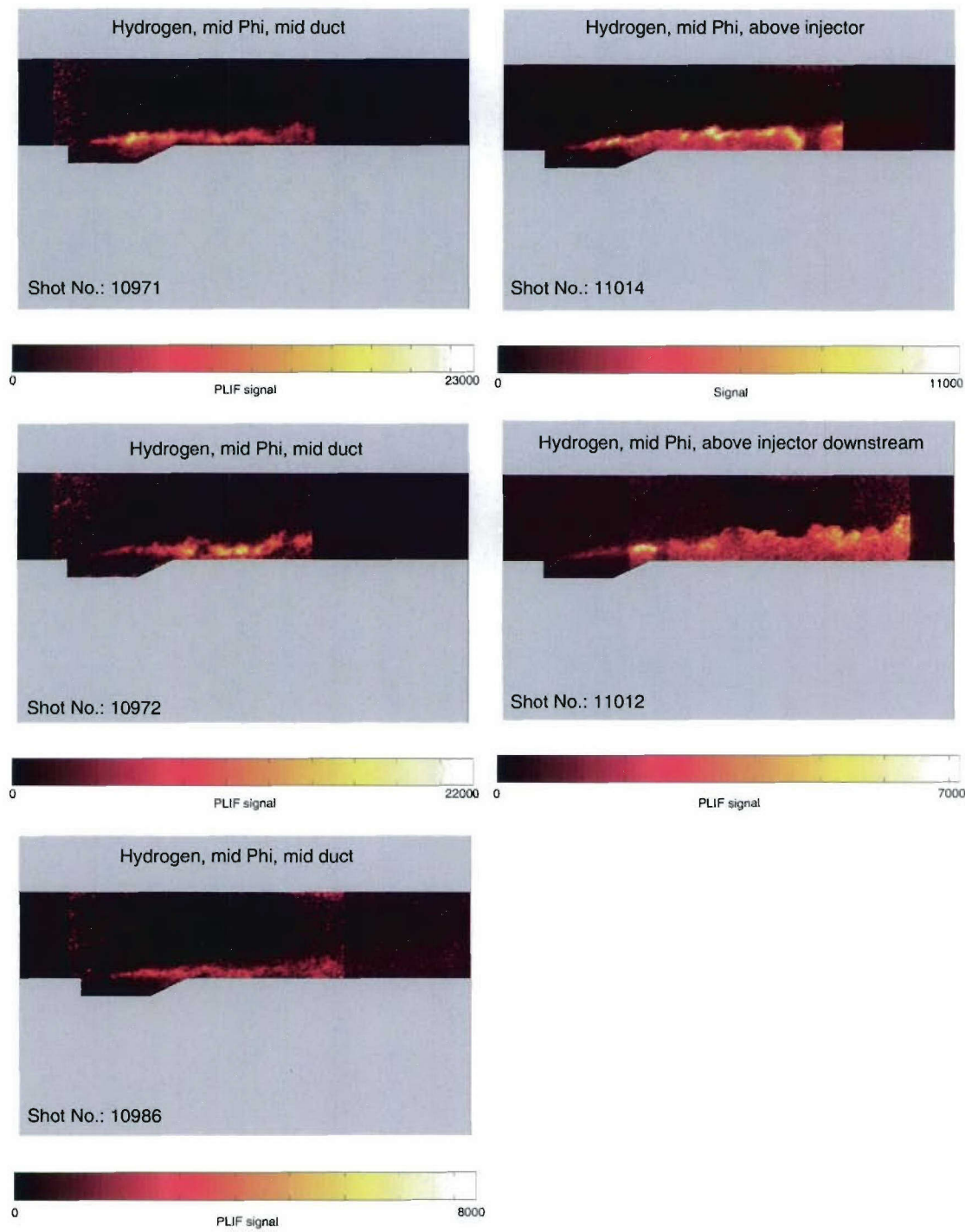


Figure A.3: Hydrogen, medium equivalence ratio ($\Phi = 0.24$)

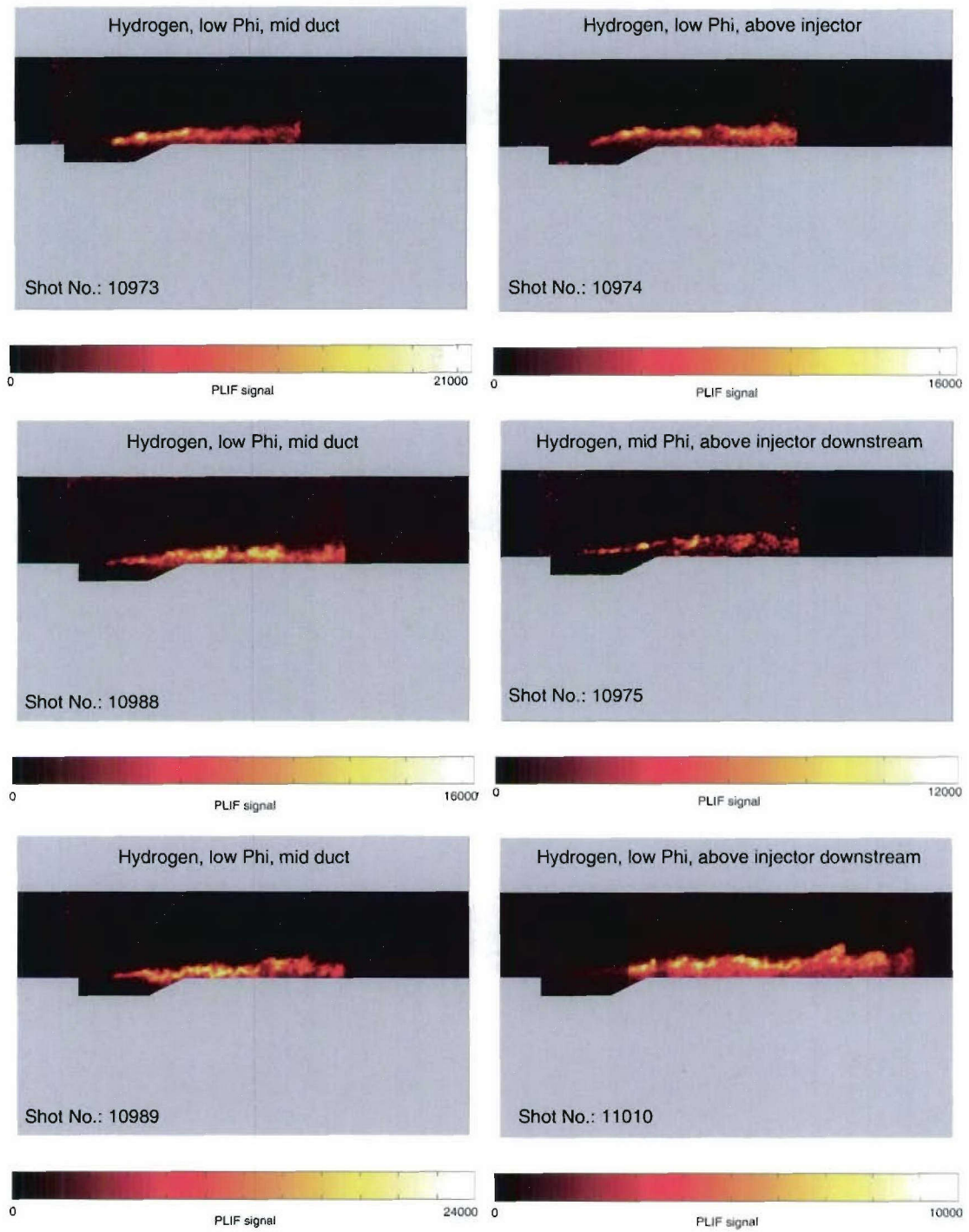


Figure A.4: Hydrogen, low equivalence ratio ($\Phi = 0.15$)

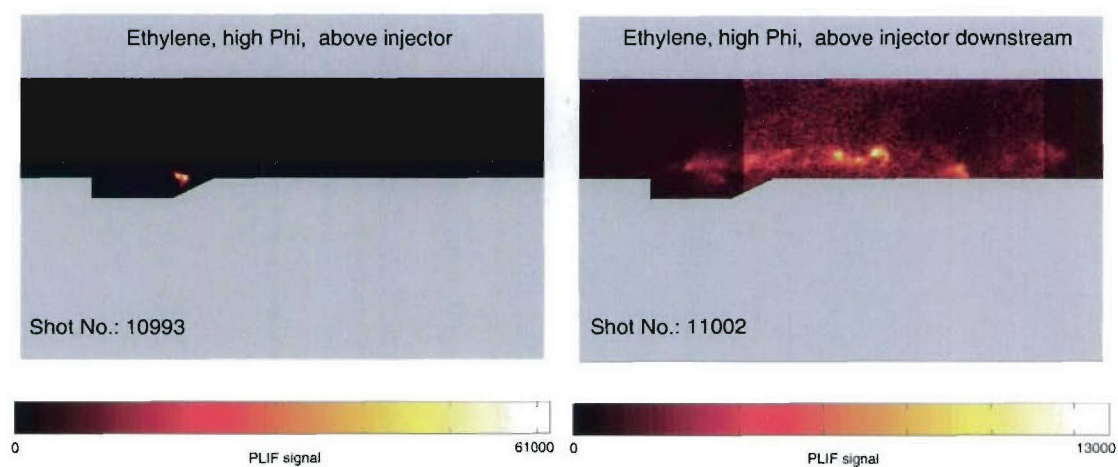


Figure A.5: Ethylene, high equivalence ratio ($\Phi = 0.64$)

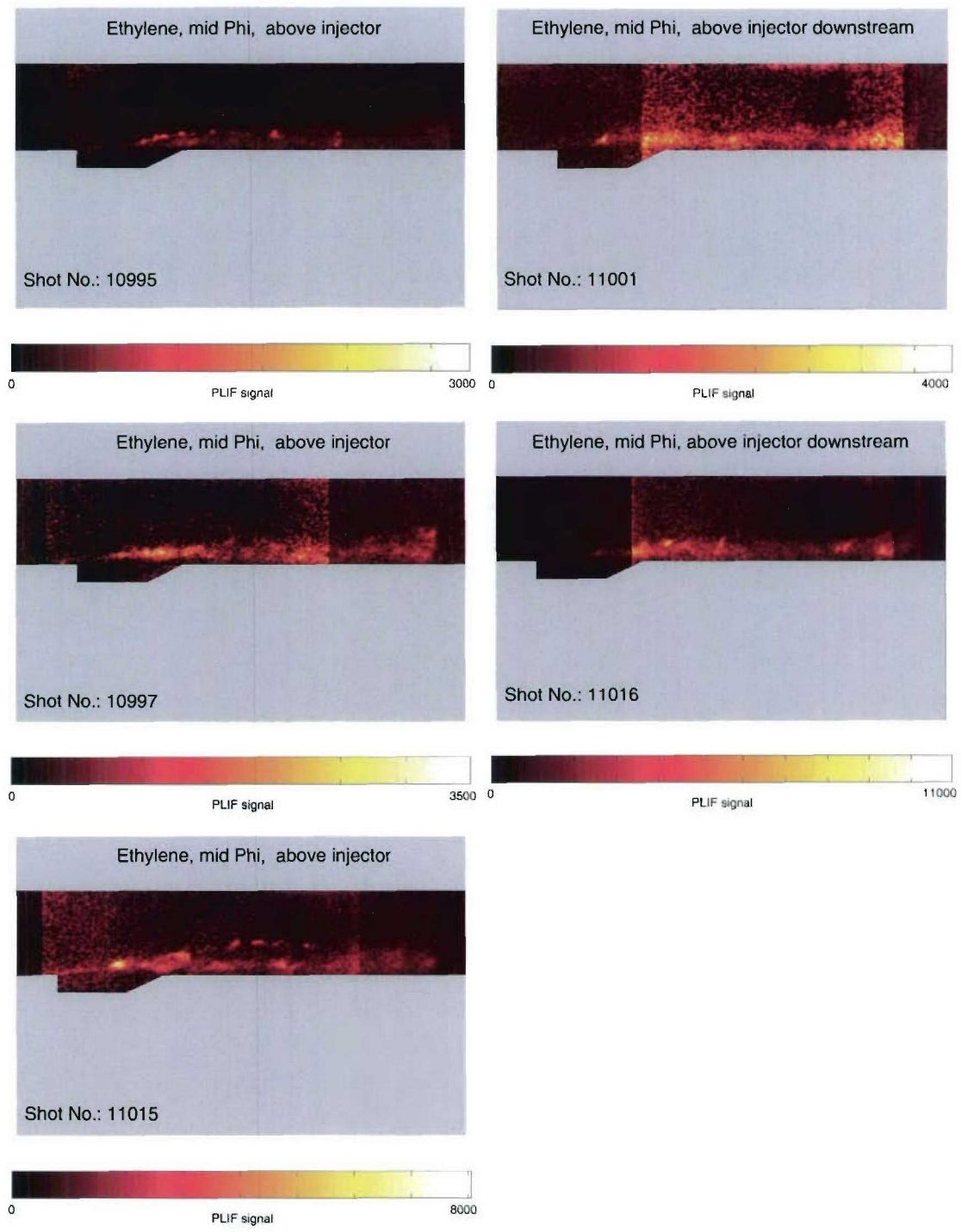


Figure A.6: Ethylene, medium equivalence ratio ($\Phi = 0.37$)

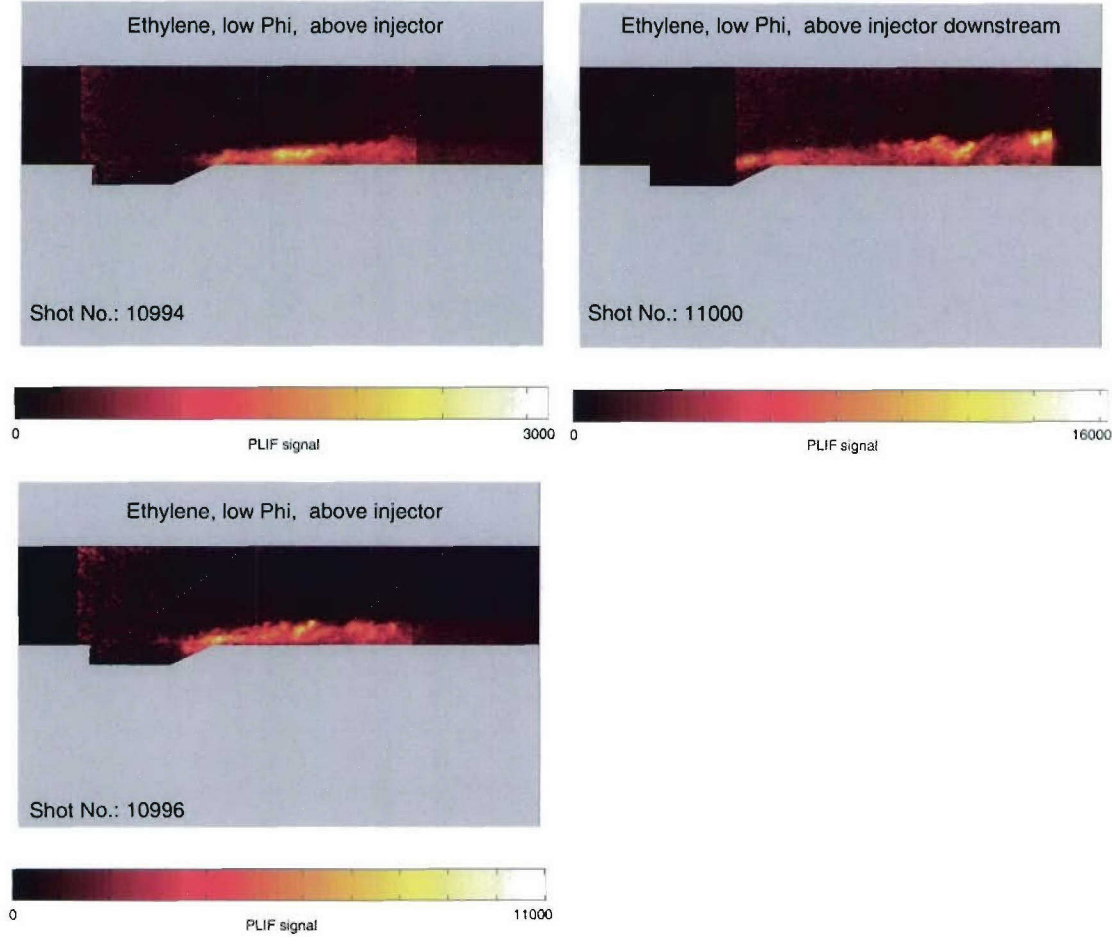


Figure A.7: Ethylene, low equivalence ratio ($\Phi = 0.13$)

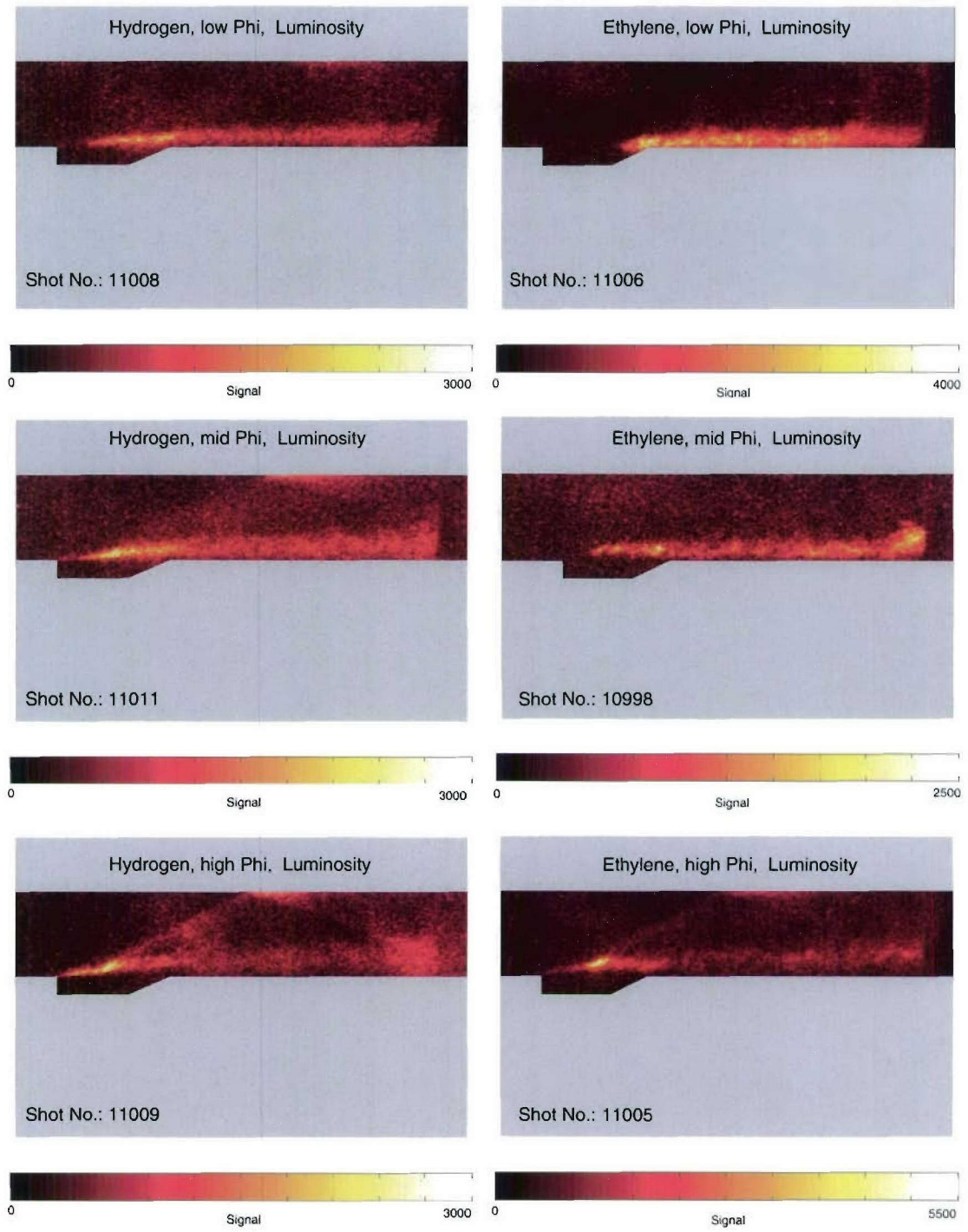


Figure A.8: Luminosity images for all fuel conditions investigated.

Bibliography

- Allen, M. G., Parker, T. E., Reinecke, W. G., Legner, H. H., Foutter, R. R., Rawlins, W. T. and Davis, S. J. (1993), 'Fluorescence imaging of OH and NO in a model supersonic combustor', *AIAA Journal* **31**(3), 505–512.
- Anderson, J. D. (1990), *Modern Compressible flow with Historical Perspective*, 2nd edn, M^CGraw-Hill.
- Anderson, J. D. (1995), *Computational Fluid Dynamics - The Basics with Applications*, 1st edn, M^CGraw-Hill.
- Baurle, R. A. (2004), Modeling of high speed reacting flows: Established practices and future challenges, in '42nd AIAA Aerospace Sciences Meeting and Exhibit', Reno, USA.
- Ben-Yakar, A. and Hanson, R. K. (2001), 'Cavity flame-holders for ignition and flame stabilization in scramjets: An overview', *Journal of Propulsion and Power* **17**(4), 869–877.
- Ben-Yakar, A., Kamel, M., Morris, C. and Hanson, R. K. (1998), 'Hypersonic combustion and mixing studies using simultaneous OH-PLIF and schlieren imaging'.
- Berg, J. and Shackelford, W. L. (1979), 'Rotational redistribution effect on saturated laser-induced fluorescence', *Applied Optics* **18**(3), 1093–2094.
- Boyce, R. R., Frost, M. and Paull, A. (2002), 'Combustor and nozzle CFD calculations for the HyShot scramjet flight experiment', *AIAA Paper* 2002–5268 .
- Bray, K. N. C. (1969), Chemical and vibrational nonequilibrium in nozzle flows, in 'Gasdynamics: A Series of Monographs', Marcel Dekker, Inc, New York.
- Cattolica, R. J. and Stephenson, D. A. (1984), Two-dimensional imaging of flame temperature using laser-induced fluorescence, in J. R. Brown, N. Manson, A. Oppenheim and R. Soloukhin, eds, 'Dynamics of Flames and Reactive Systems', Vol. 95, AIAA, New York, pp. 714–721.
- Colket, M. B. and Spadaccini, L. J. (2001), 'Scramjet fuels autoignition study', *Journal of Propulsion and Power* **17**(2), 315–323.

- Demtröder, W. (1996), *Laser Spectroscopy*, 2nd edn, Springer-Verlag.
- Drummond, J. P., Rogers, R. C. and Hussaini, M. Y. (1987), 'A numerical model for supersonic reacting mixing layers', *Computer Methods in Applied Mechanics and Engineering* **64**, 36–90.
- Eckbreth, A. C. (1996), *Laser Diagnostics for Combustion, Temperature and Species*, 2nd edn, Gordon and Breach.
- Evans, J. S. and Schexnayder, C. J. (1979), 'Influence of chemical kinetics and unmixedness on burning in supersonic hydrogen flows', *AIAA Journal* **18**, 188–193.
- Fox, J. S. (2003), Visualisation and Instantaneous Planar Laser-Induced Fluorescence Imaging Techniques Developed and Applied to Turbulent Flows, PhD thesis, Australian National University.
- Fraval, E., Danehy, P. M. and Houwing, A. F. P. (2001), Single-shot broadband coherent anti-Stokes Raman scattering measurements in a free piston shock tunnel nozzle expansion, in '23rd International Symposium on Shock Waves', Fort Worth, Texas, USA, July 22–27, 2001 (ed. F. K. Lu), pp. 396–402.
- Gai, S. L. (1992), 'Free piston shock tunnels: Developments and capabilities', *Progress in the Aerospace Sciences* **29**, 1–41.
- Gaston, M. J. (2002), A Study of Hypermixing Scramjet Fuel Injectors, PhD thesis, University of New South Wales.
- Gaydon, A. G. and Hurler, I. R. (1963), *The Shock Tube in High-Temperature Chemical Physics*, 1st edn, Chapman and Hall.
- Goldberg, U., Perroomian, O. and Chakravarthy, S. (1988), Application of the $k-\epsilon$ turbulence model to wall-bounded compressive flows, in '36th AIAA Aerospace Sciences Meeting and Exhibit', Reno, NV, USA.
- Goldberg, U., Perroomian, O., Chakravarthy, S. and Sekar, B. (1997), 'Validation of CFD++[®] code capability for supersonic combustor flowfields', *AIAA Paper No. 97-3271*. 33rd AIAA/ASME/SAE/ASEE Joint Propulsion Conference and Exhibit, Seattle, WA.
- Griffiths, A. (2004), Development and Demonstration of a Diode Laser Based Temperature and Water Vapour Sensor for Supersonic, Combusting Flows, PhD thesis, Australian National University.
- Gruber, M. R., Bauerle, R. A., Mathur, T. and Hsu, K. Y. (2001), 'Fundamental studies of cavity-based flameholder concepts for supersonic combustors', *Journal of Propulsion and Power* **17**(1), 146–153.

- Gruber, M. R., Dunbar, J. M., Carter, C. D. and Hsu, K. Y. (2004), 'Mixing and combustion studies using cavity-based flameholders in a supersonic flow', *Journal of Propulsion and Power* **20**(5), 769–778.
- Heiser, W. H. and Pratt, D. T. (1994), *Hypersonic Airbreathing Propulsion*, 1st edn, AIAA.
- Hubschmid, W. and Bombach, R. (2002), Laser spectroscopy in combustion research, Technical report, Paul Scherrer Institut, Switzerland.
- Hurle, I. R. (1971), Nonequilibrium flows with special reference to the nozzle-flow problem, in 'Proc. 8th International Shock Tube Symposium', London, England.
- Kanda, T., Sunami, T., Tomioka, S., Tani, K. and Mitani, T. (2001), 'Mach 8 testing of a scramjet engine model', *Journal of Propulsion and Power* **17**(1), 132–138.
- Luque, J. and Crosley, D. (1999), Lifbase: Database and spectral simulation program (version 1.5), Technical report, SRI International Report MP 99-009.
- Mathur, T., Gruber, M., Jackson, K., Donbar, J., Donaldson, W., Jackson, T. and Billig, F. (2001), 'Supersonic combustion experiments with a cavity-based fuel-injector', *Journal of Propulsion and Power* **17**(6), 1305–1312.
- M^CBride, B. J., Heibel, S., Ehlers, J. G. and Gordon, S. (1963), Thermodynamic properties to 6000 K for 210 substances involving the first 18 elements, Technical report, NASA SP-3001.
- M^CIntosh, M. K. (1968), Computer program for the numerical calculation of frozen equilibrium conditions in shock tunnels, Technical report, Australian National University.
- M^CIntyre, T. J., Houwing, A. F. P., Palma, P. C., Rabbath, P. A. B. and Fox, J. S. (1997), 'Optical and pressure measurements in shock tunnel testing of a model scramjet combustor', *Journal of Propulsion and Power* **13**(3), 388–394.
- Millikan, R. C. and White, D. R. (1963), 'Systematics of vibrational relaxation', *Journal of Chemical Physics* **39**(12), 3209–3213.
- Morgan, R. G. and Stalker, R. J. (1983), 'Fast acting hydrogen valve', *Journal of Physics E Scientific Instruments* **16**, 205–207.
- Neely, A. J., Riley, C., Boyce, R. R., Mudford, N. R., Houwing, A. F. P. and Gruber, M. R. (2003), 'Hydrocarbon and hydrogen-fuelled scramjet cavity flameholder performance at high flight Mach numbers', *AIAA Paper 2003-6989*. Proceedings of the 12th AIAA International Space Planes and Hypersonic Systems and Technologies Conference, Norfolk, Virginia, USA, December 15–19, 2003.
- O'Byrne, S. (1997), Examination of transient mixing and combustion processes in a supersonic combustion ramjet engine., Master's thesis, Australian National University.

- O'Byrne, S., Danehy, P. M. and Houwing, A. F. P. (2002), Nonintrusive temperature and velocity measurements in a hypersonic nozzle flow, *in* 'The Proceedings of the 22nd AIAA Aerodynamic Measurement Technology and Ground Testing Conference, St Louis, MI, USA'. AIAA Paper 2002-2917.
- Odam, J. (2004), Scramjet Experiments using Radical Farming, PhD thesis, University of Queensland.
- Palma, P. C. (1998), Laser-Induced Fluorescence Imaging in Free-Piston Shock Tunnels, PhD thesis, Australian National University.
- Paull, A. (1996), 'A simple shock tunnel driver gas detector', *Shock Waves* **6**(5), 309–312.
- Paull, A. (2003), Personal communication.
- Paull, A. and Stalker, R. J. (2000), Scramjet testing in the t3 and t4 hypersonic impulse facilities, *in* E. T. Curran and S. N. B. Murthy, eds, 'Progress in Astronautics and Aeronautics', Vol. 189, AIAA, pp. 1–46.
- Ratner, A., Driscoll, J. F., Huh, H. and Bryant, R. A. (2001), 'Combustion efficiencies of supersonic flames', *Journal of Propulsion and Power* **17**(2), 301–307.
- Samimy, M., Petrie, H. L. and Addy, A. L. (1986), 'Study of turbulent reattaching shear layers', *AIAA Journal* **24**(2), 261–267.
- Seiner, J. M., Dash, S. M. and Kenzakowski, D. C. (2001), 'Historical survey of enhanced mixing in scramjet engines', *Journal of Propulsion and Power* **17**(6), 1273–1286.
- Seitzman, J. M. and Hanson, R. K. (1993a), 'Comparison of excitation techniques for quantitative fluorescence imaging of reacting flows', *AIAA Journal* **31**(3), 513–519.
- Seitzman, J. M. and Hanson, R. K. (1993b), Planar fluorescence imaging in gases, *in* 'Instrumentation for Flows with Combustion', Academic Press Ltd.
- Stalker, R. J. (1967), 'A study of the free-piston shock tunnel', *AIAA Journal* **5**(12), 2160–2165.
- Stalker, R. J. (1972), 'Development of a hypervelocity wind tunnel', *The Aeronautical Journal* **76**, 374–384.
- Sudani, N., Valiferdowski, B. and Hornung, H. G. (2000), 'Test time increase by delaying driver gas contamination for reflected shock tunnels', *AIAA Journal* **38**(9), 1497–1503.
- Taha, A. A., Tiwari, S. N. and Mohieldin, T. O. (2002), 'Combustion characteristics of ethylene in scramjet engines', *Journal of Propulsion and Power* **18**(3), 716–718.
- Tishkoff, J. M., Drummond, J. P., Edwards, T. and Nejad, A. S. (1997), 'Future direction of supersonic combustion research: Air force/nasa workshop on supersonic combustion', *AIAA Paper 97-1017*.

- Tomioka, S., Murakami, A., Kudo, K. and Mitani, T. (2001), 'Combustion tests of a staged supersonic combustor with a strut', *Journal of Propulsion and Power* **17**(2), 293–300.
- Townend, L. H. (2001), 'Domain of the scramjet', *Journal of Propulsion and Power* **17**(6), 1205–1213.
- Turns, S. R. (1996), *An Introduction to Combustion*, 1st edn, McGraw-Hill.
- Vardavas, I. (1984), 'Modelling reactive gas flows within shock tunnels', *Australian Journal of Physics* **37**, 157–177.
- Yu, K. H., Wilson, K. and Schadow, K. (2001), 'Effect of flame-holding cavities on supersonic-combustion performance', *Journal of Propulsion and Power* **17**(6), 1287–1295.
- Zhang, X., Rona, A. and Edwards, J. (1998), 'The effect of trailing edge geometry on cavity flow oscillation driven by a shear layer', *The Aeronautical Journal* pp. 129–136.